

AD-A173 822

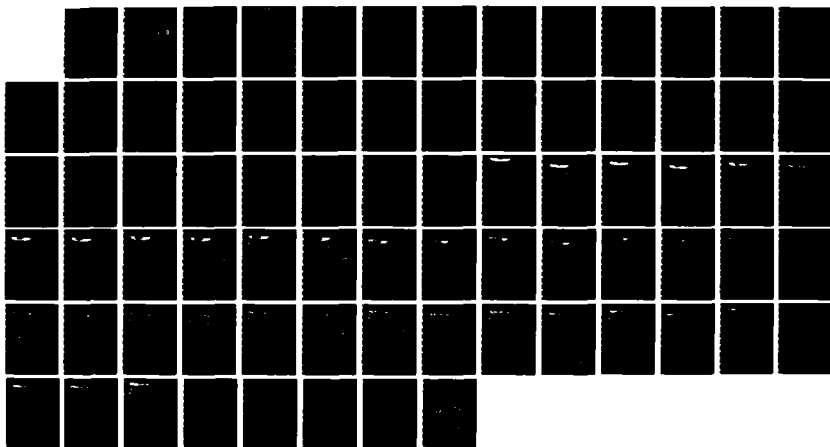
MHD SIMULATION OF THE INTERPLANETARY ENVIRONMENT IN THE
ECLIPTIC PLANE DU. (U) AIR FORCE GEOPHYSICS LAB HANSCOM
AFB MA M DRYER ET AL SEP 86 AFGL-TR-86-0189

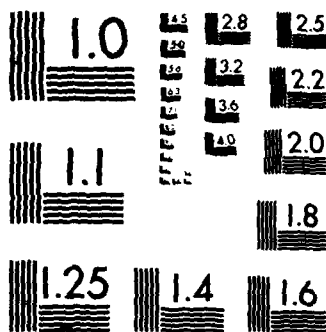
1/1

UNCLASSIFIED

F/G 3/2

NL





MICROCOPY RESOLUTION TEST CHART
NATIONAL BUREAU OF STANDARDS-1963-A

AFGL-TR-86-0189

MHD Simulation of the Interplanetary Environment
in the Ecliptic Plane During the 3-9 February 1986
Solar and Geomagnetic Activity

M. Dryer
Z.K. Smith
T.R. Detman
T. Yeh

DTIC
SELECTE
NOV 03 1986
S D

Space Environment Laboratory
NOAA/ERL
325 Broadway
Boulder, CO 80303

September 1986

Scientific Report No. 1

APPROVED FOR PUBLIC RELEASE; DISTRIBUTION UNLIMITED

AIR FORCE GEOPHYSICS LABORATORY
AIR FORCE SYSTEMS COMMAND
UNITED STATES AIR FORCE
HANSCOM AIR FORCE BASE, MASSACHUSETTS 01731

AD-A173 822

DTIC FILE COPY

"This technical report has been reviewed and is approved for publication"

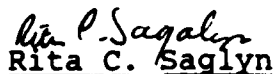


Don F. Smart
Contract Manager



E. G. Mullen
Chief, Space Particles Environment Branch

FOR THE COMMANDER


Rita C. Saglly

Director, Space Physics Division

This report has been reviewed by the ESD Public Affairs Office (PA) and is releasable to the National Technical Information Service (NTIS).

Qualified requestors may obtain additional copies from the Defense Technical Information Center. All others should apply to the National Technical Information Service.

If your address has changed, or if you wish to be removed from the mailing list, or if the addressee is no longer employed by your organization, please notify AFGL/DAA, Hanscom AFB, MA 01731. This will assist us in maintaining a current mailing list.

AD-1173 811

REPORT DOCUMENTATION PAGE

1a. REPORT SECURITY CLASSIFICATION UNCLASSIFIED			1b. RESTRICTIVE MARKINGS		
2a. SECURITY CLASSIFICATION AUTHORITY			3. DISTRIBUTION/AVAILABILITY OF REPORT		
2b. DECLASSIFICATION/DOWNGRADING SCHEDULE			Available for public release Distribution unlimited		
4. PERFORMING ORGANIZATION REPORT NUMBER(S)			5. MONITORING ORGANIZATION REPORT NUMBER(S)		
			AFGL-TR-86-0189		
6a. NAME OF PERFORMING ORGANIZATION Space Environment Laboratory NOAA/ERL		6b. OFFICE SYMBOL (If applicable)	7a. NAME OF MONITORING ORGANIZATION Air Force Geophysics Laboratory		
6c. ADDRESS (City, State and ZIP Code) 325 Broadway Boulder Colorado 80303		7b. ADDRESS (City, State and ZIP Code) Hanscom Air Force Base Bedford, MA 01731			
8a. NAME OF FUNDING/SPONSORING ORGANIZATION		8b. OFFICE SYMBOL (If applicable) PHP	9. PROCUREMENT INSTRUMENT IDENTIFICATION NUMBER Project order ESD-6-625		
8c. ADDRESS (City, State and ZIP Code)		10. SOURCE OF FUNDING NOS			
		PROGRAM ELEMENT NO. 61102F	PROJECT NO. 2311	TASK NO. G4	WORK UNIT NO. AA
11. TITLE (Include Security Classification) (U) MHD Simulation of The Interplanetary Environment (Con't)					
12. PERSONAL AUTHOR(S) M. Dryer, Z. K. Smith, T. R. Detman and T. Yeh					
13a. TYPE OF REPORT Scientific Report No. 1		13b. TIME COVERED FROM Nov 85 TO Sep 86		14. DATE OF REPORT (Yr., Mo., Day) 86 September	
				15. PAGE COUNT 74	
16. SUPPLEMENTARY NOTATION					
17. COSATI CODES			18. SUBJECT TERMS (Continue on reverse if necessary and identify by block number)		
FIELD	GROUP	SUB GR			
03	01		MHD modeling, Solar flare generated Shock		
03	02		Solar-Terrestrial Physics, February 1986 Events		
			Interplanetary medium, Geomagnetic storm		
19. ABSTRACT (Continue on reverse if necessary and identify by block number) A numerical simulation, based on physical principles, is performed for the interplanetary medium's response to six solar flares that were observed, sequentially, in real time by NOAA and AWS instruments on 3-7 February 1986. This epoch is of great practical interest because of the extensive geomagnetic disturbances and associated near-Earth activity that followed these flares on 6-9 February 1986. The magnetohydrodynamic simulation is carried out with the Space Environment Laboratory's 2-1/2D IGM (Interplanetary Global Model) code. It demonstrates the multiple, compound interactions of the interplanetary disturbances produced by these flares by using input perturbations based upon real-time optical, radio, and satellite observations. The optical (H-alpha) and radio (microwave to metric wavelength) data were obtained from the SOON/RSTN sites, and full-disk-					
20. DISTRIBUTION AVAILABILITY OF ABSTRACT UNCLASSIFIED/UNLIMITED <input checked="" type="checkbox"/> SAME AS RPT <input type="checkbox"/> DTIC USERS <input type="checkbox"/>			21. ABSTRACT SECURITY CLASSIFICATION Unclassified		
22a. NAME OF RESPONSIBLE INDIVIDUAL Don F. Smart			22b. TELEPHONE NUMBER (Include Area Code) 617-377-3978		22c. OFFICE SYMBOL PHP

Cont of Block 11:

in the Ecliptic Plane During the 3-9 February 1986 Solar and Geomagnetic Activity

Cont of Block 19 (ABSTRACT)

integrated X-ray measurements were obtained from the NOAA/GOES-5 and -6 satellites. Examination of the simulated solar wind output (such as momentum flux, and cross-magnetospheric tail electric field) at Earth's position indicates that the major geomagnetic activity was probably due primarily to the second and fifth solar flares in the sixfold sequence. "Predicted" geomagnetic storm sudden commencement (SSC) times were early by only about 4 percent (3-4 hours) for the pulses suggested by the consequences of the second and sixth flares.

The 180 hour simulation, which required only 100 seconds (CPU time) on the NOAA/NBS CYBER 855/205, required 8 hours clock time on the Space Environment Laboratory's APOLLO workstation. Thus, it has potential for realtime operational use by a facility that may not have access to, or funding for, a supercomputer such as the 205.

1. INTRODUCTION

Carrington Rotation 1771 of the sun was characterized by a sequence of twelve solar flares, commencing 3 February and ending 15 February 1986, from NOAA/SEL/SESC Regions 4711 and 4713. The optical classification ranged from SF to 3B and the X-ray classification ranged from M1 to X3. Substantial geomagnetic activity followed the first six flares in this sequence. In the preceding several solar rotations, geomagnetic activity was minor during the first phase of each rotation. There was somewhat more significant geomagnetic activity during the latter phase of each rotation (presumably, because of recurrent coronal hole activity). The outstanding geomagnetic (etc.) activity during the earlier half of Rotation 1771 could, for the most part, be ascribed to the first set of six flares (or subset thereof). Although one small recurrent coronal hole made its appearance at the east limb in the beginning of February, the simulation discussed here will not take it into account. Our present intention is to focus on the six flares only.

The geomagnetic storm of 6-9 February 1986 qualifies as one of the most intense on record (Allen, 1986). The effects on an extensive set of multifarious systems are listed in Table I. The probable causes of these events have been ascribed (G. R. Heckman, private communication, 1986) in approximate percentages: (1) events caused by geomagnetic storm effects, 75%; (2) events caused by energetic particles, 15%; and (3) events caused directly by the X-rays and microwave emission of the solar flares, 10%.



<input checked="" type="checkbox"/>	
<input type="checkbox"/>	
<input type="checkbox"/>	
Codes	
Date	Approved/ or special
A-1	

Our primary purpose is to study the multiple interactions of the flare-generated disturbances without considering latitudinal gradients of the disturbed parameters. Our procedure, applied to the ecliptic plane, seems reasonable for this point of the solar cycle (near-minimum) because the solar flares took place near that plane within the range 2°S - 10°S latitude. For the purpose of the present study, the flares will be assumed to have taken place in the ecliptic plane which is the plane of analysis for the 2-1/2D dimensional (D) Interplanetary Global Model (IGM) code (Wu et al., 1983; Dryer and Wu, 1982; Gislason et al., 1984; Dryer et al., 1984; Dryer and Smart, 1984; Dryer, 1985; Dryer et al., 1986b; Dryer and Smith, 1986; and Smith et al., 1986). The 2-1/2D refers to the fluid analysis that considers all dependent variables, including the three components of the velocity and interplanetary magnetic field (IMF) vectors, within the two-dimensional ecliptic plane. We hope to study the present epoch at a later date with our fully time-dependent 3D IGM code (Han et al., 1986; Dryer et al., 1986a) in order to examine the latitudinal and heliospheric current sheet effects.

Our secondary purpose is to study the geoeffectiveness implied by using the time series of the disturbed solar wind plasma parameters to display the variations of momentum flux and cross-tail electric field. We will show that certain flare-generated disturbances (specifically those caused by the second and fifth flares) are most likely to have caused the major momentum flux and electric field changes at Earth, implying, therefore, the most significant geomagnetic and ionospheric disturbances. Stated somewhat differently, the location of the flare relative to Earth is not, necessarily, the determining

factor in the geomagnetic response. The intervening interplanetary configuration preceding a given flare's propagating disturbance is an important factor in the question of geoeffectiveness.

Any physical model must meet the following criteria before it could be accepted for operational use:

- (1) The underlying assumptions should be a reasonable representation of the physical phenomena for which a simulation is attempted.
- (2) The approach should pass proof-of-principle test by examination for many cases.
- (3) Input data should be available and accurate.
- (4) Output information should be useful.

In the discussion below we outline the assumptions adopted for the IGM code within the present context. We note several reasons for the choice of the present example for testing of the proof-of-principle. We have constrained our input data to quantities that can be inferred or calculated from what we consider to be significant real-time observations. We suggest below that the momentum flux variability of the solar wind at Earth's orbit and the magnetospheric cross-tail electric field are examples of important "geoeffective" parameters of interest to an operational model's utility.

In Section 2, we discuss the solar activity and some of the near-Earth system responses during the 3-9 February 1986 epoch. In particular we discuss the use of the observed data from the input assumptions of the IGM. The assumed initial state of the solar wind is also outlined. The results of the simulations are given in Section 3, followed by some concluding remarks in Section 4.

2. INTERPLANETARY GLOBAL MODEL

Solar Activity. Two active regions made their appearance during Carrington Rotation 1771 as shown on the H-alpha inferred neutral line chart in Figure 1 (P. S. McIntosh, private communication, 1986). Region SESC 4711, with central meridian (CM) passage on 5 February 1986, and Region SESC 4713, with CM passage on 8 February 1986, produced six flares (five of which were in Region 4711) of interest to our study. A small He I 10830 \AA -inferred coronal hole was detected just north and to the east of the latter active region as shown in Figure 1. The possible effect of one or more high speed streams (cf., Kojima and Kakinuma, 1986) will not be considered in our study at this time so that the potential compound effects of the flares themselves could be assessed. We plan to include simulations of likely high speed streams at a later time.

During the same phases of the four previous solar rotations, there had been no significant solar flares or erupting prominences, as evidenced by arrivals of energetic particles and/or geomagnetic activity. Thus, the "isolated" character of this sequence of six flares, as listed in Table II, taken together with the important systems effects referred to in Table I,

suggests itself as a useful candidate for one of many tests of the physical modeling approach suggested in our earlier work.

The events listed in Table II were detected in real time by the NOAA/AWS system: GOES (full-disk-integrated X-ray flux) satellites (Garcia, 1986), SOON (H-alpha filtergrams and optical flare classification), and RSTN (radio bursts). Estimates of the shock velocity derivable from the Type II bursts were not made at the RSTN sites and, hence, were inferred [even in the absence of Type II's in the case of Event (i.e., flare) Numbers 3, 4, and 6] for the purpose of the simulations. These estimates were inferred on a subjective basis and, hence, cannot be justified on a rigorous basis. Support for this approach is provided by the statistical study (when Type II bursts were detected) of the monotonic relationship of peak X-ray flux and interplanetary shock velocity reported by Pinter and Dryer (1985).

Input Pulse Assumptions for MHD Simulation. We assumed that each event (flare) produced a coronal shock wave as noted above. The initial shock velocity, relative to an assumed uniform background solar wind, is given in Table III for each event. These values are then used to compute the MHD Rankine-Hugoniot jump conditions at the radial position of $18 R_s$ ($R_s = 1$ solar radius = 6.97×10^5 km) along each flare's meridian. This position was chosen because it is a representative point beyond all steady-state critical points in the solar wind. The steady-state solution is discussed below. We assume that the shock leaves the flare's vicinity and moves to the inner boundary ($18 R_s$) of the computational domain (half of the ecliptic plane) at this velocity. The clock time given in Table III starts ($t = 0$ hr) when the first shock,

which we assume to have left the sun at approximately the time of X-ray maximum of the first flare, arrives at $18 R_{\odot}$. The same assumption is made for each of the succeeding events as listed in Table III. These shocks, then, should be considered to be piston driven to, and slightly beyond (as explained below), this position of $18 R_{\odot}$. An extensive study of piston driven shocks, and their subsequent attenuation into blast waves, has been given by Smart and Shea (1985). The basic ideas (constant velocity propagation followed by a power law deceleration) included within that empirical study are also contained within the more detailed simulation in the present paper.

We also assumed a sinusoidal spatial profile of the shock strength over an 18° included angle centered at the meridian of each flare. This value was chosen rather arbitrarily in order to provide a representative non-spherical extension of the disturbance that emanated from the flare site. Temporally, a trapezoidal rise and fall for each parameter at each heliolongitudinal position was assumed for periods of time listed in Table III. This duration was chosen to be the additional piston driving time as suggested by inspection of the temporal profiles of X-ray flux measured by the GOES satellites. This inspection was straight forward in the determination of the moment of initial rise above background flux but arbitrary in the choice of the time of return to near-background. A subjective duration, rounded off in units of one-half-hour, was chosen as a result of this inspection. This characterization of each flare's contribution of energy, momentum, and mass to the surrounding corona and solar wind is a crude approximation of what are basically poorly understood phenomena in solar flare physics. Our goal is to describe large-scale features in space and time. Hence, we believe that these input

assumptions can be considered reasonable representations of the actual physical phenomena. We found in a very limited test of sensitivity, for example, that the shock created by Flare 2 arrived at Earth about 5 hours earlier than the case studied here when the hypothesized piston duration was increased (Table III) from 1/2 hour to 1 hour and all other parameters were unchanged. Yet the global structure, to be described below, of IMF and plasma was not changed in any appreciable way. Nevertheless, it is appropriate to note that any success in describing large-scale features does not relieve the modeler of any burden of making the best possible assumptions for input.

Initial Steady State of the Interplanetary Medium. We assumed that the initial state of the interplanetary medium (prior to $t = 0$) was homogeneous; i.e., independent of heliolongitude. Moreover, we assumed that the IMF contained an initial southward component. In the 2-1/2D computational code, the partial differential equations for the governing physical laws for conservation of mass, momentum, and energy and Maxwell's equations (Wu et al., 1983) are written with three independent variables (t, r, ϕ) and eight dependent variables ($V_r, V_\theta, V_\phi, B_r, B_\theta, B_\phi, n, T$). The partial derivatives with respect to helio-colatitude θ at the equatorial plane are assumed to be zero. [This restriction has been removed in the full 3D code described by Han et al., 1986].

The initial steady state is established by first assuming a representative data set and then allowing the numerical solution of the time-dependent equations to relax into a steady state solution within an acceptable tolerance level. The sun-centered spherical coordinate system is used with

heliocentric radius r increasing outward, the helio-colatitude θ increasing downward from 0° at the northern axis, and the heliolongitude ϕ increasing from 0° at the east limb as viewed from Earth. The range of spatial variables in the simulation is from $18 R_\odot \leq r \leq 232 R_\odot$ (1.1 AU), $\theta = 90^\circ$, and $0^\circ \leq \phi \leq 180^\circ$.

Table IV includes the initial solar wind plasma and IMF values at both the inner boundary, (viz., $18 R_\odot$), and just within the outer boundary (viz., 1 AU) of the computational domain. The derived parameters: plasma beta β , total pressure P , and momentum flux nmv^2 are also listed in the table. The IMF should be recognized as having a positive (viz., "away") polarity by virtue of the positive radial and negative azimuthal components as described in a sun-centered spherical coordinate system. We may consider that the magnetic flux that leaves the sun in this half-plane returns to it in the other half-plane of the ecliptic.

3. RESULTS

Global View of the Half-Ecliptic Plane: Figure 2 presents, graphically, the initial ($t = 0$ hr) steady-state parameters (V_r , n , T , P , and the unit vector of the IMF as projected into the ecliptic plane) as summarized in Table IV. At the upper left corner, the radial velocity is plotted upward in the three-dimensional graphical presentation of the uniform solar wind in the half-ecliptic plane as "viewed" by an observer, at $r > 1$ AU, who "looks" toward the sun. The velocity V_r is equal to 255 km/sec at the inner boundary of $18 R_\odot$, which is not seen in this perspective. The east and west limb meridians are,

respectively, to the left and right of the reader's perspective. The vertical "cliff" at 1.1 AU is, of course, a graphics artifact but can be used from one figure to another to assess the scale change that was required by the graphics software on occasion. In Figure 2, the higher value of $V_r = 355$ km/sec at 1.0 AU can easily be inferred near the foreground of the symmetrically uniform solar wind at $t = 0$ hr. The plot at the lower right corner of Figure 2 shows the Archimedean spiral of the IMF as viewed from the northern solar pole; this IMF direction is, of course, indicated by the unit vectors as projected into the ecliptic plane. The remaining three plots display the proton density, temperature, and total pressure in a logarithmic scale (base 10). In succeeding figures, (for $0 < t \leq 180.1$ hr), the upper right corner (blank in Figure 2) is used to display the solar wind vector change, ΔV_r , relative to the initial steady state undisturbed value at each location. The maximum velocity change is listed on each of these figures. Each figure (with its six panels) displays the properties in ~5 hour increments. Each spatial tick mark refers to 0.1 AU per division. Time "zero" ($t = 0$ hr), as described earlier, is started when the shock from the first flare reaches $18 R_g$; this time corresponds (approximately) to 2300 UT on 3 February 1986 when converted to real time. Hence, the reader can approximate the simulation's clock time at $t = 0$ hr to correspond, roughly, to the start of 4 February 1986. Earth is located along the vertical axis; the sun is at the origin as viewed from above the ecliptic plane.

Discussion of Time-Dependent Simulation: The results of the simulated interplanetary environment during this epoch of solar and geomagnetic activity are best seen from the perspective of a hypothetical observer who looks down

at the half-ecliptic plane from, say, the northern pole of the sun. A number of interactions will be seen as the evolving disturbances move outwardly from the solar neighborhood to that of Earth. Formation of forward and reverse interplanetary shocks will be identified without ambiguity. Shock strength attenuation of some flare disturbances will be pointed out when one forward shock propagates into a region that has been accelerated by a preceeding shock from an earlier flare. We will also observe the effects of a longer-lasting, piston driven, forward shock as it overtakes and interacts with the reverse shock from a previous flare. Some of these effects involve the global distortion of the overtaking shocks. It will be shown that only three flares from the sequence of six were "geoeffective". Following this sequence of dispersion, interaction, and distortion of the staccato solar events in this epoch, the hypothetical observer will note a gradual return to the original, steady-state parameters discussed earlier.

Figures 3-38 display the simulated response of the interplanetary medium at intervals of approximately 5 hours, from $t = 5.2$ hr to $t = 180.1$ hr. Identification comments are occasionally made on the figures. Thus, "Flare 1", as indicated on the top left panel of Figure 3, refers to the interplanetary disturbance caused by the first flare as discussed earlier. No special designation is assigned to the products for interacting shocks (forward with forward, forward with reverse, etc. as discussed in greater detail by Smith et al., 1986); instead we chose to continue with the designation of the stronger interplanetary shock. Thus, for example, the interplanetary disturbance labeled as Flare 2 in Figures 5-7 is observed to overtake Flare 1. The latter is then no longer referred to. Instead, we

observe the development of the fast reverse MHD shock that follows the fast forward MHD shock from Flare 2 in Figures 8-10.

Inspection of the density contours in Figures 8-10 also reveals the more inconsequential effects of Flare 3 that, nevertheless, must blend in with the effects of Flare 2. The forward and reverse shocks of the latter are also labeled in these and subsequent figures. The reverse shocks are most easily identified by the steepening of the temperature contours closest to the flare's meridian. An alternative approach, though harder to identify because of the graphical scale, is the velocity vector plot (upper right corner of Figures 8-10) which shows that the faster solar wind, produced initially by the stronger Flare 2, is caused to slow down in the frame of an observer riding on the reverse shock. Figures 8 and 9, for example, show the location of Flare 2's reverse shock and the reduction in length of the velocity increment vectors as one moves outwardly in helioradius.

Flare 4 is observed at $t = 45.1$ hr in Figure 11 near Earth's central meridian. Flare 3 can still be identified in the contour plots (seen, for example, in the density curves) but cannot be seen from the perspective of the viewer in the upper left, three-dimensional velocity plot because of the foreshadowing effects of Flare 2. Distortion of the IMF is clearly seen in the unit vector presentation of each of these figures. Eventually, Flare 3 can be observed in the velocity plot (Figure 13) as the effects of Flare 2 are attenuated.

We have also attempted to identify the reverse shock associated with

Flare 2 in Figure 13 by reference to the requirement of a shift of polarity (and increasing magnitude) to the east. This polarity shift is also seen near the central axis of the forward shock in the lower right panel of Figure 13.

Flare 5, the result of the longer-lasting piston driven shock (simulating the main features of the flare on 6 February 1986, 0625 UT), is clearly seen in Figure 14 at $t = 60$ hr. This disturbance rapidly overtakes and overwhelms Flare 4 as suggested in Figures 15 and 16. We also observe, in Figures 17-20, the overtaking of Flare 2's reverse shock by Flare 5's forward shock. The early stages of Flare 6 are also detected at $t = 90$ hr in Figure 20 just as its piston driven phase ends and its blast phase begins.

The development of the reverse shock from Flare 5 and the distortion of its forward shock are seen in Figures 20 and 21. The distortion is undoubtedly indicated by its interaction with the reverse shock of Flare 2 as noted above.

Flare 6, as seen in Figures 22-27, has a similar scenario, namely the overtaking of the reverse shock of the earlier Flare 5 by the forward shock of Flare 6. Collision takes place, again in a spatially oblique configuration, in Figure 27 ($t = 125.2$ hr), just beyond Earth's position.

In the remaining figures of this sequence (Figures 27-38), we observe the dispersion and attenuation of Flare 6. There is a gradual return to the original, steady-state parameters and Archimedean spiral form of the IMF.

Time Series of Plasma and IMF at 1 AU. Our interest for potential operational interpretations and eventual comparison with observations is clearly directed to the output at various points in the ecliptic plane. Observations, when available, from IMP-8 at Earth and the "Halley Armada" (VEGA 1/2, GIOTTO, SAKIGAKE, SUISEI, and ICE) will obviously be of great interest in this respect. At this time, we direct attention to six hypothetical observation points at 1 AU.

Figure 39 shows the time series of V_r , n , and T at these six positions. The left column of the figure shows these simulated parameters at three solar longitudes: 27°E , 18°E , and 9°E of the Earth's meridian. Recall that the Earth is located along the vertical axis in the previous Figures 2-38. The right column of panels in Figure 39 refers to three additional solar longitudes: 0°W (i.e., Earth's location), 9°W , and 18°W of Earth's meridian.

Flare 2's forward shock produced jumps that were somewhat larger to the east of Earth. This was expected because Flare 2 occurred at 21°E of Earth's meridian. There was an effect indicated in the parameters ($\Delta V \approx 100$ km/sec) at $t \approx 85$ hr when the stronger portion of Flare 2's reverse shock arrived at the 27°E and 18°E positions. As anticipated (see the contours of n , T , and P in Figures 18, 19, and 20), there was no perceptible change at the 9°E position until Flare 5's forward shock arrived at $t = 85 - 90$ hr. Arrival of Flare 5's reverse shock at the three eastern positions is observed best in the velocity plot, followed shortly by Flare 6's forward shock.

The major disturbances at Earth are indicated (Figure 39, right side,

solid curve) to be due to the disturbances associated with the forward shocks from Flare 2, Flare 5, and Flare 6. The other two positions at 9°W and 18°W experience a delay in response from Flare 2 and Flare 5 but have an earlier response, compared with that at Earth, from Flare 6.

The time series for the magnitude $|B|$ of the IMF is shown in Figure 40 (top panels) for the same six positions. The azimuthal component B_{ϕ} is shown in the middle panels, and the meridional component B_{θ} is plotted (with the appropriate sign change) in the lower panels (labeled as B_z). The latter, B_z , is customarily used in the solar-ecliptic coordinate system (with the X-axis pointed to the sun, the Y-axis pointed to the east of the observing position, and the Z-axis forming the remainder of a right-handed system). This usage is conventionally used by magnetospheric physicists. It is seen that the pre-existing southward field is compressed by Flare 2 to nearly -20γ followed by a large-scale rotation moving toward, but never achieving, a northward polarity. The rotation involves a large-amplitude Alfvén wave which is then hit by Flare 5 and the sequence is repeated, albeit at smaller magnitude, after collision with Flare 6.

The time series for momentum flux is shown in Figure 41. Flare 5 clearly is indicated to be the major pulse at Earth (upper panel, solid line). Indeed, preliminary information (C. Rufenach, private communication, 1986) indicates, from GOES 5/6 magnetometer data, that a series of four magnetopause crossings took place at the geosynchronous ($6.6 R_E$) altitude during the period starting with Flare 5's forward shock until that disturbance's decay. The last two magnetopause crossings (including the one with the longest duration

between crossings) occurred when, according to the simulation, the momentum flux was decreasing and, indeed, was even less than that for the original undisturbed solar wind. This observation, then, serves to caution the modeler to reconsider the input (such as the possible high speed stream from the coronal hole[s] mentioned earlier). We also point out that the present simulation does not have the spatial resolution to reveal physical phenomena on scales smaller than $\sim 10^5$ km because of the grid size used ($\Delta r = 2R_s$, $\Delta\theta = 3^\circ$, $\Delta\phi = 3^\circ$). Turbulent fluctuations, then, cannot be simulated in the present model. It is of interest to note that the storm sudden commencements implied by the arrival at Earth of the forward shocks associated with Flare 2 and Flare 6 at $t \approx 60$ hr and ≈ 135 hr (the latter, during the interaction with Flare 5's reverse shock) correspond fairly well with the actual SSC's observed on 6 February (1313 UT) and 9 February (1748 UT) 1986. The clock time for the actual SSC's would require the simulation to have been at $t = 62.2$ hr and 138.8 hr, thereby indicating the "predictions" to have been early by about 4 percent.

No actual SSC was detected during the pulse designated here as Flare 5 even though the magnetopause responded as noted above. We speculate that the strong magnetic activity that started on 6 February 1986 and continued until 9 February 1986 may have obscured a clear SSC signal during this interval. In fact, the Fredericksburg, Virginia, 3-hr K indices for the most disturbed 24 hours of 8-9 February 1986 were 6, 7, 8, 8, 9, 9, 8, 7 as reported by Allen (1986) thereby indicating validity to our speculation.

Finally, another "geoeffectiveness" parameter that can be derived from

the results of the simulation is the cross-magnetospheric-tail electric field VB_z as shown in Figure 42. The relative magnitudes are again shown at each of the six "sampling points" at 1 AU. VB_z exhibits a fourfold increase at the Earth (top panel, solid line) from 2 mV m^{-1} to about 8 mV m^{-1} for the first two pulses (from Flares 2 and 5) and from 0.5 mV m^{-1} to 2.5 mV m^{-1} for the third pulse (Flare 6). Parenthetically, we note that, had Earth been located at the 27°E position (lower panel, Figure 42, solid line) the simulation suggests a sixfold increase in VB_z from 2 mV m^{-1} to 12.5 mV m^{-1} as a result of the first pulse. Following this latter scenario, the momentum flux (Figure 41, lower panel, solid line) would have increased tenfold from 5×10^{-9} to $55 \times 10^{-9} \text{ dyn cm}^{-2}$.

We remind the reader that the simulation has used an inertial coordinate system. Earth has implicitly been assumed to remain at the 1 AU position along the vertical axis shown in the Figures 2-38. Actually, of course, Earth moves around the sun at a rate of 1 degree per day. During the period of the simulation, 4-11 February 1986, a 7 degree movement to the west would have taken place. We have centered our input pulses at the meridian of each flare as viewed from Earth (see Table II). We believe that the uncertainty involved in our assumptions of spatial and temporal values for the consequences of each flare is more important than the error suggested in Earth's actual location during this epoch. Nevertheless, some compensation for this movement may be approximated by interpolation between the additional, hypothetical, "sampling point" at 9°W and the "Earth's position" at 0°W of CM.

4. CONCLUDING REMARKS

An MHD, time-dependent, 2-1/2D computer model for the interplanetary dynamics was used to simulate the disturbances in the interplanetary medium caused by a series of six flare-induced coronal shocks. This effort was inspired by the availability of real-time observations during the epoch of 3-11 February 1986. We do not claim to represent the real, complex, poorly understood physical phenomena at and near the flare site by anything more than a crude approximation based on limited observations and their comparison with theory and earlier modeling efforts. Comparison with actual observations at Earth was limited in this study to the times of SSC's. These comparisons between observations and simulations are encouraging. The simulated SSC's arrived at the Earth 3-4 hours before the actual ones for the second and sixth flares. Additional comparisons must await the availability of spacecraft data at various points in space.

Further simulations should be made to test the sensitivity of the output to changes in the many parameters that must be considered. One such test has been mentioned: an increase in the pulse duration from 1/2 hr to 1 hr for Flare 2 resulted in a shock arrival at Earth about 5 hours earlier than that shown in the present paper. Other sensitivity tests, such as the omission of one or more "flare" pulses, should be conducted.

In addition we plan to incorporate the simulation of one or two coronal hole streams in addition to the present use of six "flare" pulses.

The February 1986 epoch has been an ideal period for a study of this kind because it took place at solar minimum in the absence of any other significant solar activity. We suggest that much more insight and understanding may be gained by such a study despite our imperfect knowledge from limited observations and interpretations. We do believe, however, that a study of a more complex solar atmosphere that produces an equally complex heliospheric structure cannot be ignored. Heliospheric current sheets and three-dimensional effects must be considered in the future so that we can widen our ability to simulate flare events at higher latitudes, eruptive prominences, shearing of photospheric and coronal magnetic topologies, and irregularly shaped high-speed coronal hole streams. These forms of solar activity should be simulated in various ways, taken both singly and in combination.

In conclusion, we have demonstrated the usefulness of the NOAA/SEL 2-1/2D Interplanetary Global Model (IGM) to study compound events of important geophysical interest. Of particular interest is the demonstration of complex interactions among disturbances from multiple, staccato flares. The study suggests that the researcher and forecaster can make more meaningful assessments of cause and effect in more complicated cases.

The computer code required only 100 seconds (CPU time) on the CYBER 855/205 computer for a 180-hour simulation of one-half of the ecliptic plane covering a radius of 1.1 AU. The same run could be made in 8 hours on the SEL APOLLO workstation; thus, real-time use in an operational forecasting mode is possible for a facility that may have neither funding nor access to a supercomputer such as the CYBER 205. More importantly, simulations of the

type discussed here require further testing via comparisons with multi-spacecraft data sets before operational application is undertaken.

ACKNOWLEDGMENTS

This work has been supported in part by Air Force Geophysics Laboratory Order No. ESD-6-625. We are grateful for discussions, comments, and suggestions from J. H. Allen, P. Bornmann, H. Garcia, S. M. Han, G. R. Heckman, H. Leinbach, P. S. McIntosh, L. Murdock, C. Rufenach, M. A. Shea, D. F. Smart, T. Speiser, M. D. Szymanowski and S. T. Wu. We also thank T. Jacobwith for his efficient and rapid preparation of the manuscript.

REFERENCES

- Allen, J. H., Major magnetic storm effects noted, EOS, 67, 537, 1986.
- Dryer, M., Interplanetary evolution of solar flare-generated disturbances and their potential for producing magnetospheric activity, in Proceedings of Kunming Workshop on Solar Physics and Interplanetary Travelling Phenomena (C. de Jager and B. Chen, Eds.), Science Press, Beijing, China, pp. 943-954, 1985.
- Dryer, M., and D. F. Smart, Dynamical models of coronal transients and interplanetary disturbances, Adv. Space Res., 4(7), 291-301, 1984.
- Dryer, M., and Z. K. Smith, MHD simulation of multiple interplanetary disturbances during STIP Interval VII (August, 1979), in Proceedings of the Solar Maximum Analyses Symposium (V. E. Stepanov and V. N. Obridko, Eds.), VNU Science Press, Utrecht, in press, 1986.
- Dryer, M., S. T. Wu, and S. M. Han, Three-dimensional, time-dependent, MHD model of a solar flare-generated interplanetary shock wave, in The Sun and the Heliosphere in Three Dimensions (R. G. Marsden, Ed.), D. Reidel Publ. Co., Dordrecht, pp. 135-140, 1986a.

Dryer, M., Z. K. Smith, S. T. Wu, S. M. Han, and T. Yeh, MHD simulation of the "Geoeffectiveness" of interplanetary disturbances, in Solar Wind-Magnetosphere Coupling (Y. Kamide and J. A. Slavin, Eds.), Terra Scientific Publ. Co., Tokyo, in press, 1986b.

Dryer, M., and S. T. Wu, Magnetohydrodynamic modelling of interplanetary disturbances between the sun and earth, Air Force Geophysics Laboratory Report AFGL-TR-82-0396, 21 December, 1982. ADA130115

Dryer, M., and D. F. Smart, Dynamical models of coronal transients and interplanetary disturbances, Adv. Space Res., 4(7), 291-301, 1984.

Dryer, M., S. T. Wu, G. Gislason, S. M. Han, Z. K. Smith, J. F. Wang, D. F. Smart, and M. A. Shea, Magnetohydrodynamic modelling of interplanetary disturbances between the sun and earth, Astrophys. Space Sci., 105, 187-208, 1984.

Garcia, H. A., Solar flares and the intense geomagnetic storm of Feb. 1986 (abstract), Bull. Amer. Astronom. Soc., 18(2), 699-700, 1986.

Gislason, G., M. Dryer, Z. K. Smith, S. T. Wu, and S. M. Han, Interplanetary disturbances produced by a simulated solar flare and equatorially-fluctuating heliospheric current sheet, Astrophys. Space Sci., 98, 149-161, 1984.

Han, S. M., S. T. Wu, and M. Dryer, A transient, three-dimensional MHD model for numerical simulation of interplanetary disturbances, in STIP Symposium on Retrospective Intervals (M. A. Shea and D. F. Smart, Eds.), Book Crafters Publ. Co., Chelsea, Michigan, in press, 1986.

Kojima, M., and T. Kakinuma, Three-station observations of interplanetary scintillation at 327 MHz - II. Evolution of two-dimensional solar wind structure during 1983 to 1985, Proc. Res. Inst. Atmos. (Nagoya University), 33, 1, 1986.

Pinter, S., and M. Dryer, The influence of the energy emitted by solar flare X-ray bursts on the propagation of their associated interplanetary shock waves, Astrophys. Space Sci., 116, 51-60, 1985.

Smart, D. F., and M. A. Shea, A simplified model for timing the arrival of solar flare-initiated shocks, J. Geophys. Res., 90, 183-190, 1985.

Smith, Z. K., M. Dryer, and S. M. Han, Interplanetary shock collisions: forward with reverse shocks, Astrophys. Space Sci., 119, 337-344, 1986.

Wu, S. T., M. Dryer, and S. M. Han, Non-planar MHD model for solar flare-generated disturbances in the heliospheric equatorial plane, Solar Phys., 84, 395-418, 1983.

TABLE I. Geomagnetic Storm of February 3-9, 1986:
Effects on Systems At/Near Earth

Cheyenne Mountain Complex and NOAA/NGDC:

- . HF Communication link failures on February 4, 0740-0800 UT and on February 7-8, 2243-0205 UT.
- . Bit flips on ESA Geostationary Satellite on February 4, 1817 UT and 1915 UT and on February 8, 2045 UT.
- . Bit flips on Geostationary Communication Satellites on February 8-9, 1650-1435 UT.
- . X-ray sensor saturation on ESA Polar Satellite from February 5, 2043 UT to February 8, 2107 UT.
- . Power surges at two radar ground stations on February 7, 1325-1455 UT.
- . Heavy aurora at Flyingdale AFB on February 7, 1400 UT.
- . Radio frequency interference at radar site on February 7, 1400 UT to February 8, 0200 UT.
- . Power outages on Geosynchronous Telecommunication Satellite on February 8, 1121-1248 UT.

NOAA/SEL/SESC:

- . North Atlantic HF radio propagation was nil to poor.
- . Minnesota Power Company had 3% voltage drop.
- . Naval Astroynamics Satellites had seriously degraded communications. System was close to shut-down.
- . Voice of America had degraded HF reception and satellite alignment problems.
- . Omega System (U. S. Coast Guard) had errors due to anomalous phase advance.

* Lt. K. Lutz, Cheyenne Mt. Complex; J. Allen, NOAA/NGDC; G. R. Heckman and J. Hirman, NOAA/SEL/SESC (private communications, 1986).

Table II. Major Solar Flares During 3-7 February 1986

Event	Date (X-ray maximum)	Location (Active Region)	Classification (Optical / X-ray)	Radio Burst (Metric Sweep)
1	3 February (2049 UT)	S09 E26 (AR4711)	1B / M2.3	Type II Type IV
2	4 February (0741 UT)	S03 E21 (AR4711)	3B / X3.0	Type II
3	4 February (1029 UT)	S02 E68 (AR4713)	1B / M6.4	
4	5 February (1255 UT)	S07 E06 (AR4711)	2B / M3.0	
5	6 February (0625 UT)	S04 W06 (AR4711)	3B / X1.7	Type II
6	7 February (1034 UT)	S10 W20 (AR4711)	2B / M5.2	Type IV

Table III. Assumed Input Pulses for Events of February 1986

<u>Event</u>	<u>Shock Velocity</u>	<u>Duration</u>	<u>Clock Time</u>
#1	1500 km/sec	1 hr	0 hr
#2	2000 km/sec	1/2 hr	10.42 hr
#3	1000 km/sec	1 hr	15.00 hr
#4	1000 km/sec	1 hr	40.16 hr
#5	2000 km/sec	2 hr	57.16 hr
#6	1000 km/sec	3 hr	86.66 hr

Table IV

Initial Steady-State Solar Wind

Parameter	18 R_s	1 AU
V_r (km sec ⁻¹)	250.	355.
V_θ "	0.2	0.01
V_ϕ "	4.0	0.35
B_r (gamma)	300.	2.1
B_θ "	100.	6.0
B_ϕ "	- 30.	-2.0
n (cm ⁻³)	600.	3.0
T (°K)	1.06×10^6	3.1×10^4
$\beta(16\pi nkT/B^2)$	0.43	0.15
$P(2nkT + B^2/8\pi)$ (dyn cm ⁻²)	5.8×10^{-7}	2.0×10^{-10}
nmv^2 (dyn cm ⁻²)	6.3×10^{-7}	6.3×10^{-9}

FIGURE TITLES

1. Synoptic H-alpha chart of Carrington Rotation 1771 (14 January - 10 February 1986). Note the solar magnetic polarities, active regions, and the implied, essentially flat, heliospheric current sheet.
2. Properties of simulated interplanetary medium at $t = 0$ hr (2300 UT, 3 February, 1986).
3. Properties of simulated interplanetary medium at $t = 5.2$ hr (0412 UT, 4 February, 1986).
4. Properties of simulated interplanetary medium at $t = 10.1$ hr (0906 UT, 4 February, 1986).
5. Properties of simulated interplanetary medium at $t = 15.2$ hr (1412 UT, 4 February, 1986).
6. Properties of simulated interplanetary medium at $t = 20.1$ hr (1906 UT, 4 February, 1986).
7. Properties of simulated interplanetary medium at $t = 25.1$ hr (0006 UT, 5 February, 1986).
8. Properties of simulated interplanetary medium at $t = 30.1$ hr (0506 UT, 5 February, 1986).
9. Properties of simulated interplanetary medium at $t = 35.2$ hr (1012 UT, 5 February, 1986).
10. Properties of simulated interplanetary medium at $t = 40.3$ hr (1518 UT, 5 February, 1986).
11. Properties of simulated interplanetary medium at $t = 45.1$ hr (2006 UT, 5 February, 1986).
12. Properties of simulated interplanetary medium at $t = 50.0$ hr (0100 UT, 6 February, 1986).
13. Properties of simulated interplanetary medium at $t = 55.1$ hr (0606 UT, 6 February, 1986).
14. Properties of simulated interplanetary medium at $t = 60.0$ hr (1100 UT, 6 February, 1986).
15. Properties of simulated interplanetary medium at $t = 65.2$ hr (1612 UT, 6 February, 1986).
16. Properties of simulated interplanetary medium at $t = 70.2$ hr (2112 UT, 6 February, 1986).

17. Properties of simulated interplanetary medium at $t = 75.0$ hr (0200 UT, 7 February, 1986).
18. Properties of simulated interplanetary medium at $t = 80.1$ hr (0706 UT, 7 February, 1986).
19. Properties of simulated interplanetary medium at $t = 85.2$ hr (1212 UT, 7 February, 1986).
20. Properties of simulated interplanetary medium at $t = 90.0$ hr (1700 UT, 7 February, 1986).
21. Properties of simulated interplanetary medium at $t = 95.1$ hr (2206 UT, 7 February, 1986).
22. Properties of simulated interplanetary medium at $t = 100.2$ hr (0312 UT, 7 February, 1986).
23. Properties of simulated interplanetary medium at $t = 105.2$ hr (0812 UT, 7 February, 1986).
24. Properties of simulated interplanetary medium at $t = 110.1$ hr (1306 UT, 7 February, 1986).
25. Properties of simulated interplanetary medium at $t = 115.1$ hr (1806 UT, 7 February, 1986).
26. Properties of simulated interplanetary medium at $t = 120.1$ hr (2306 UT, 7 February, 1986).
27. Properties of simulated interplanetary medium at $t = 125.2$ hr (0412 UT, 8 February, 1986).
28. Properties of simulated interplanetary medium at $t = 130.0$ hr (0900 UT, 8 February, 1986).
29. Properties of simulated interplanetary medium at $t = 135.3$ hr (1418 UT, 8 February, 1986).
30. Properties of simulated interplanetary medium at $t = 140.1$ hr (1906 UT, 8 February, 1986).
31. Properties of simulated interplanetary medium at $t = 145.3$ hr (0018 UT, 9 February, 1986).
32. Properties of simulated interplanetary medium at $t = 150.3$ hr (0518 UT, 9 February, 1986).
33. Properties of simulated interplanetary medium at $t = 155.2$ hr (1012 UT, 9 February, 1986).

34. Properties of simulated interplanetary medium at $t = 160.1$ hr (1506 UT, 9 February, 1986).
35. Properties of simulated interplanetary medium at $t = 165.3$ hr (2018 UT, 9 February, 1986).
36. Properties of simulated interplanetary medium at $t = 170.3$ hr (0118 UT, 10 February, 1986).
37. Properties of simulated interplanetary medium at $t = 175.1$ hr (0606 UT, 10 February, 1986).
38. Properties of simulated interplanetary medium at $t = 180.1$ hr (1106 UT, 10 February, 1986).
39. Time series of simulated radial velocity V_r , density, n , and temperature, T , at six sampling points at 1 AU. Left column presents the simulations at 27°E (solid curve), 18°E (dashed curve), and 9°E (dotted curve) of Earth's central meridian. Right column presents the simulations at 0°W (Earth's position, solid curve), 9°W (dashed curve), and 18°W (dotted curve) of Earth's meridian.
40. Time series of simulated interplanetary magnetic field magnitude $|B|$, azimuthal magnetic field component B_ϕ , and the negative value of the meridional magnetic field component B_θ plotted here as B_z at six hypothetical sampling points at 1 AU. As in Figure 39, the panels on the left side refer to the three points east of Earth and, on the right side, to Earth's position and two additional points to the west of Earth.
41. Time series of simulated momentum flux (nmV^2) at six hypothetical sampling points at 1 AU. Upper panel refers to Earth's position (0°W of central meridian, solid curve), 9°W (dashed curve), and 18°W (dotted curve) of central meridian. Lower panel refers to 27°E (solid curve), 18°E (dashed curve), and 9°E (dotted curve) of Earth's meridian.
42. Time series of simulated cross-magnetospheric tail electric field (VB_z) variations at six hypothetical sampling points at 1 AU. Upper panel refers to Earth's position (0°W of central meridian, solid curve), 9°W (dashed curve), and 18°W (dotted curve) of Earth's meridian. Lower panel refers to 27°E (solid curve), 18°E (dashed curve), and 9°E (dotted curve) of Earth's meridian.

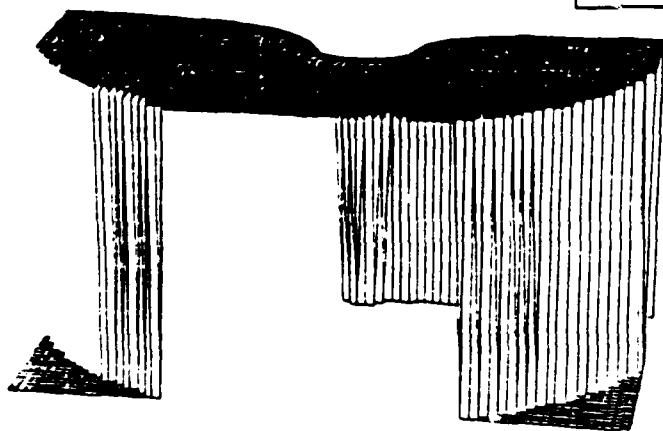
10 9 8 7 6 5 4 3 2 1 31 30 29 28 27 26 25 24 23 22 21 20 19 18 17 16 15 14
FEBRUARY, 1960 JANUARY, 1960

0 30 60 90 120 150 180 210 240 270 300 330 360

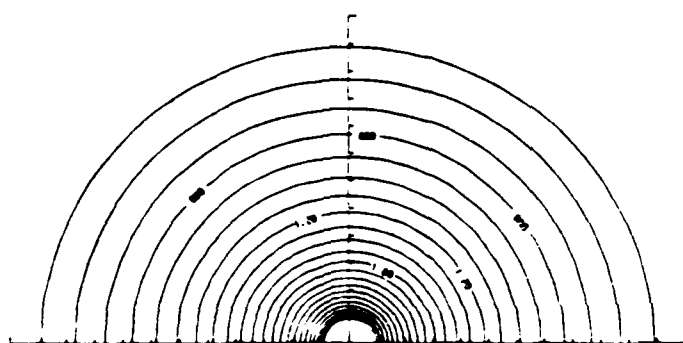
10830 Coronal Hole Estimate

- 30

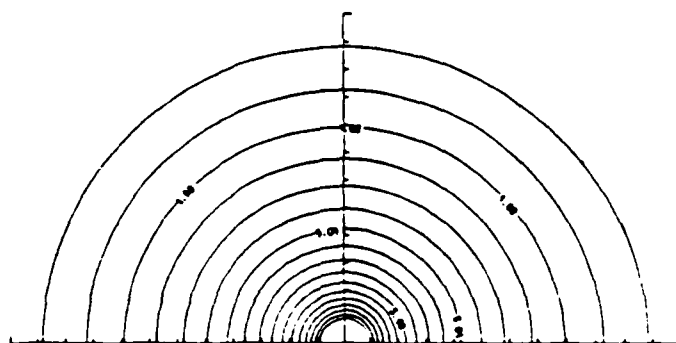
$t = 0.0$ hr



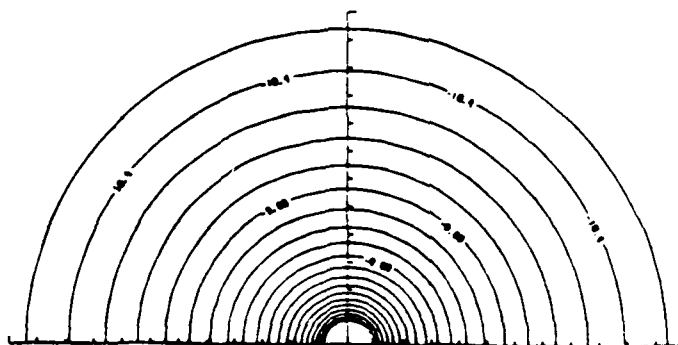
Solar Wind Speed



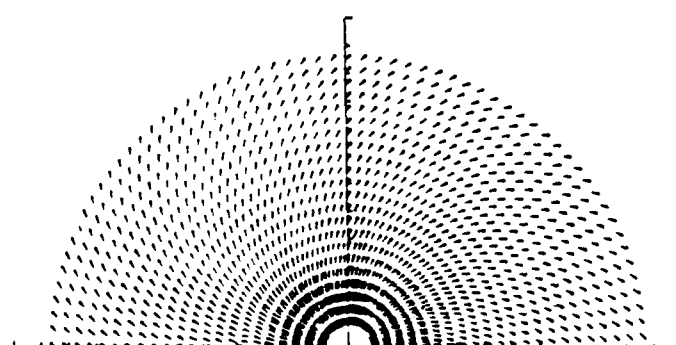
Proton Density



Temperature



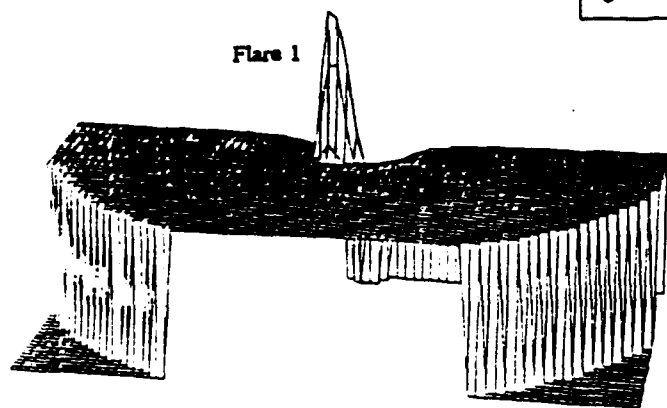
Total Pressure



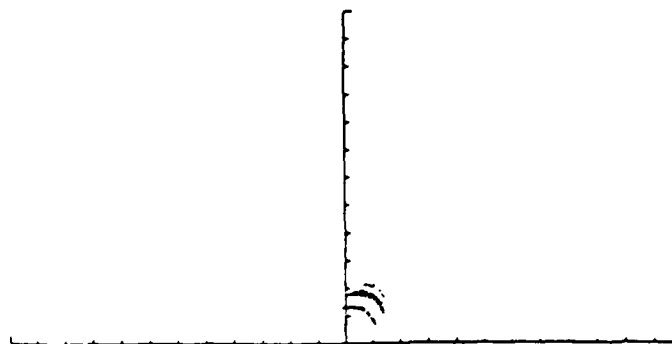
IMF Direction

2. Properties of simulated interplanetary medium at $t = 0$ hr (2300 UT, 3 February, 1986).

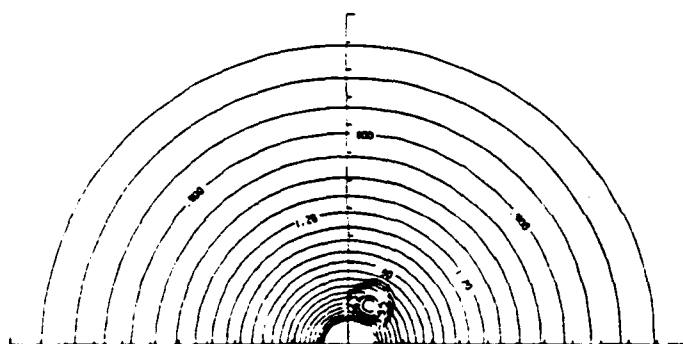
$t = 5.2 \text{ hr}$



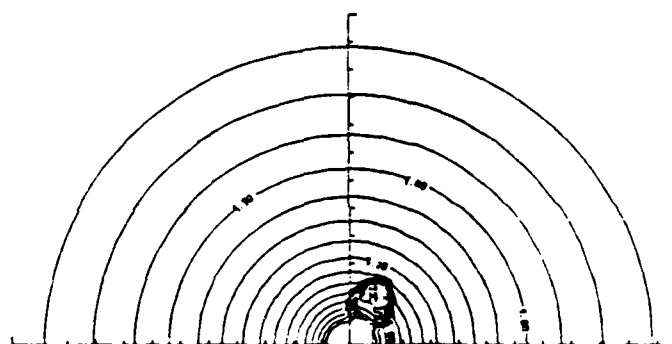
Solar Wind Speed



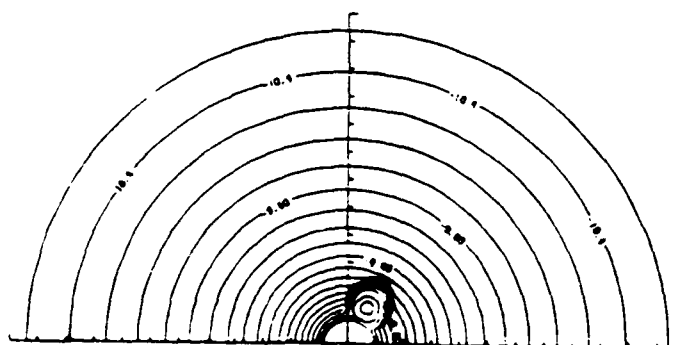
Velocity Increment
(maximum: 357 km/s)



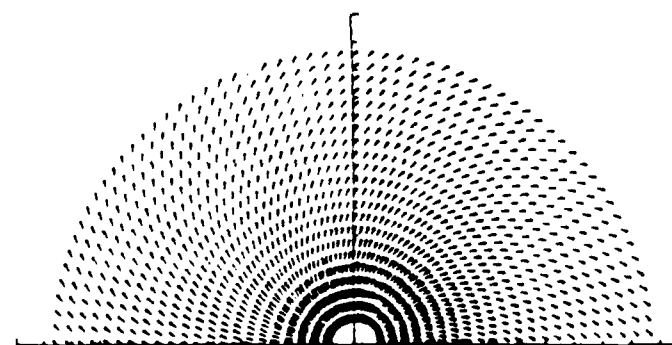
Proton Density



Temperature



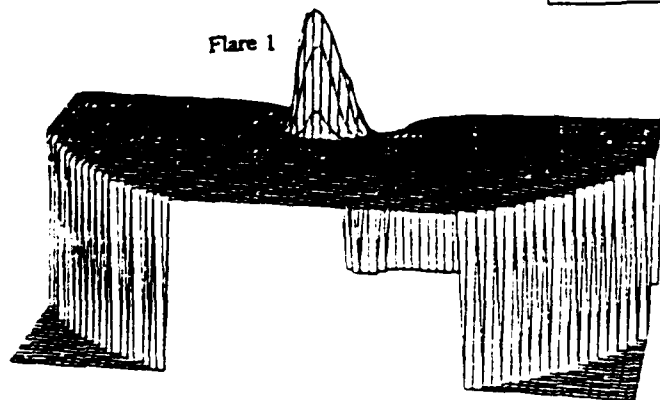
Total Pressure



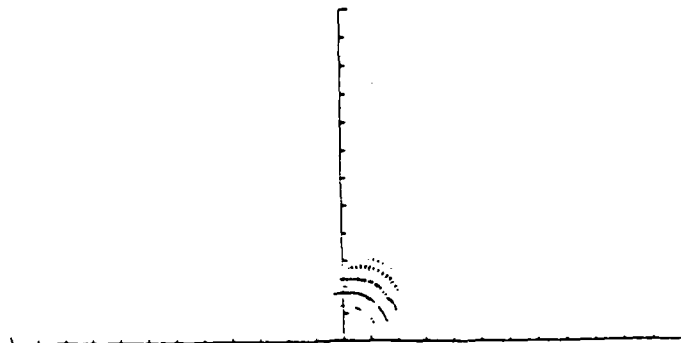
IMF Direction

3. Properties of simulated interplanetary medium at $t = 5.2 \text{ hr}$ (0412 UT, 4 February, 1986).

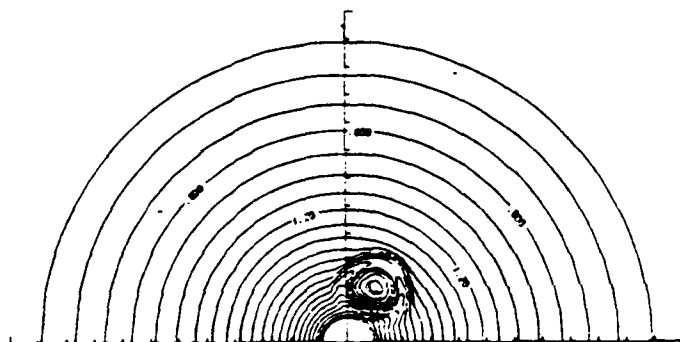
$t = 10.1$ hr



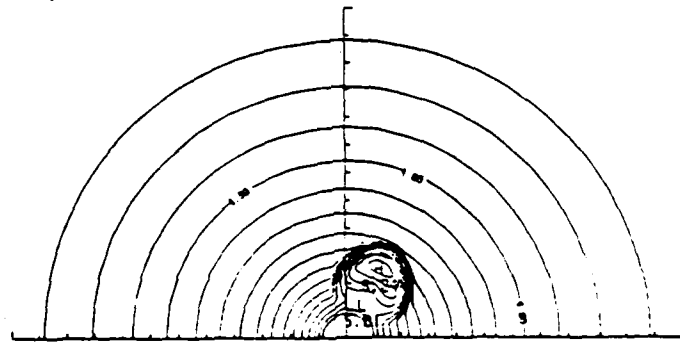
Solar Wind Speed



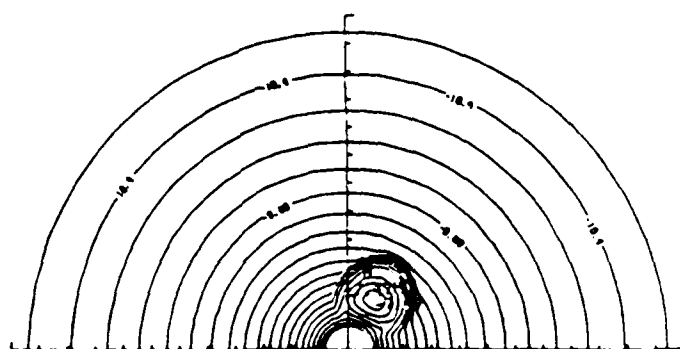
Velocity Increment
(maximum: 258 km/s)



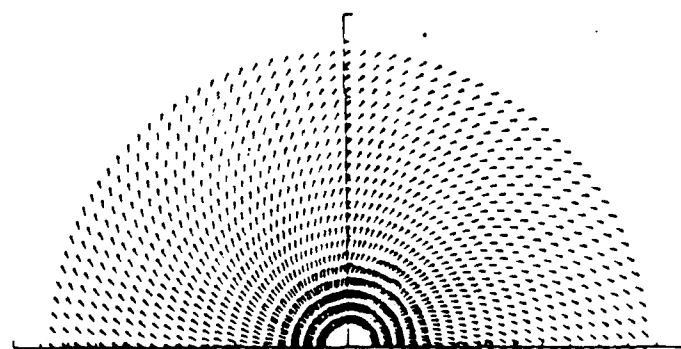
Proton Density



Temperature



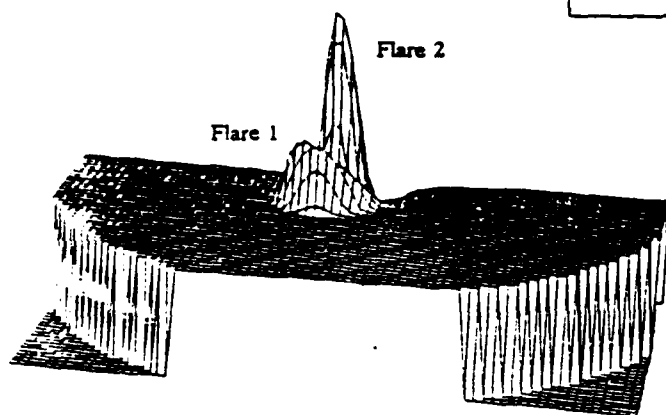
Total Pressure



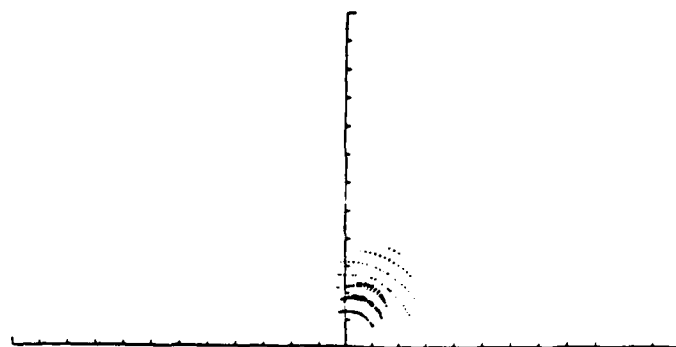
IMF Direction

4. Properties of simulated interplanetary medium at $t = 10.1$ hr (0906 UT, 4 February, 1986).

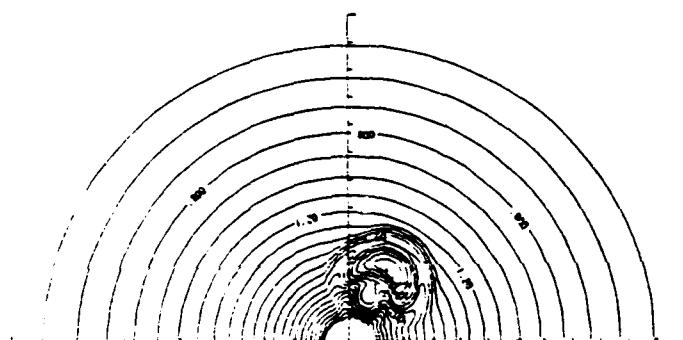
$t = 15.2 \text{ hr}$



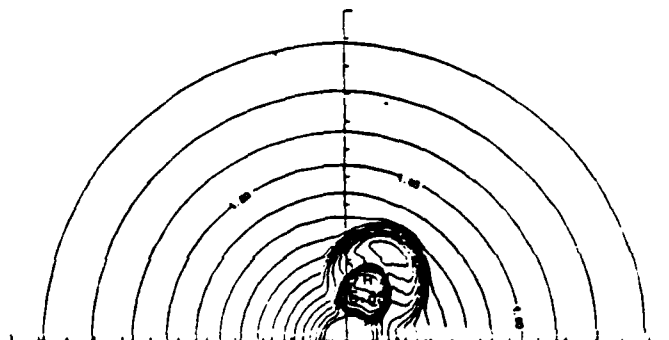
Solar Wind Speed



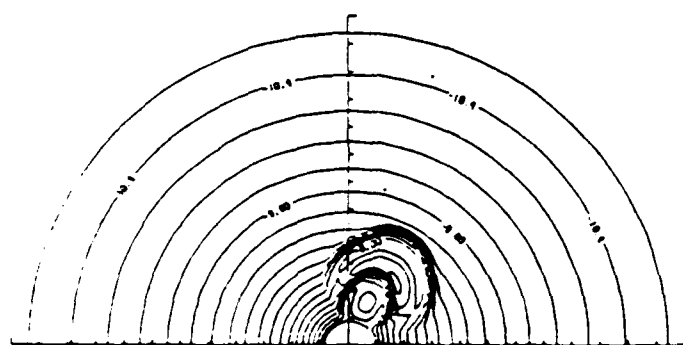
Velocity Increment
(maximum: 600 km/s)



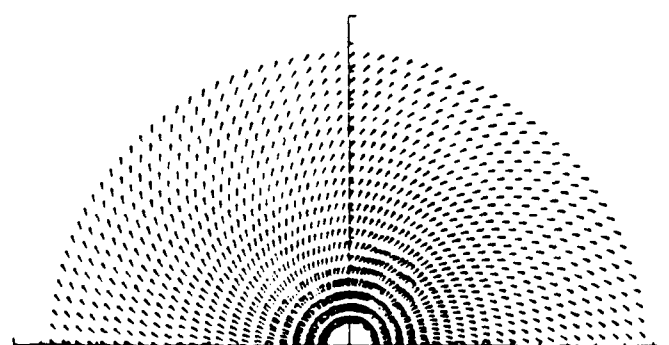
Proton Density



Temperature



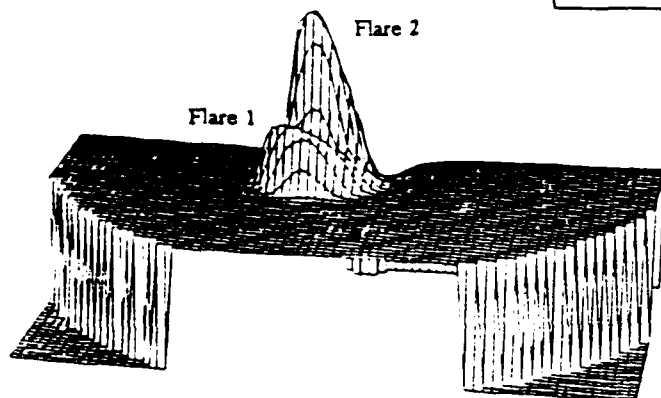
Total Pressure



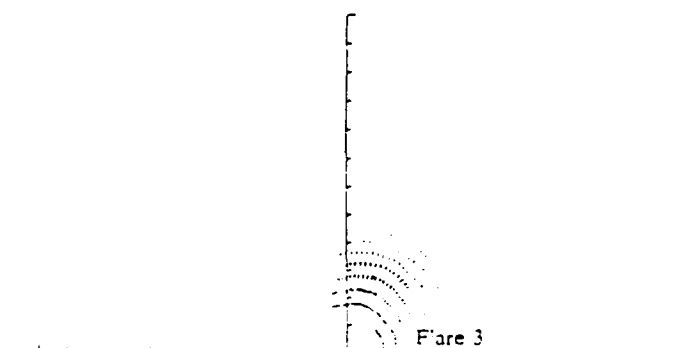
IMF Direction

5. Properties of simulated interplanetary medium at $t = 15.2 \text{ hr}$ (1412 UT, 4 February, 1986).

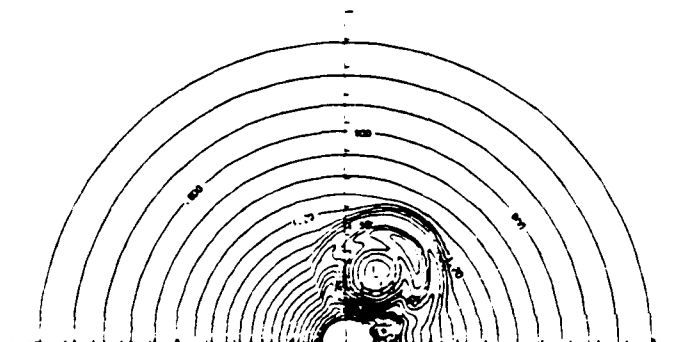
$t = 20.1 \text{ hr}$



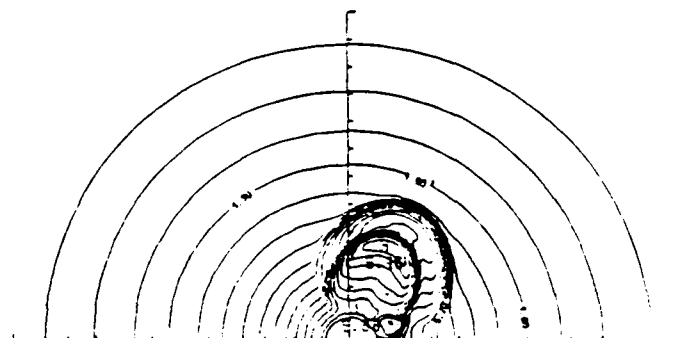
Solar Wind Speed



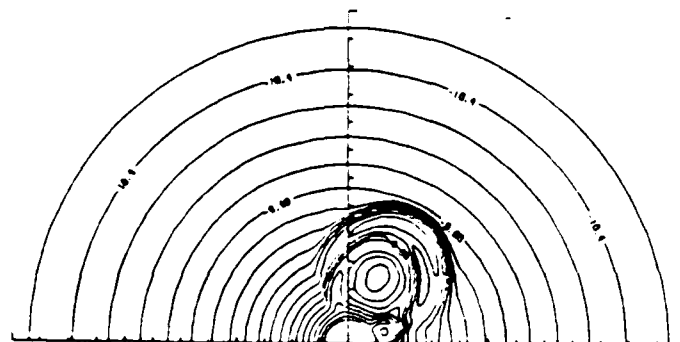
Velocity Increment
(maximum: 487 km/s)



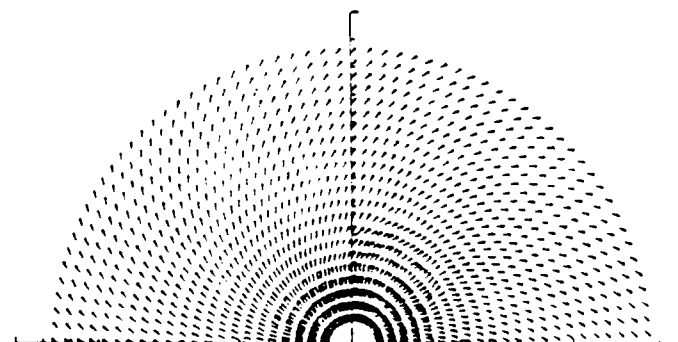
Proton Density



Temperature



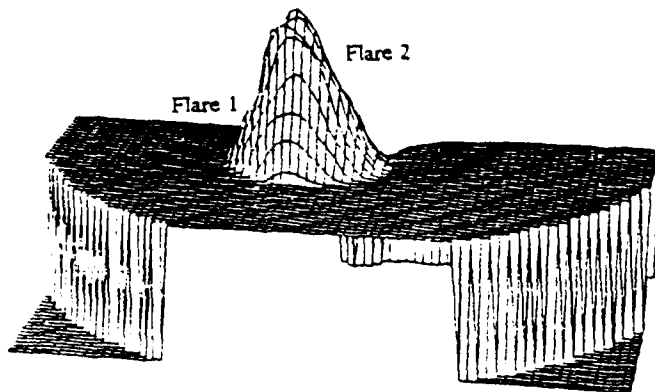
Total Pressure



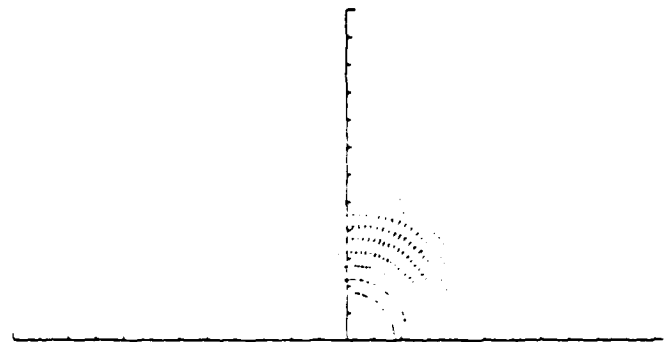
IMF Direction

6. Properties of simulated interplanetary medium at $t = 20.1 \text{ hr}$ (1906 UT, 4 February, 1986).

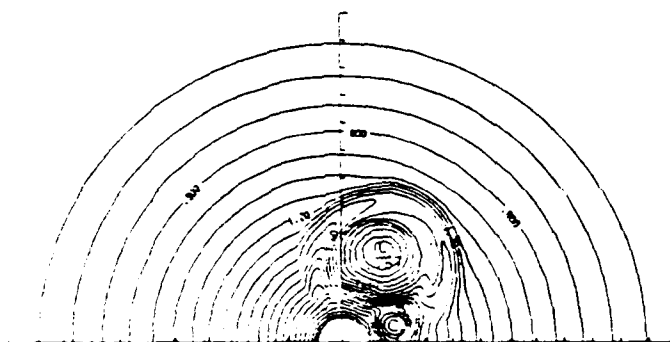
$t = 25.1$ hr



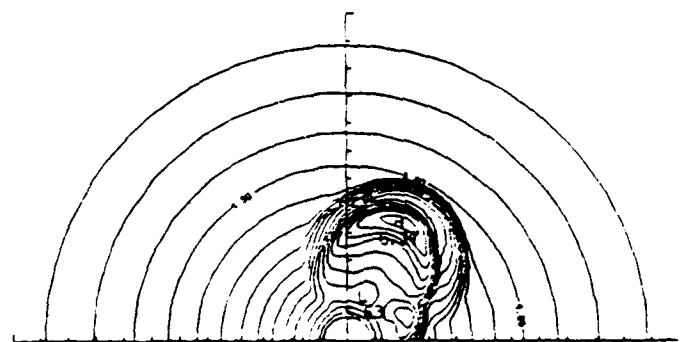
Solar Wind Speed



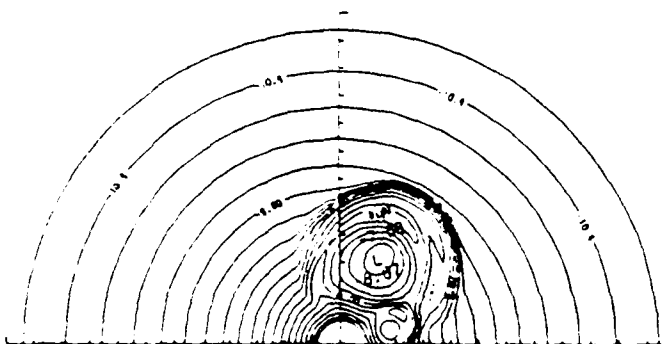
Velocity Increment
(maximum: 400 km/s)



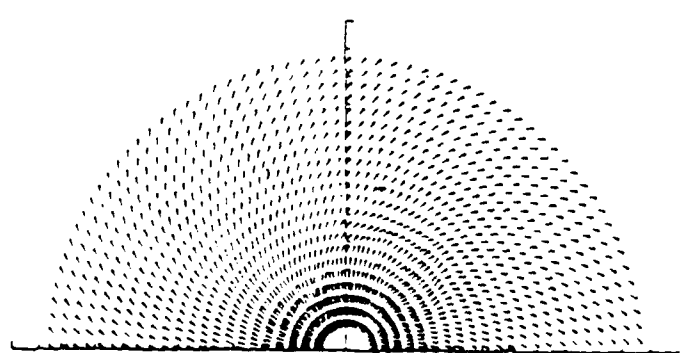
Proton Density



Temperature



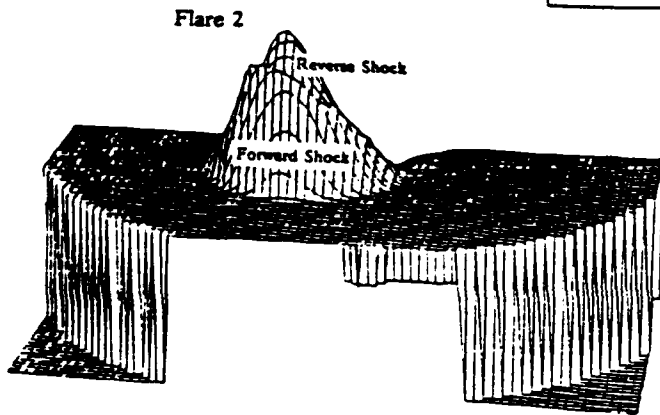
Total Pressure



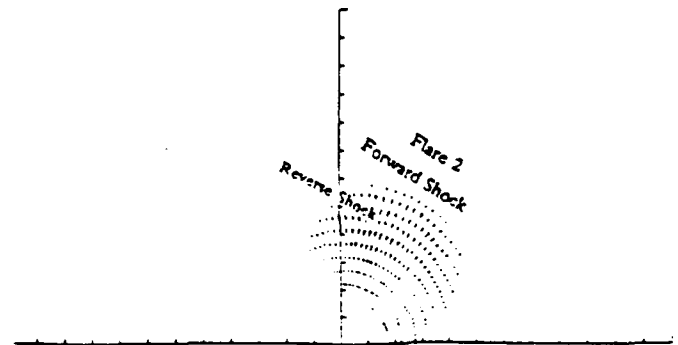
IMF Direction

7. Properties of simulated interplanetary medium at $t = 25.1$ hr (0006 UT, 5 February, 1986).

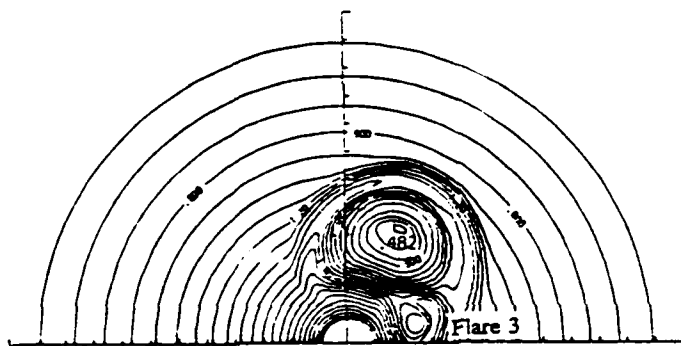
$t = 30.1 \text{ hr}$



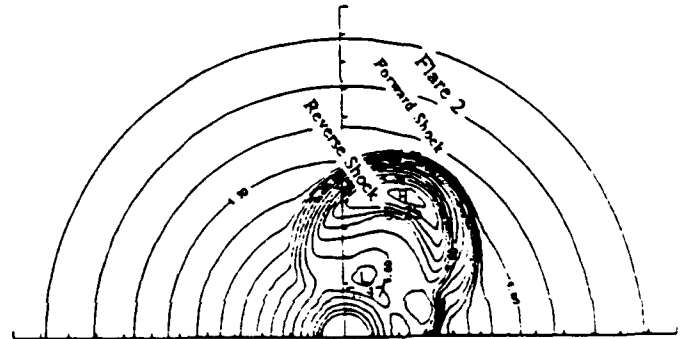
Solar Wind Speed



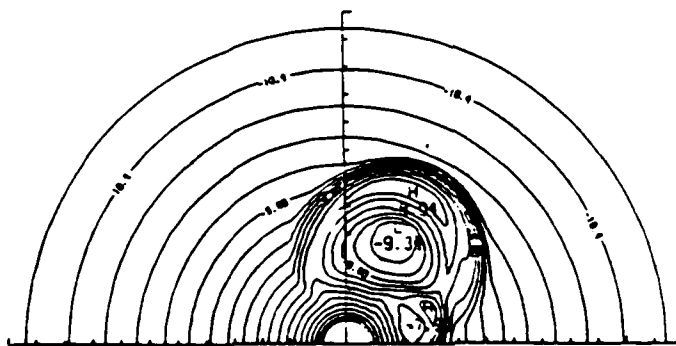
Velocity Increment
(maximum: 331 km/s)



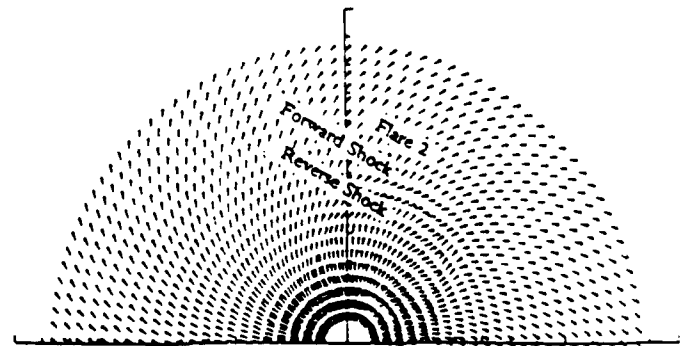
Proton Density



Temperature



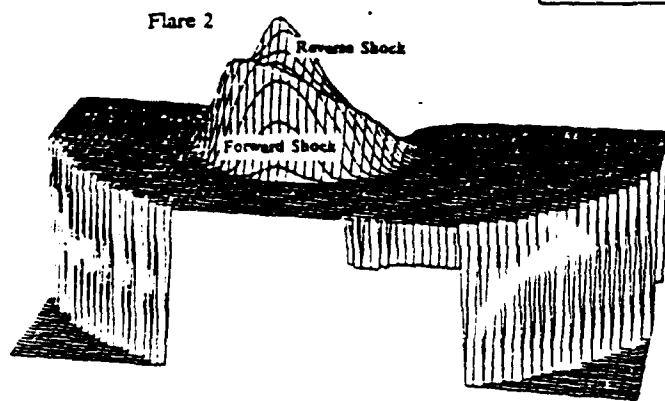
Total Pressure



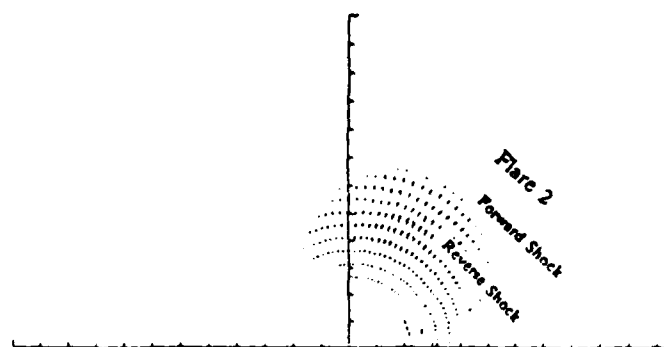
IMF Direction

8. Properties of simulated interplanetary medium at $t = 30.1 \text{ hr}$ (0506 UT, 5 February, 1986).

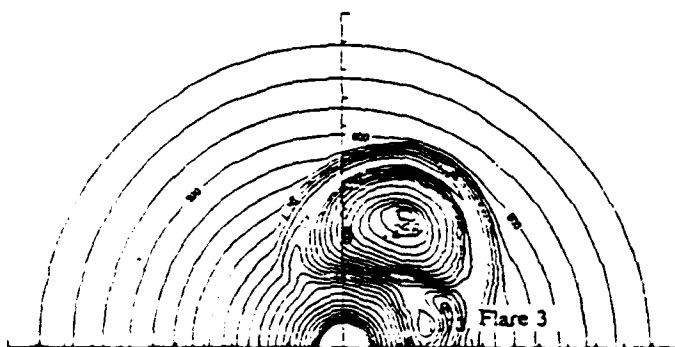
$t = 35.2 \text{ hr}$



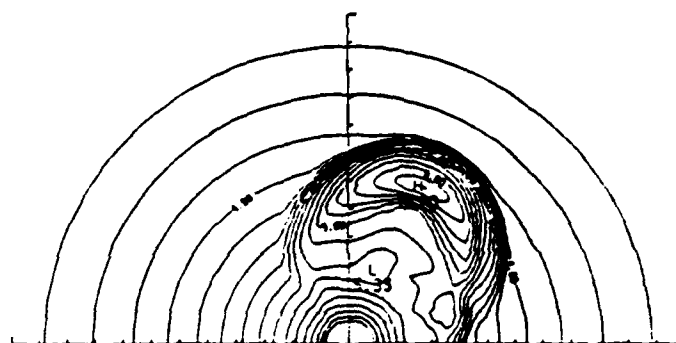
Solar Wind Speed



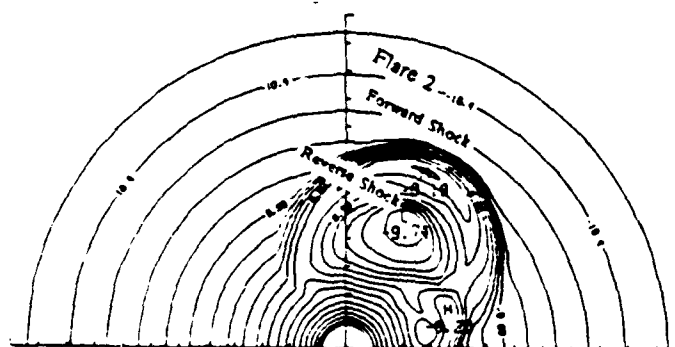
Velocity Increment
(maximum: 309 km/s)



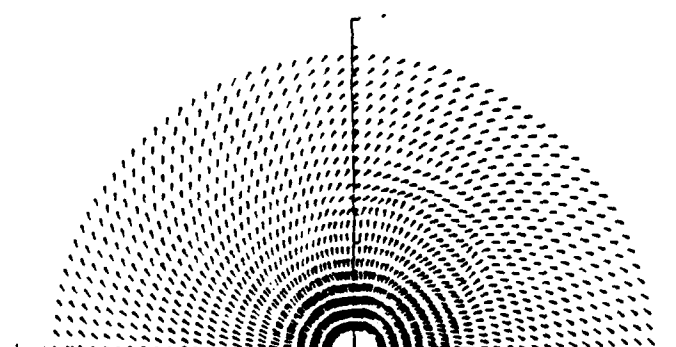
Proton Density



Temperature



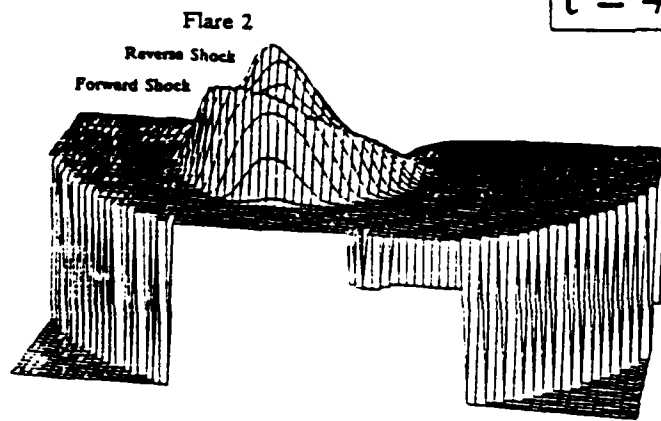
Total Pressure



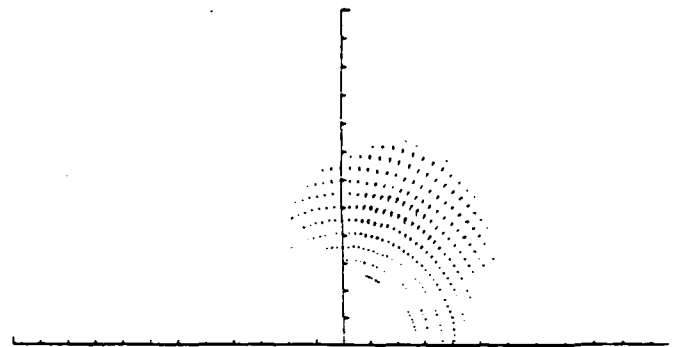
IMF Direction

9. Properties of simulated interplanetary medium at $t = 35.2 \text{ hr}$ (1012 UT, 5 February, 1986).

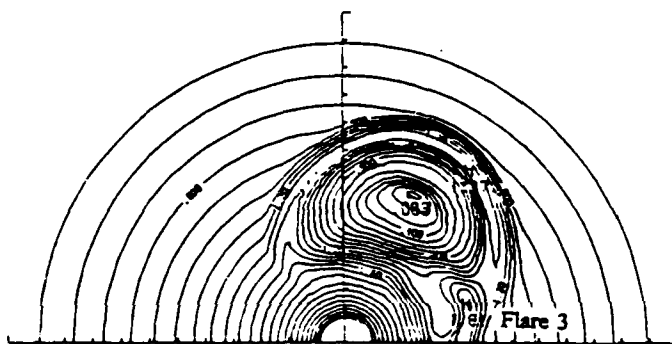
$t = 40.3 \text{ hr}$



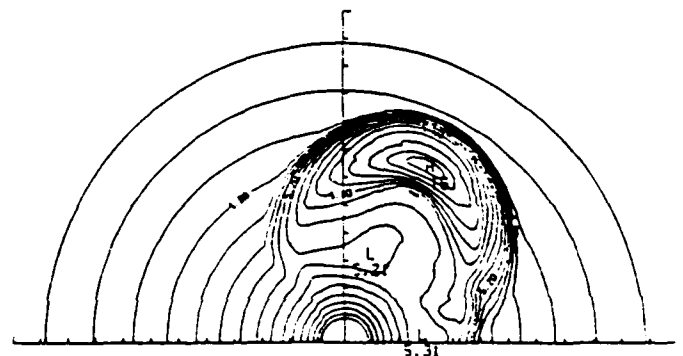
Solar Wind Speed



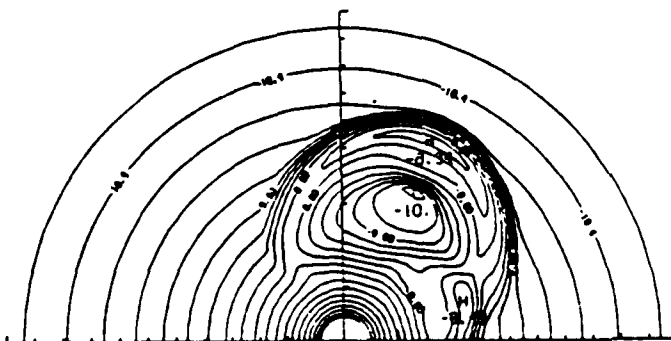
Velocity Increment
(maximum: 285 km/s)



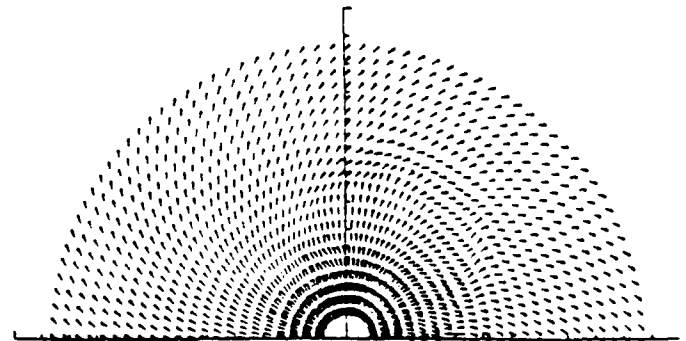
Proton Density



Temperature



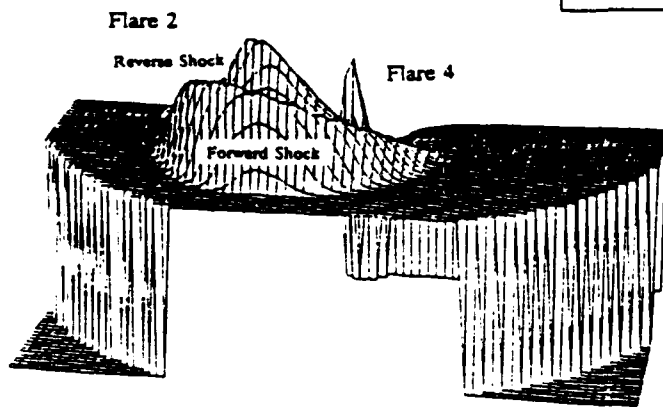
Total Pressure



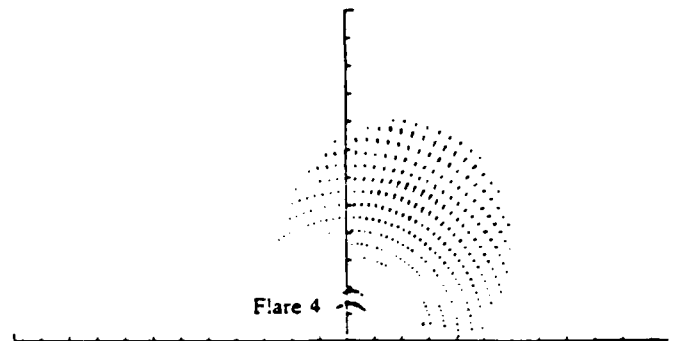
IMF Direction

10. Properties of simulated interplanetary medium at $t = 40.3 \text{ hr}$ (1518 UT, 5 February, 1986).

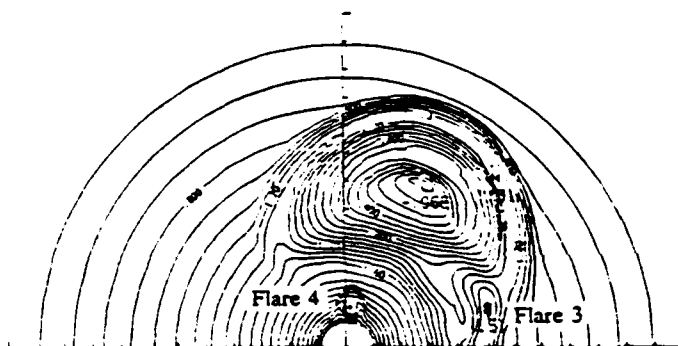
$t = 45.1 \text{ hr}$



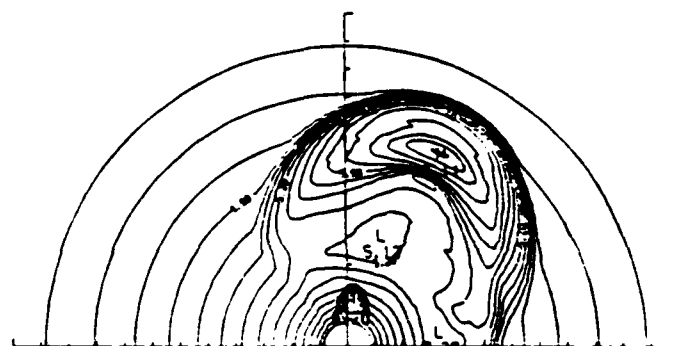
Solar Wind Speed



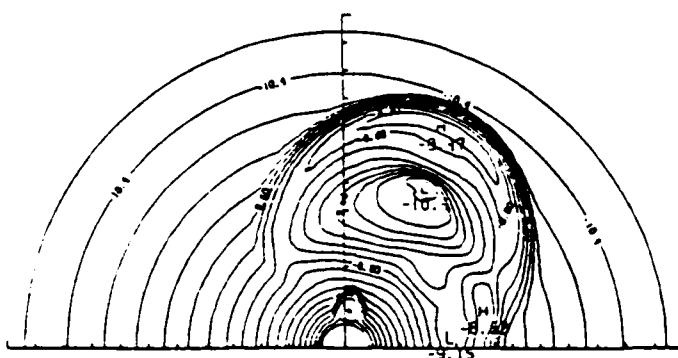
Velocity Increment
(maximum: 263 km/s)



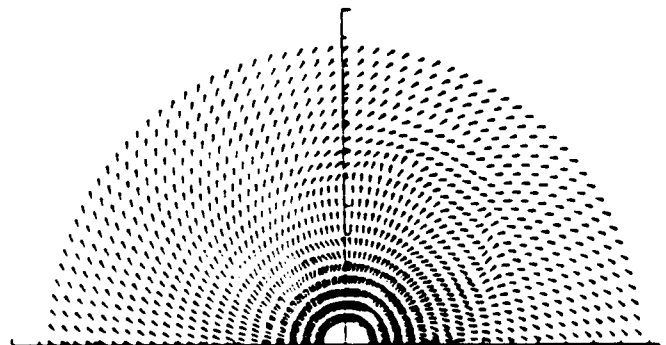
Proton Density



Temperature



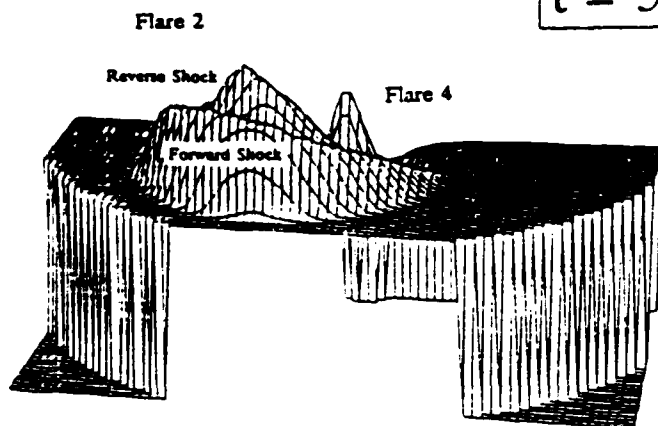
Total Pressure



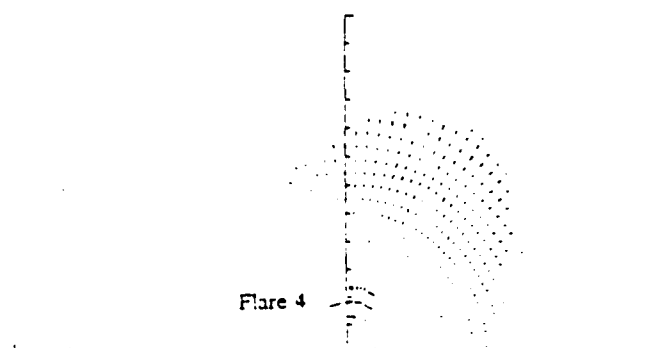
IMF Direction

11. Properties of simulated interplanetary medium at $t = 45.1 \text{ hr}$ (2006 UT, 5 February, 1986).

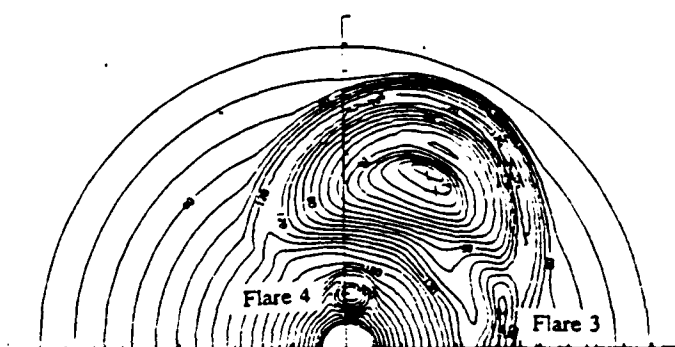
$t = 50.0$ hr



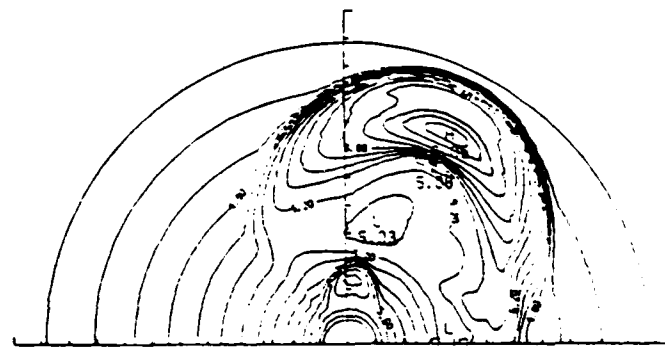
Solar Wind Speed



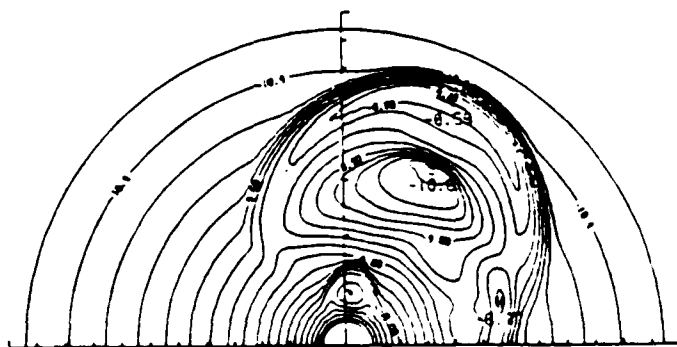
Velocity Increment
(maximum: 234 km/s)



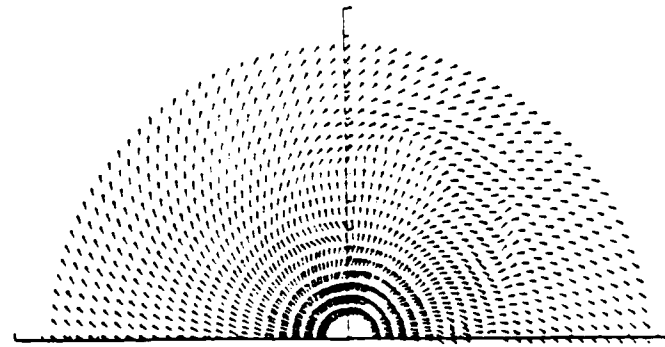
Proton Density



Temperature



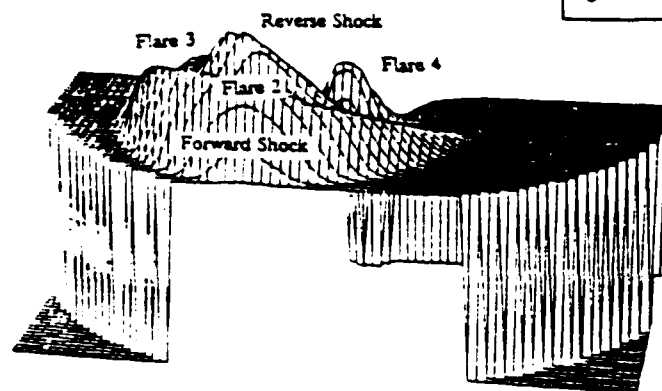
Total Pressure



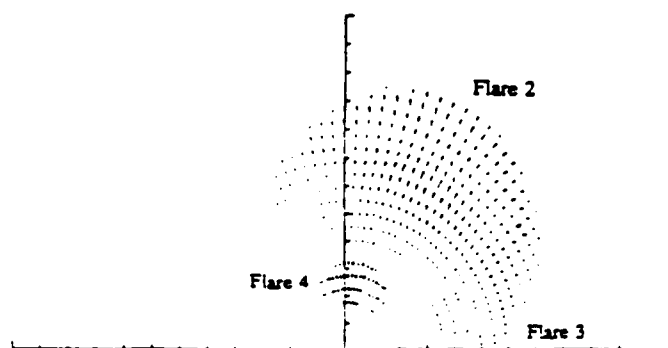
IMF Direction

12. Properties of simulated interplanetary medium at $t = 50.0$ hr (0100 UT, 6 February, 1986).

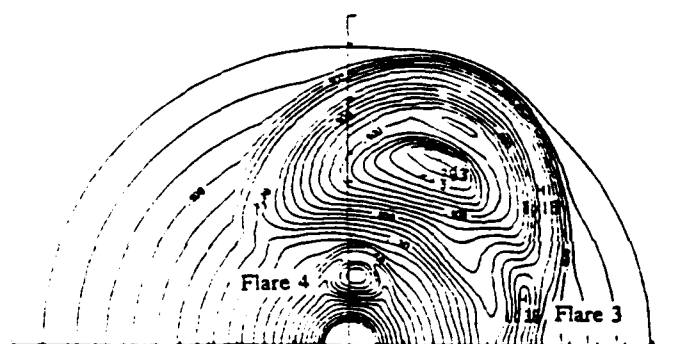
$t = 55.1 \text{ hr}$



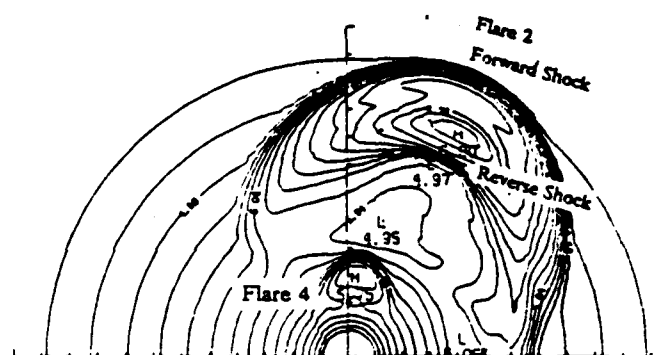
Solar Wind Speed



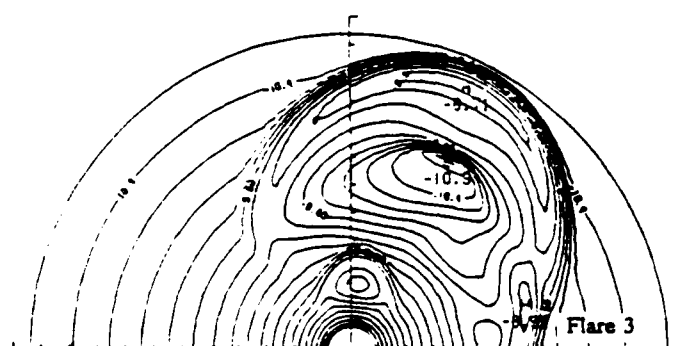
Velocity Increment
(maximum: 208 km/s)



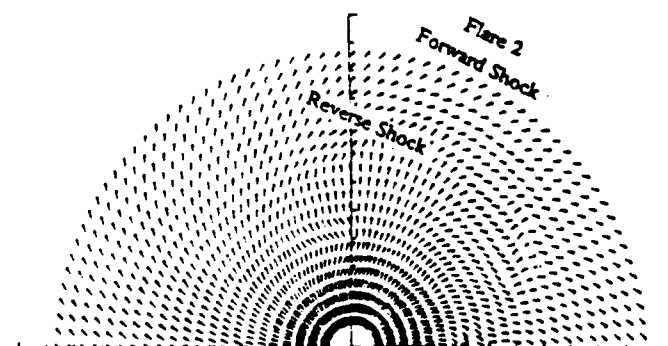
Proton Density



Temperature



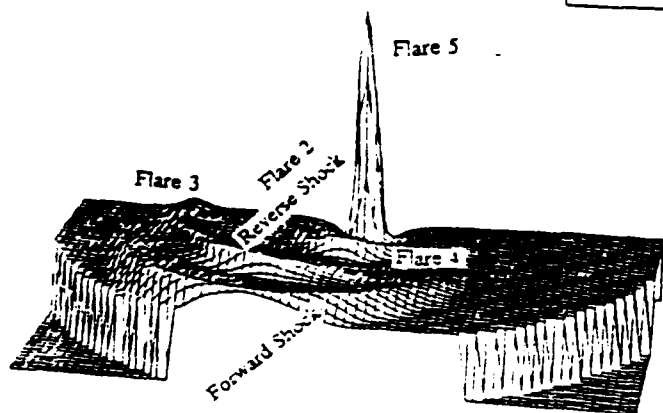
Total Pressure



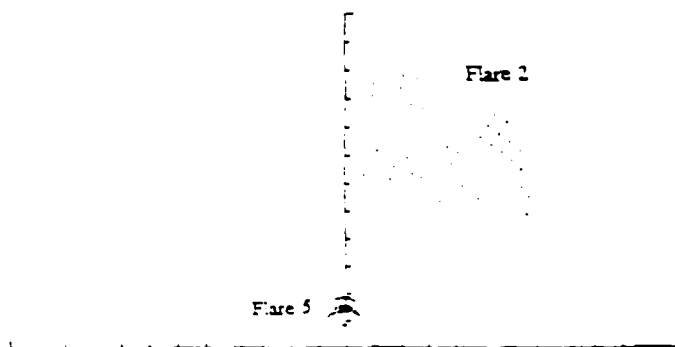
IMF Direction

13. Properties of simulated interplanetary medium at $t = 55.1 \text{ hr}$ (0606 UT, 6 February, 1986).

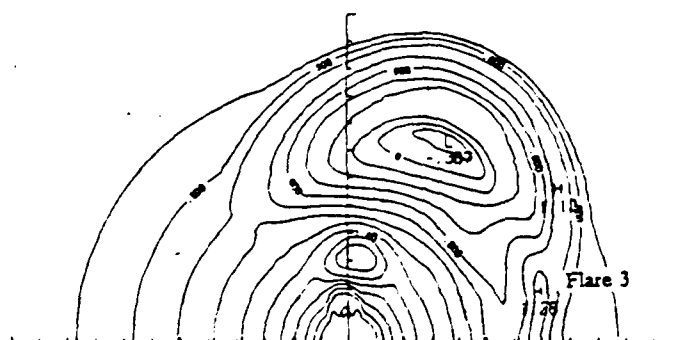
$t = 60.0 \text{ hr}$



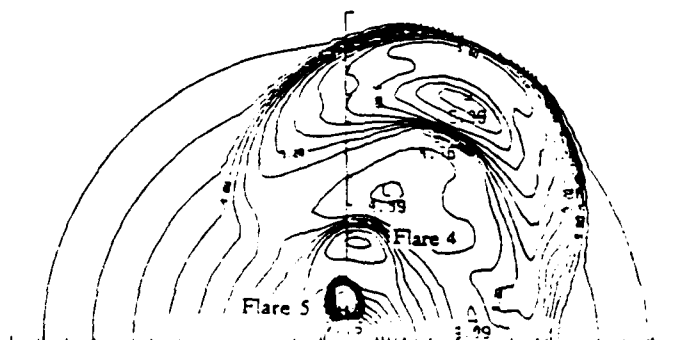
Solar Wind Speed



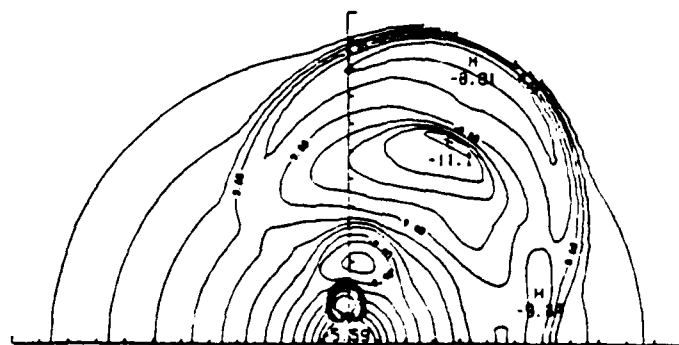
Velocity Increment
(maximum: 1290 km/s)



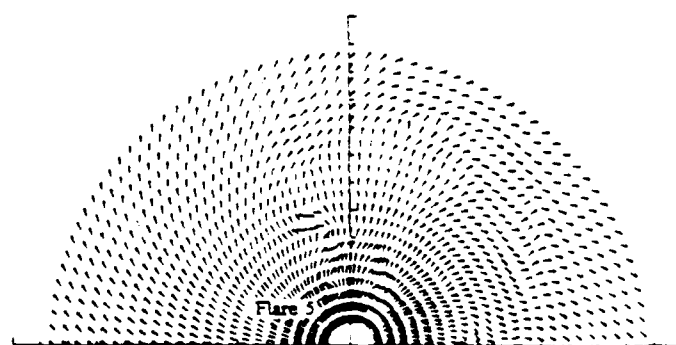
Proton Density



Temperature



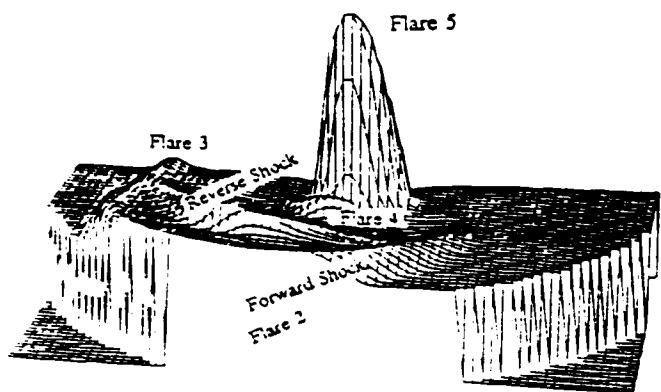
Total Pressure



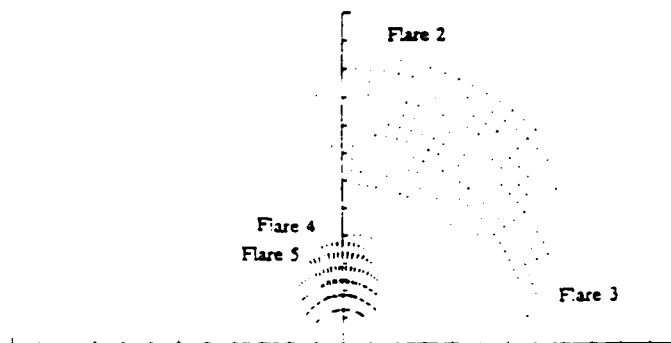
IMF Direction

14. Properties of simulated interplanetary medium at $t = 60.0 \text{ hr}$ (1100 UT, 6 February, 1986).

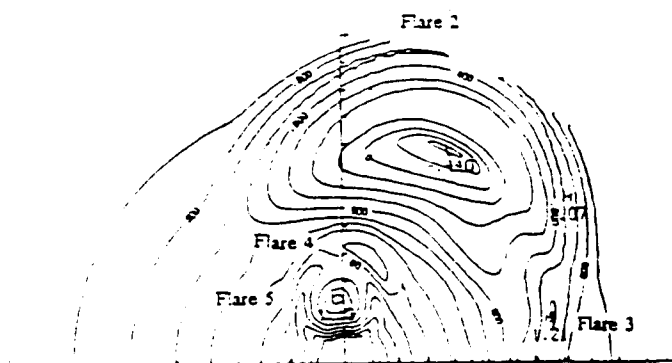
$t = 65.2 \text{ hr}$



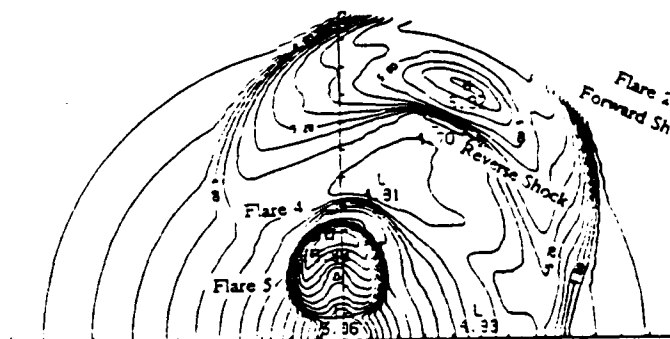
Solar Wind Speed



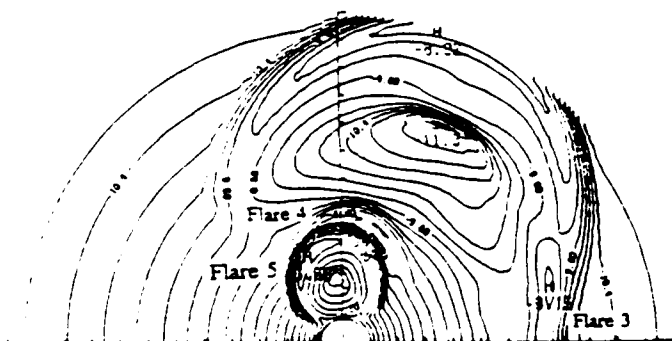
Velocity Increment
(maximum: 784 km/s)



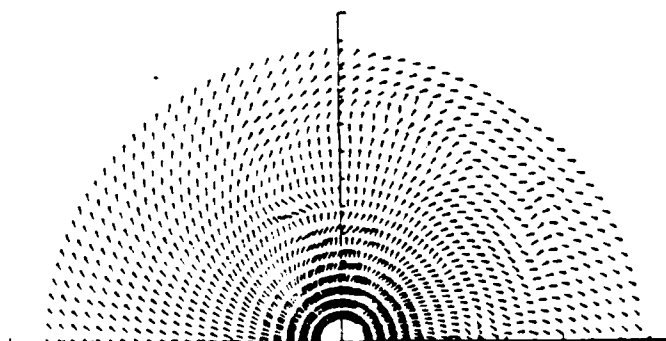
Proton Density



Temperature



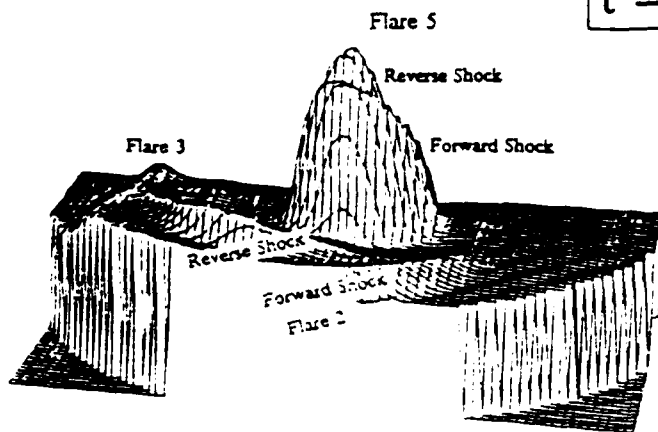
Total Pressure



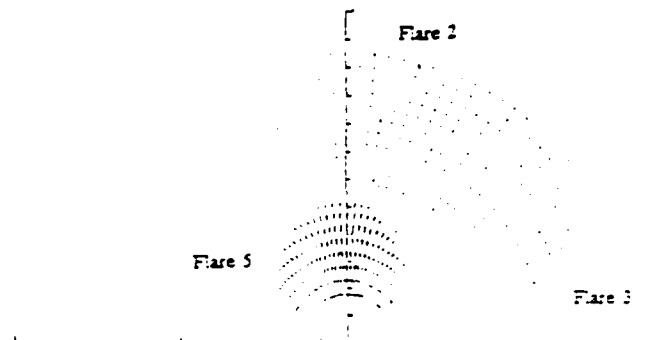
IMF Direction

15. Properties of simulated interplanetary medium at $t = 65.2 \text{ hr}$ (1612 UT, 6 February, 1986).

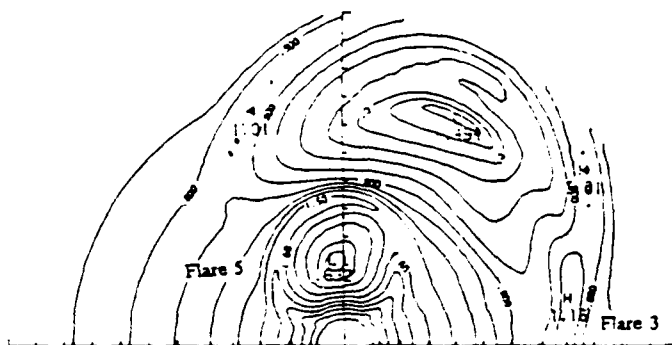
$t = 70.2 \text{ hr}$



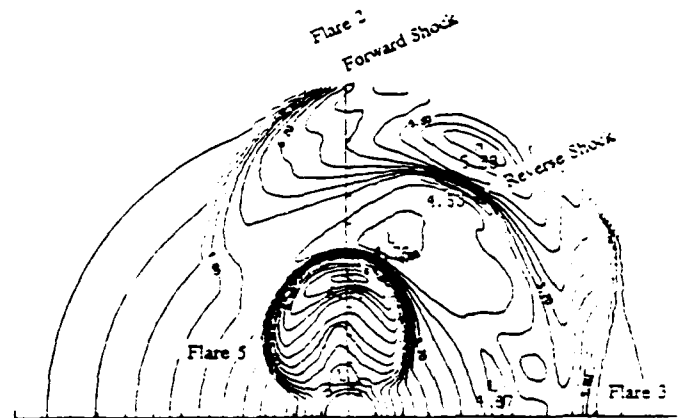
Solar Wind Speed



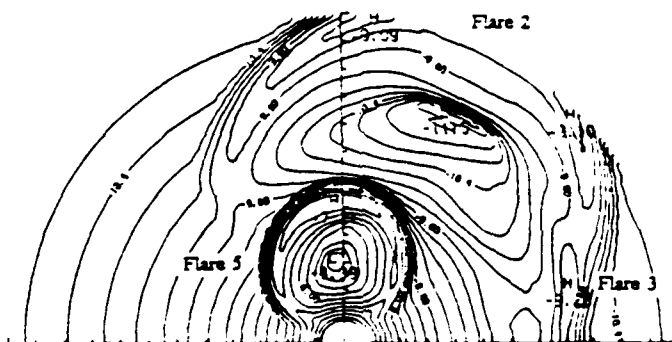
Velocity Increment
(maximum: 582 km/s)



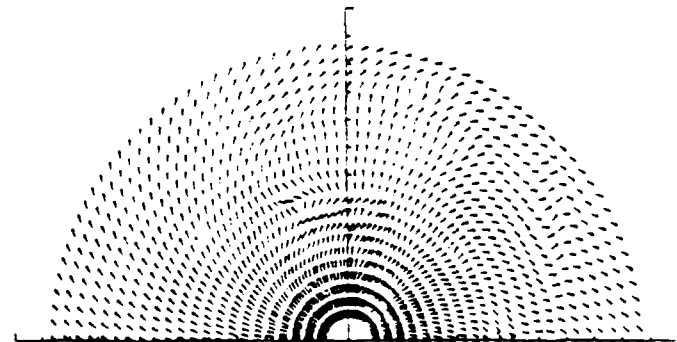
Proton Density



Temperature

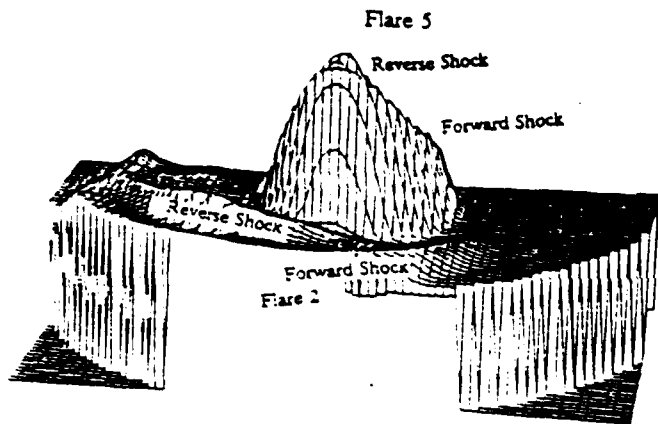


Total Pressure

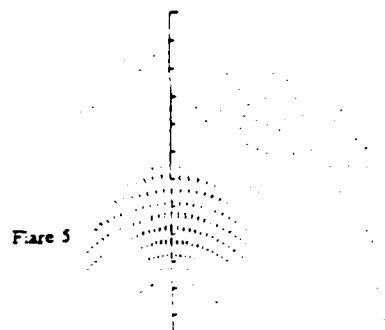


IMF Direction

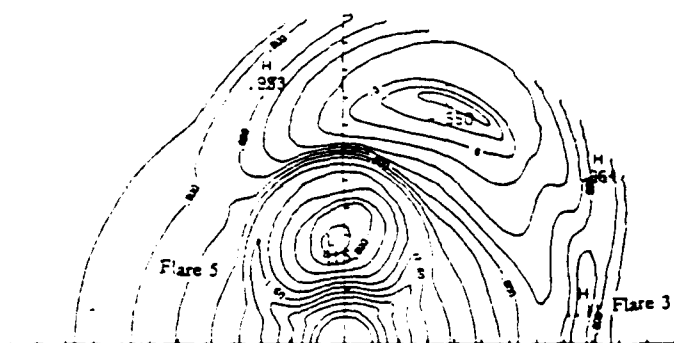
16. Properties of simulated interplanetary medium at $t = 70.2 \text{ hr}$ (2112 UT, 6 February, 1986).

$$t = 75.0 \text{ hr}$$


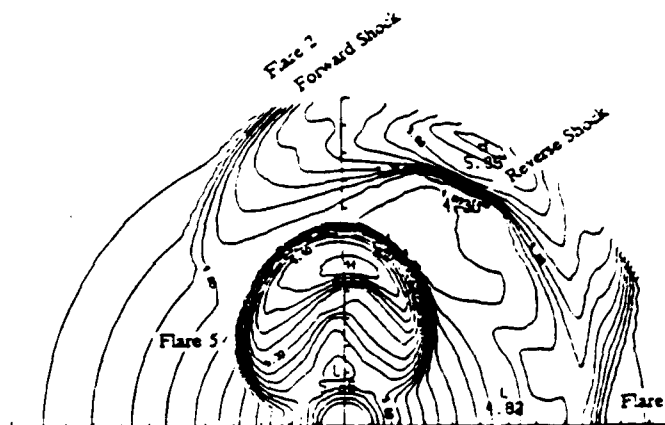
Solar Wind Speed



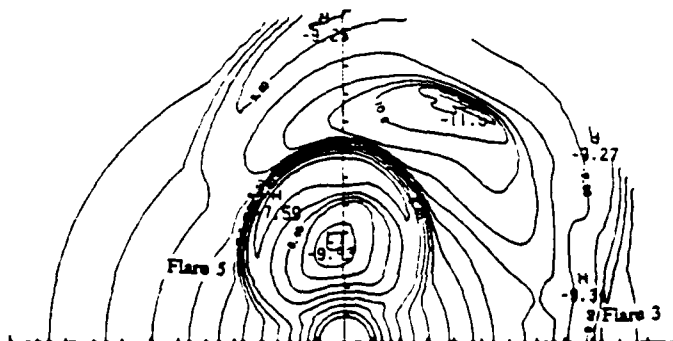
Velocity Increment
(maximum: 497 km/s)



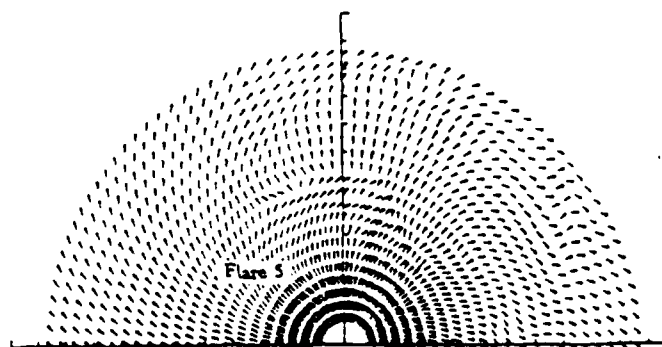
Proton Density



Temperature



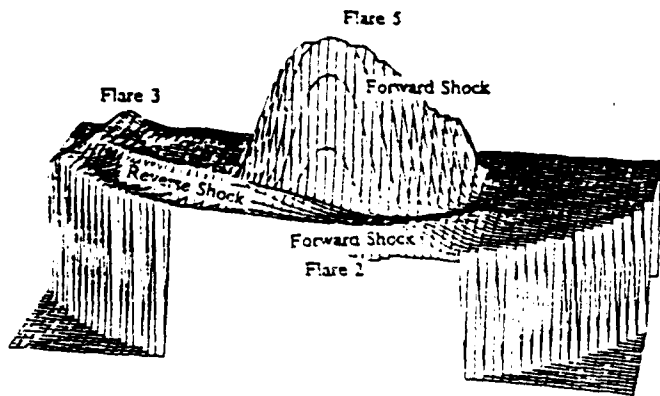
Total Pressure



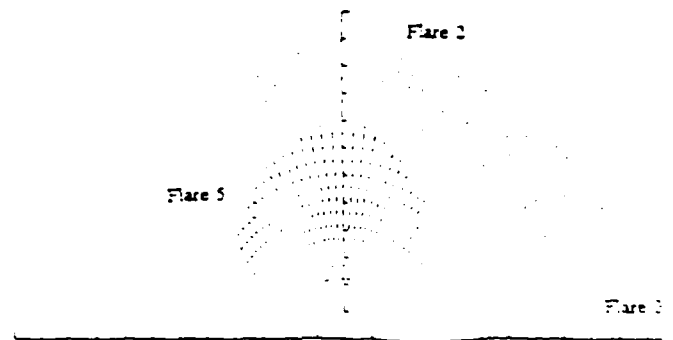
IMF Direction

17. Properties of simulated interplanetary medium at $t = 75.0$ hr (0200 UT, 7 February, 1986).

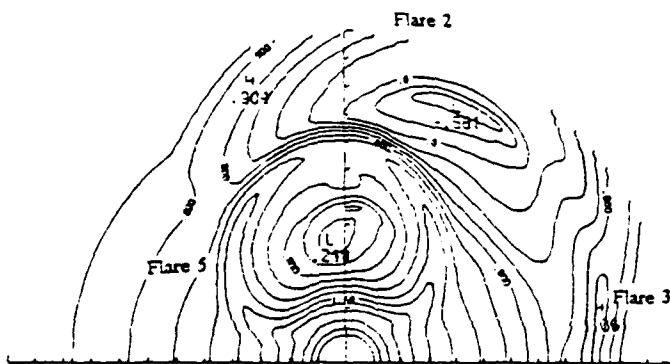
$t = 80.1 \text{ hr}$



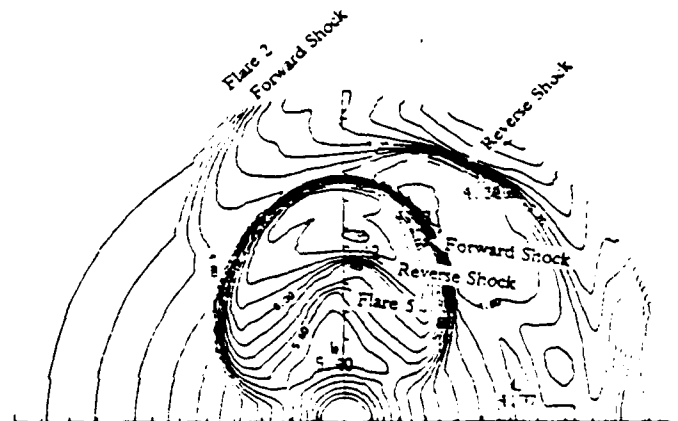
Solar Wind Speed



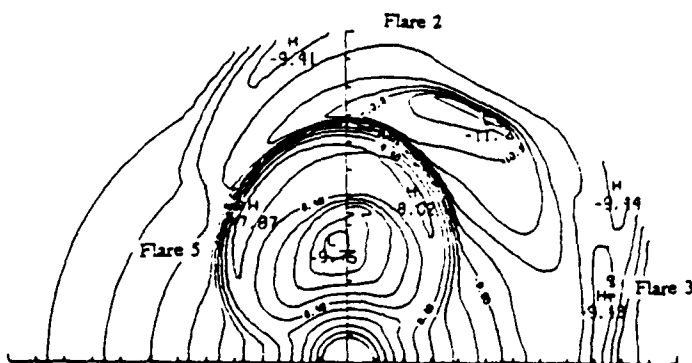
Velocity Increment
(maximum: 479 km/s)



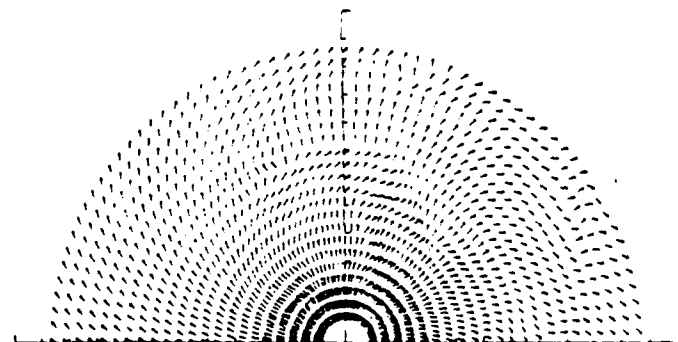
Proton Density



Temperature



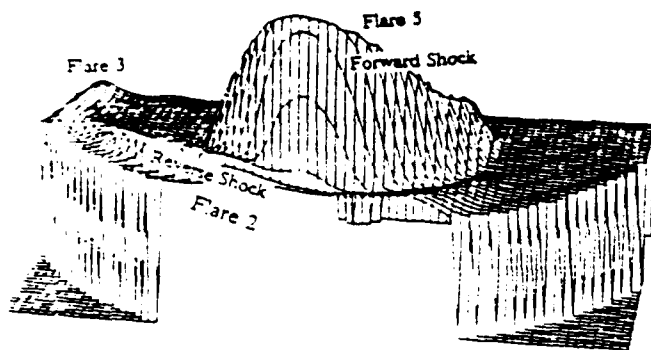
Total Pressure



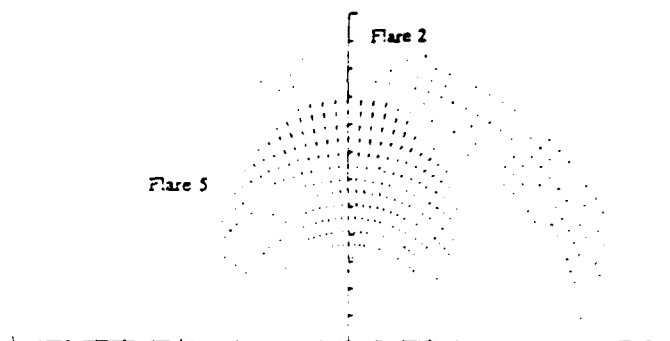
IMF Direction

18. Properties of simulated interplanetary medium at $t = 80.1 \text{ hr}$ (0706 UT, 7 February, 1986).

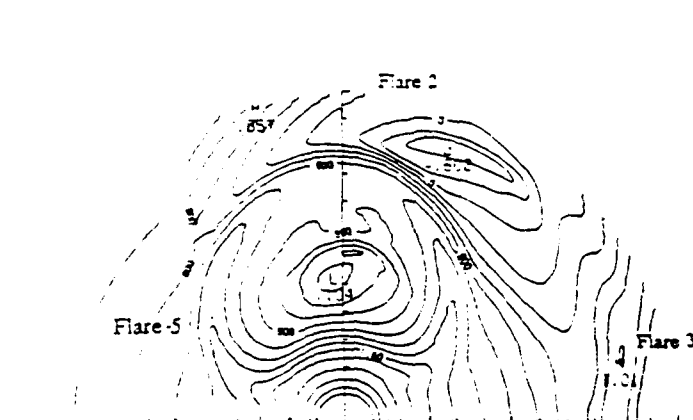
$t = 85.2 \text{ hr}$



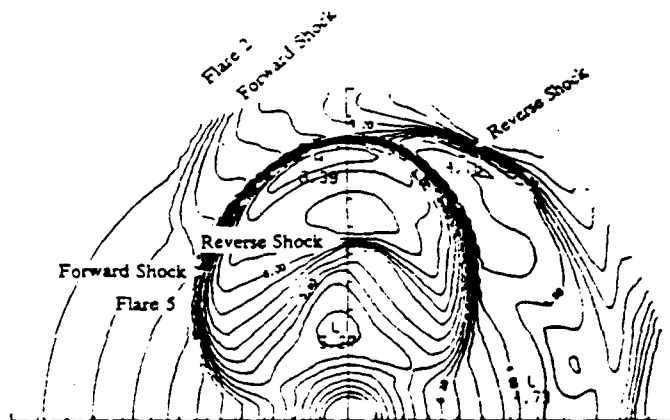
Solar Wind Speed



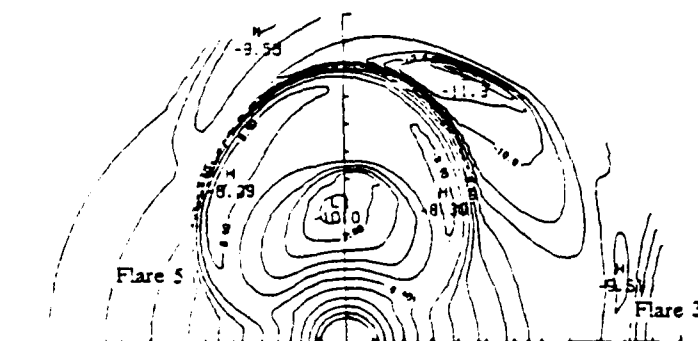
Velocity Increment
(maximum: 509 km/s)



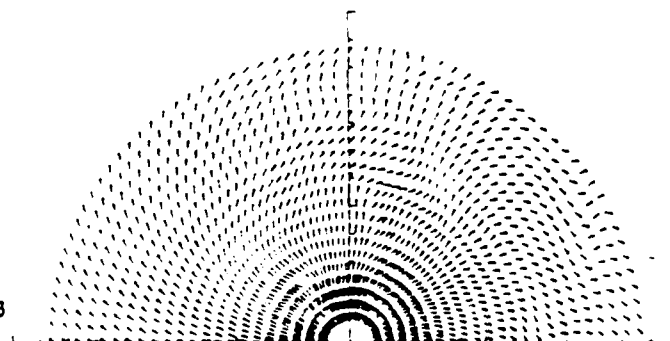
Proton Density



Temperature



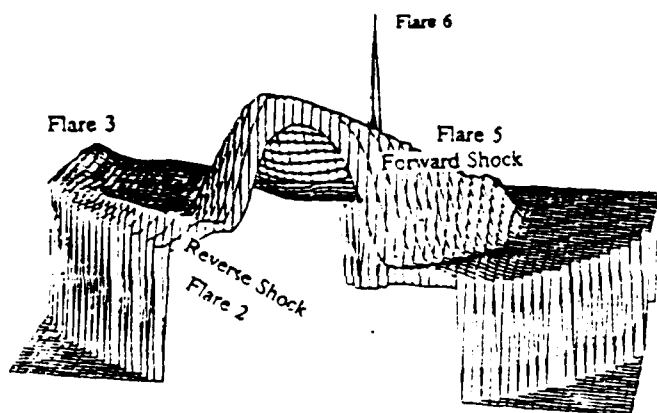
Total Pressure



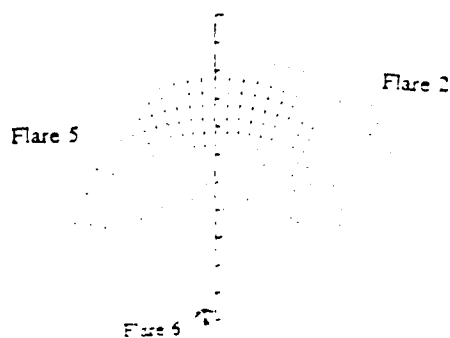
IMF Direction

19. Properties of simulated interplanetary medium at $t = 85.2 \text{ hr}$ (1212 UT, 7 February, 1986).

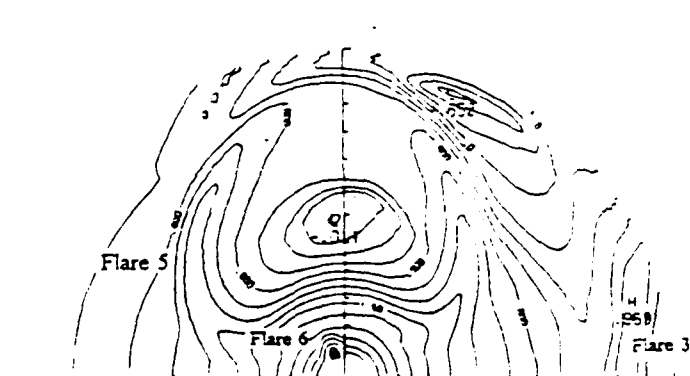
$t = 90.0 \text{ hr}$



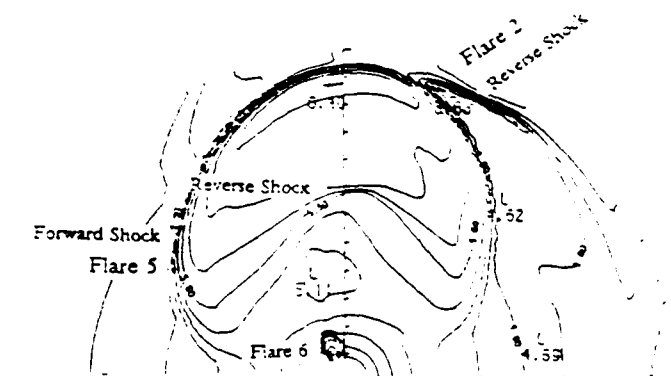
Solar Wind Speed



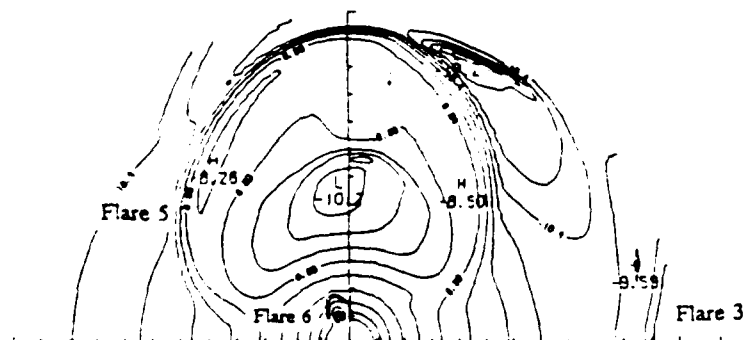
Velocity Increment
(maximum: 734 km/s)



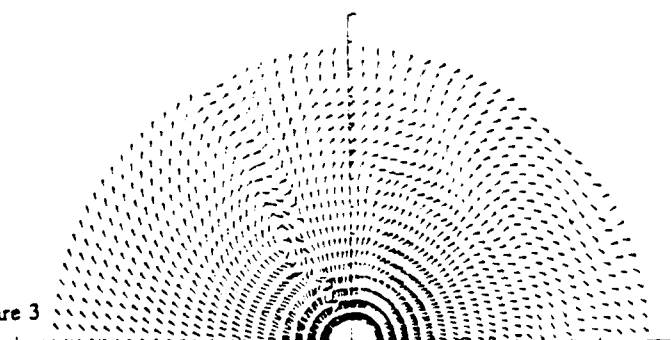
Proton Density



Temperature



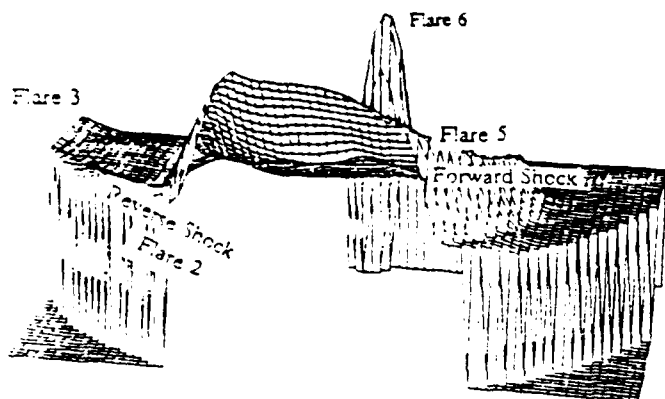
Total Pressure



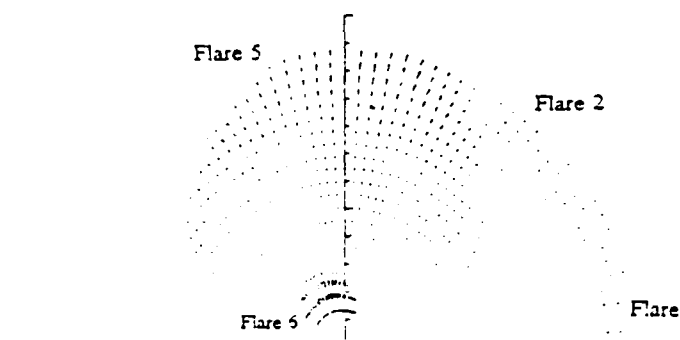
IMF Direction

20. Properties of simulated interplanetary medium at $t = 90.0 \text{ hr}$ (1700 UT, 7 February, 1986).

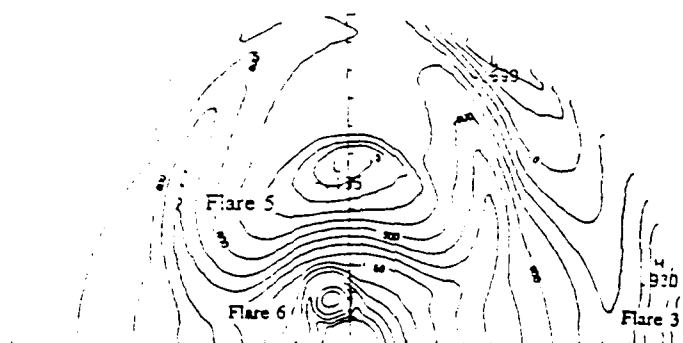
$t = 95.1$ hr



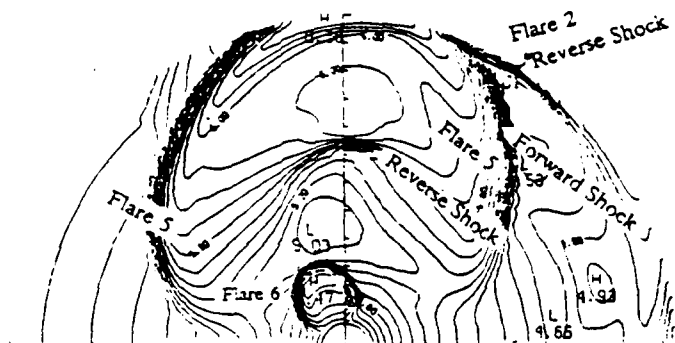
Solar Wind Speed



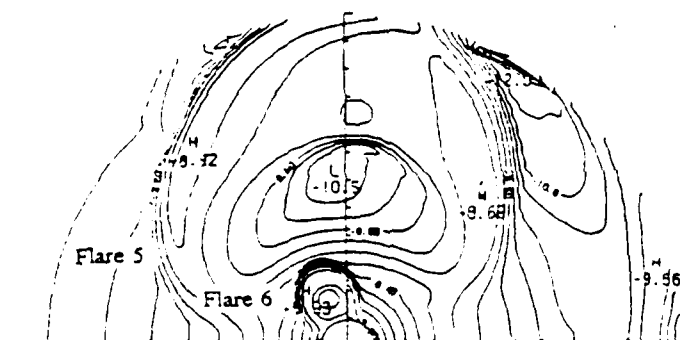
Velocity Increment
(maximum: 484 km/s)



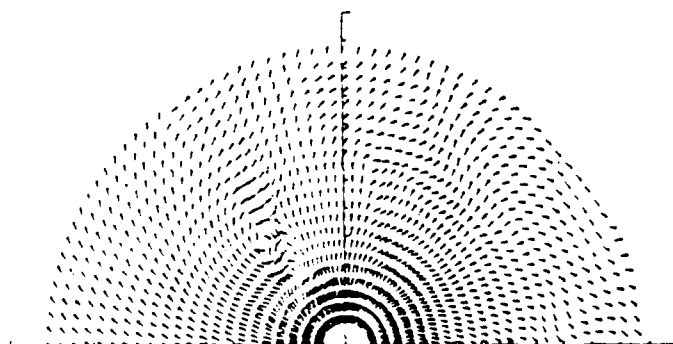
Proton Density



Temperature



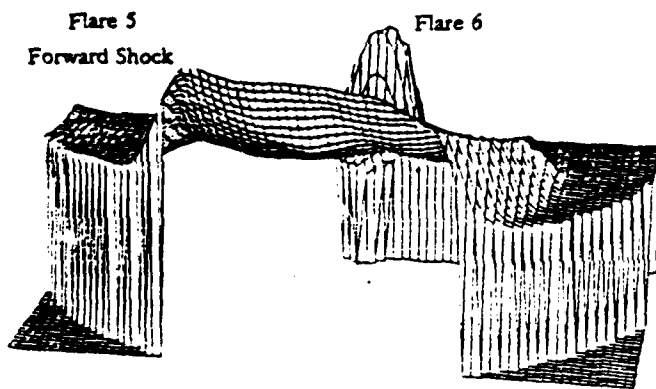
Total Pressure



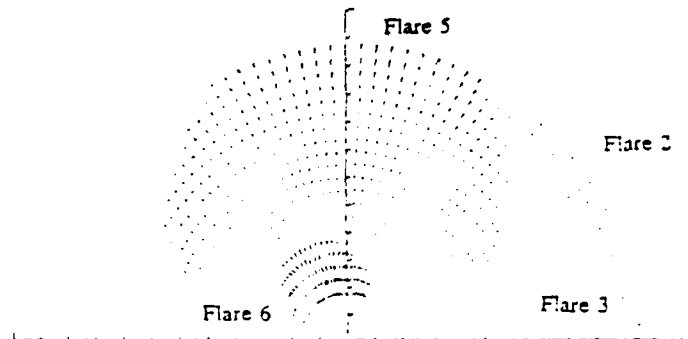
IMF Direction

21. Properties of simulated interplanetary medium at $t = 95.1$ hr (2206 UT, 7 February, 1986).

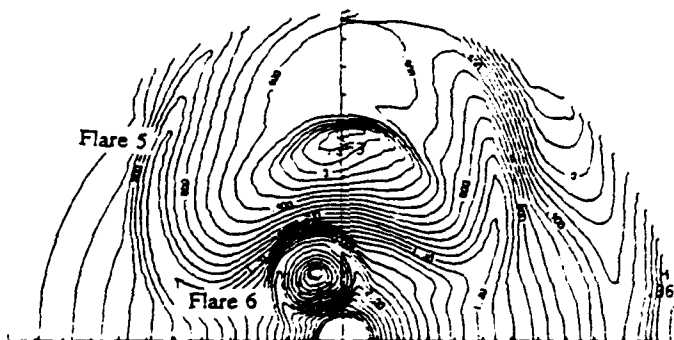
$t = 100.2 \text{ hr}$



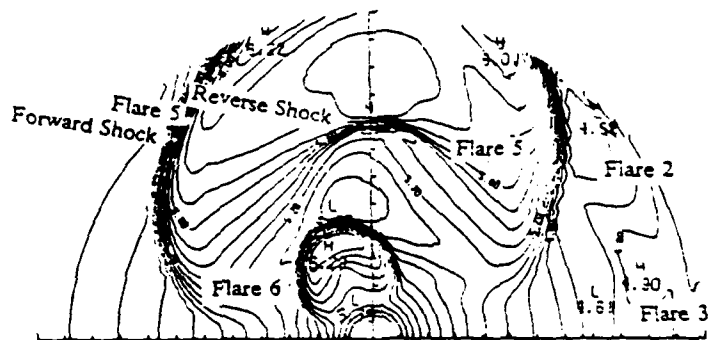
Solar Wind Speed



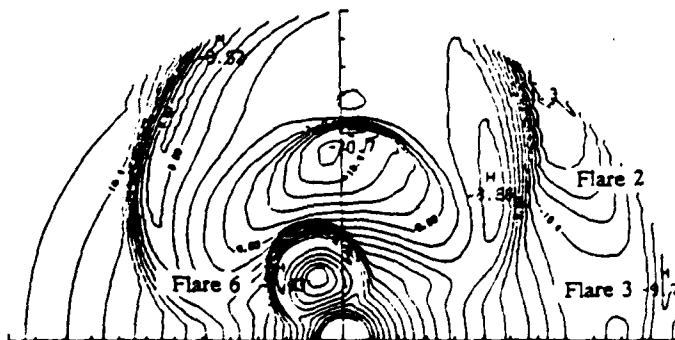
Velocity Increment
(maximum: 426 km/s)



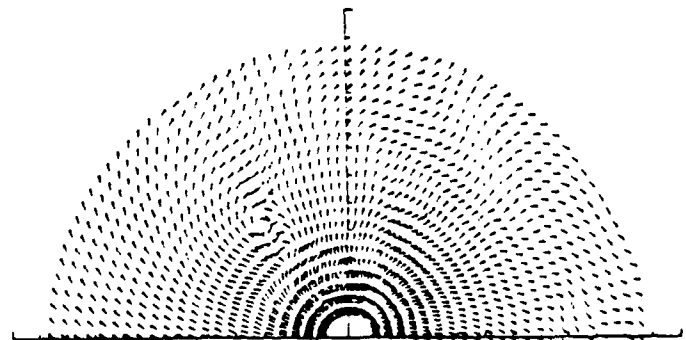
Proton Density



Temperature



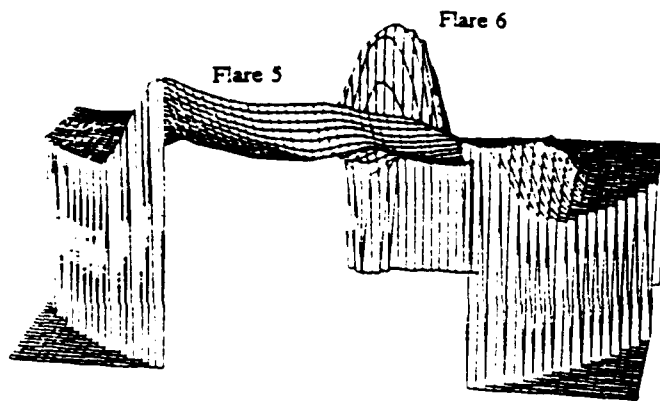
Total Pressure



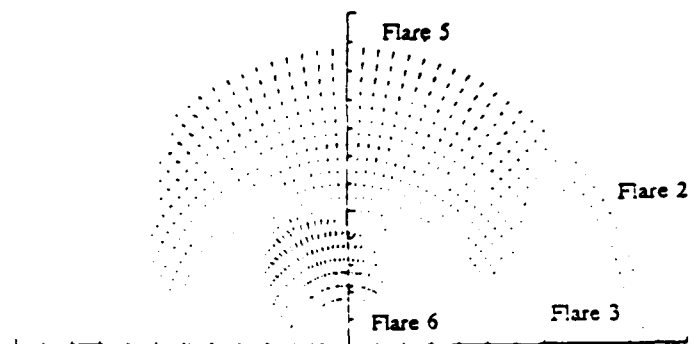
IMF Direction

22. Properties of simulated interplanetary medium at $t = 100.2 \text{ hr}$ (0312 UT, 7 February, 1986).

$t = 105.2$ hr



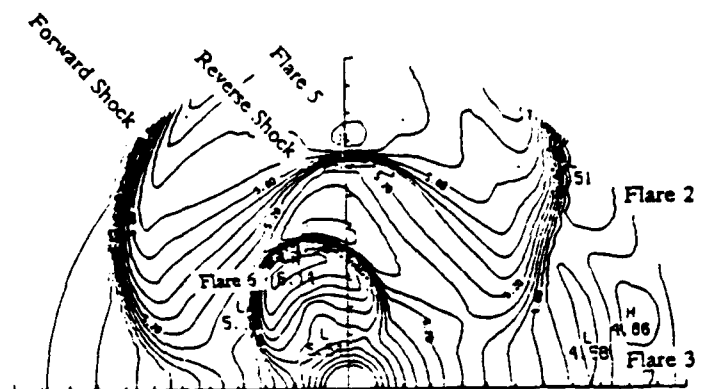
Solar Wind Speed



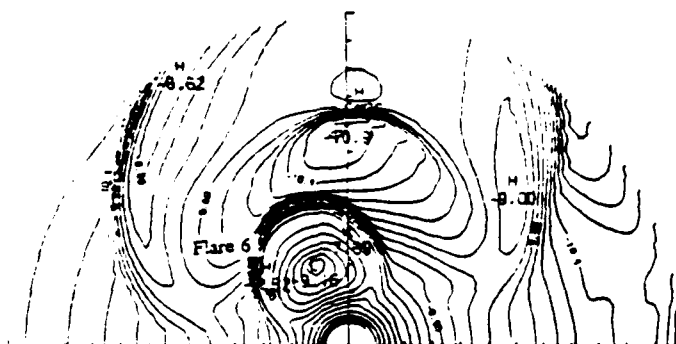
Velocity Increment
(maximum: 350 km/s)



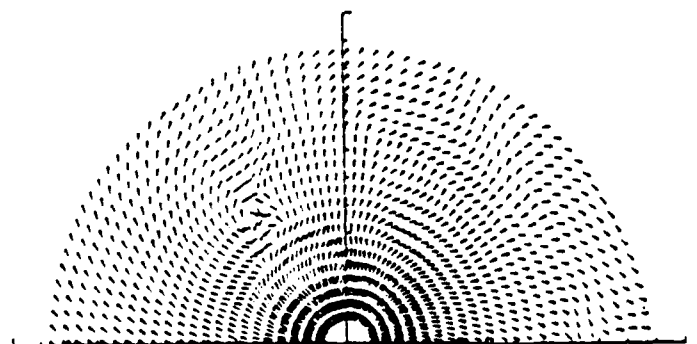
Proton Density



Temperature



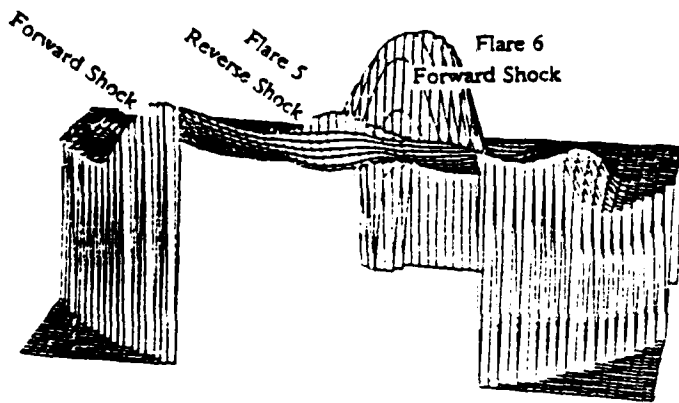
Total Pressure



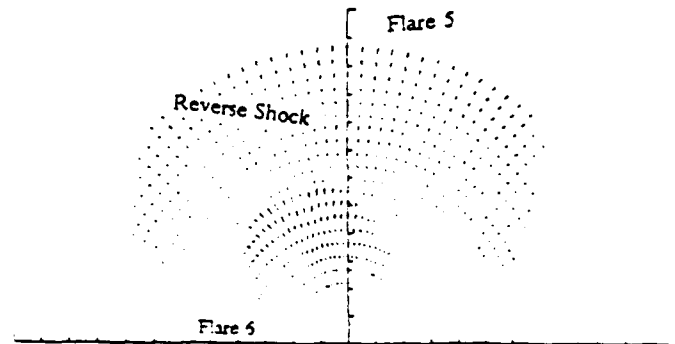
IMF Direction

23. Properties of simulated interplanetary medium at $t = 105.2$ hr (0812 UT, 7 February, 1986).

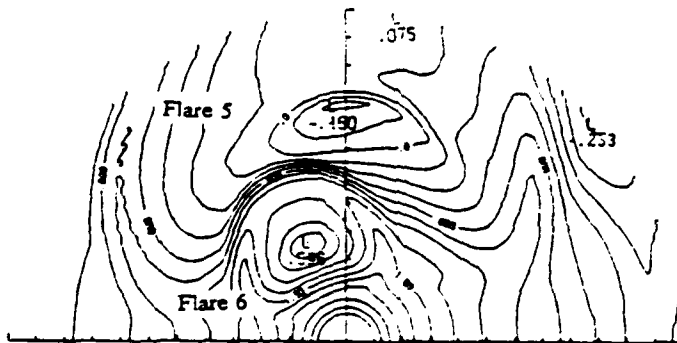
$t = 110.1 \text{ hr}$



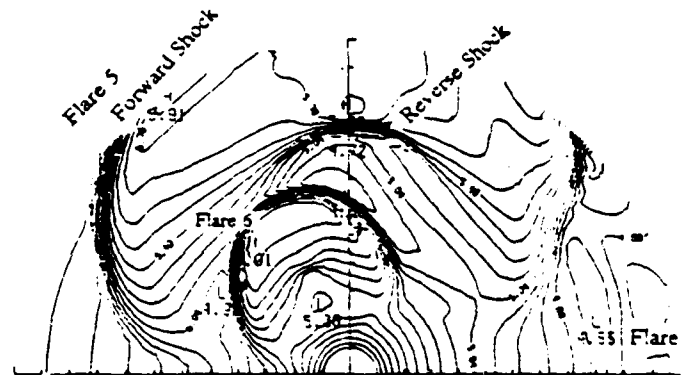
Solar Wind Speed



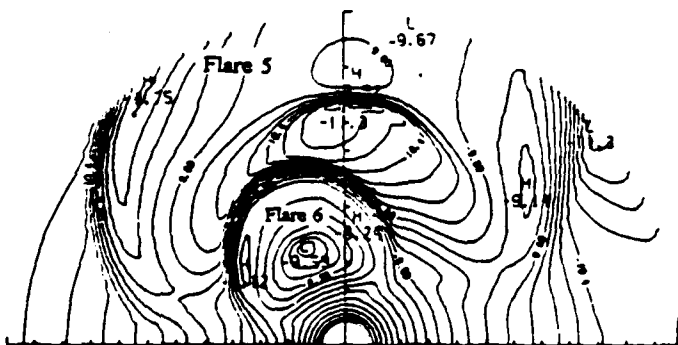
Velocity Increment
(maximum: 362 km/s)



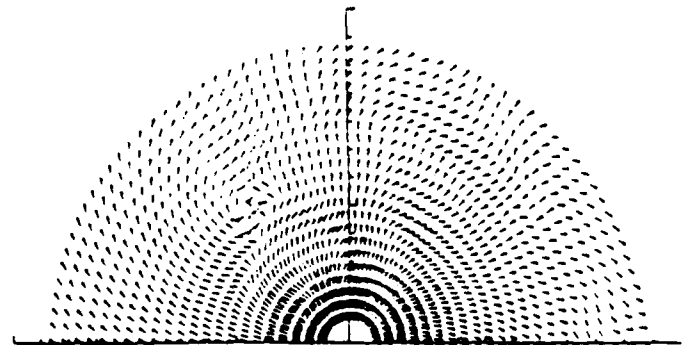
Proton Density



Temperature



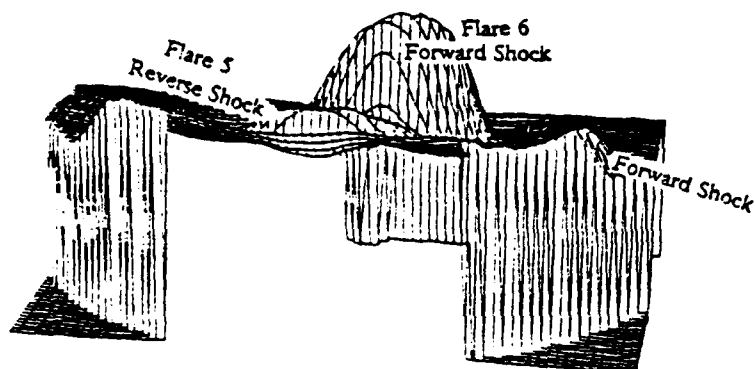
Total Pressure



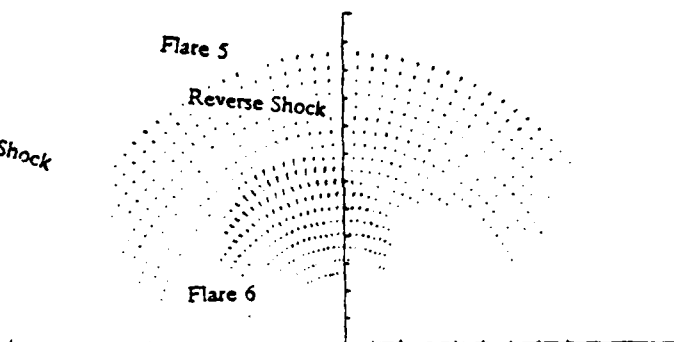
IMF Direction

24. Properties of simulated interplanetary medium at $t = 110.1 \text{ hr}$ (1306 UT, 7 February, 1986).

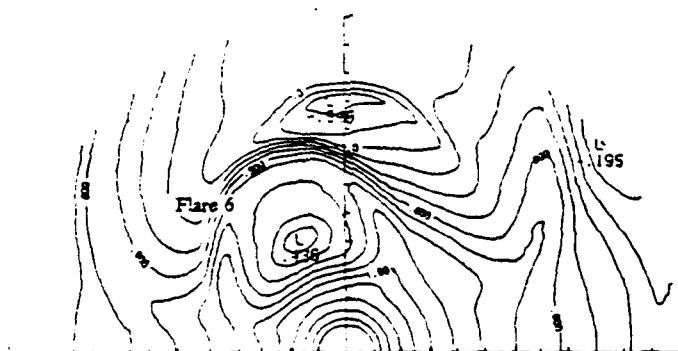
$t = 115.1 \text{ hr}$



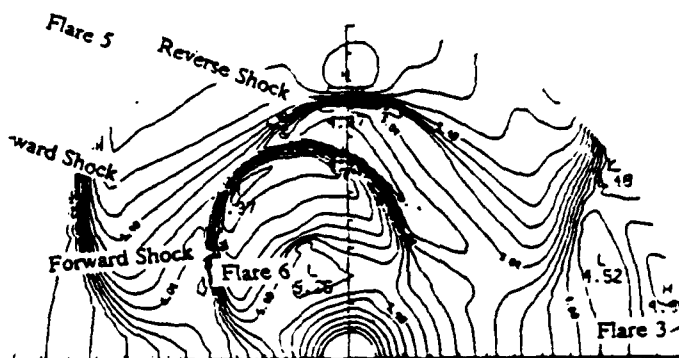
Solar Wind Speed



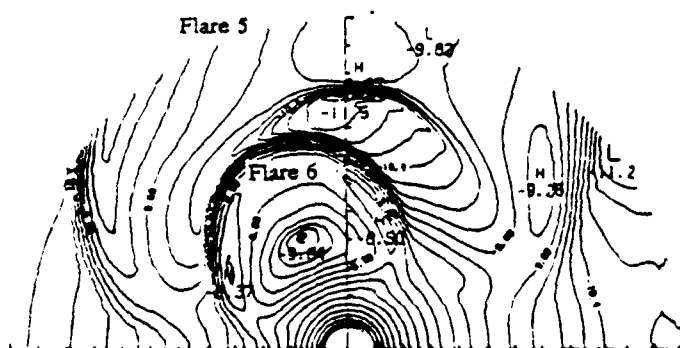
Velocity Increment
(maximum: 368 km/s)



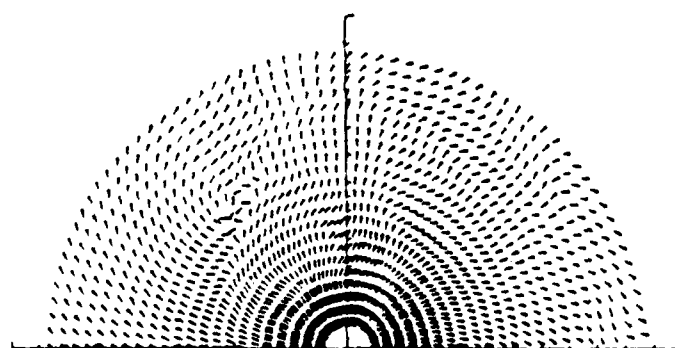
Proton Density



Temperature



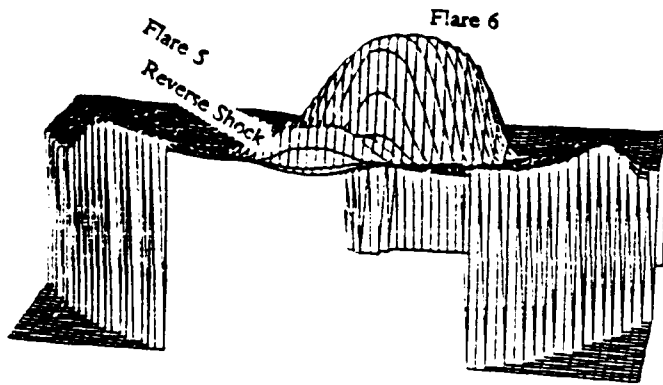
Total Pressure



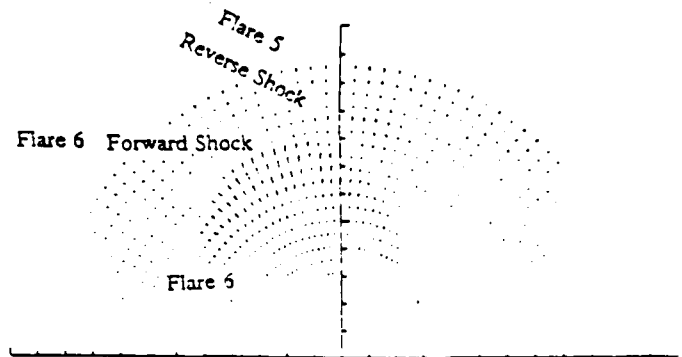
IMF Direction

25. Properties of simulated interplanetary medium at $t = 115.1 \text{ hr}$ (1806 UT, 7 February, 1986).

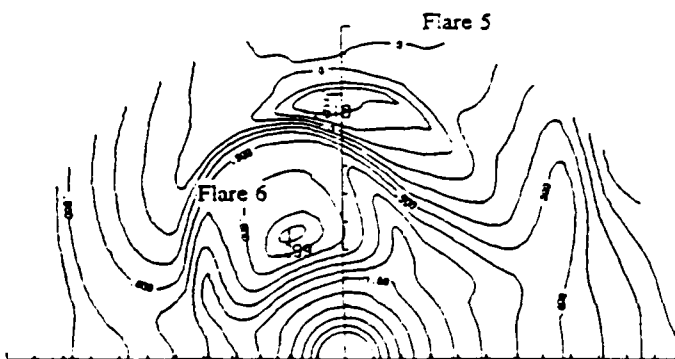
$t = 120.1$ hr



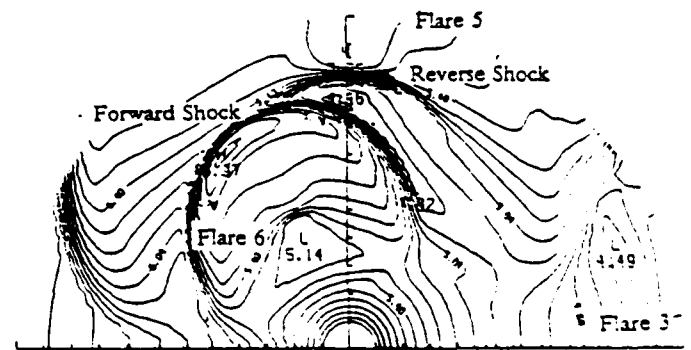
Solar Wind Speed



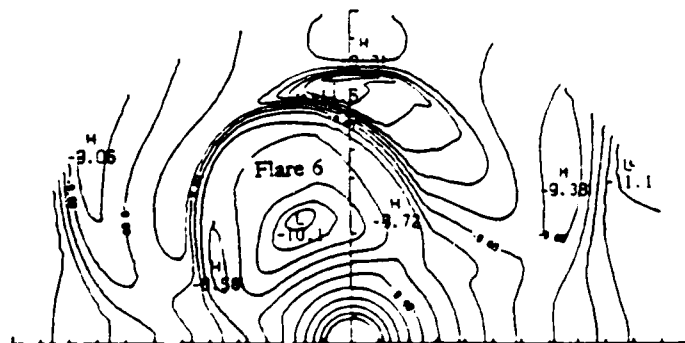
Velocity Increment
(maximum: 369 km/s)



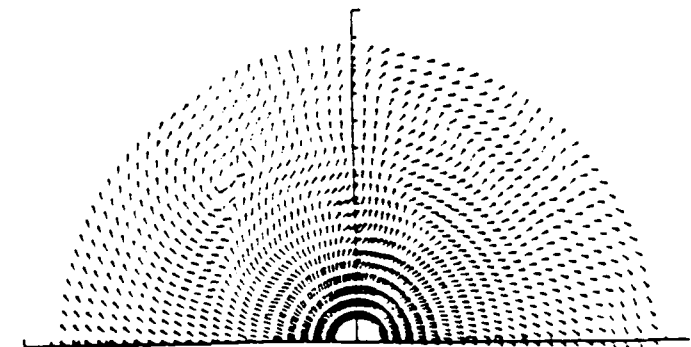
Proton Density



Temperature



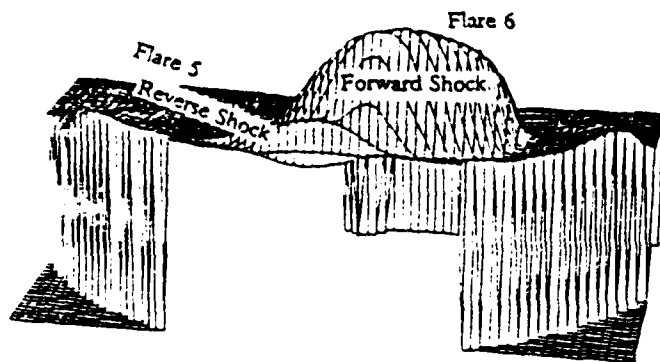
Total Pressure



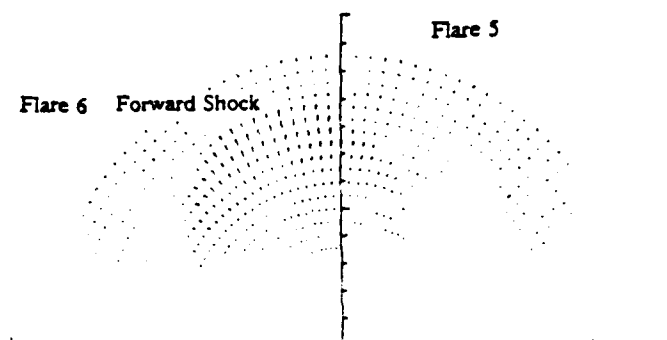
IMF Direction

26. Properties of simulated interplanetary medium at $t = 120.1$ hr (2306 UT, 7 February, 1986).

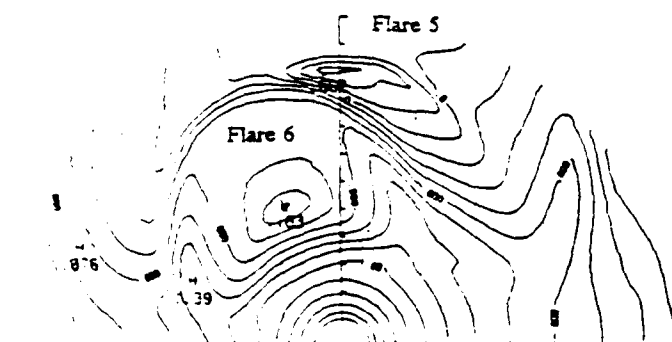
$t = 125.2 \text{ hr}$



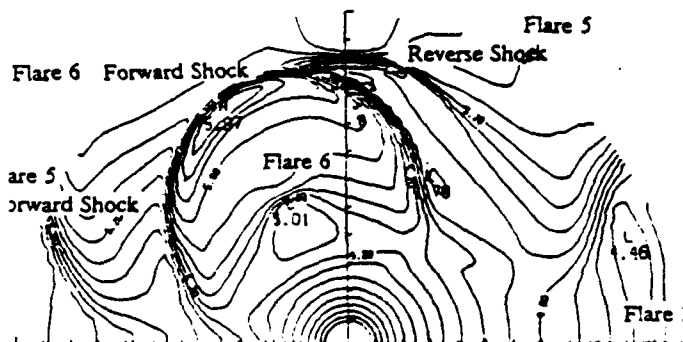
Solar Wind Speed



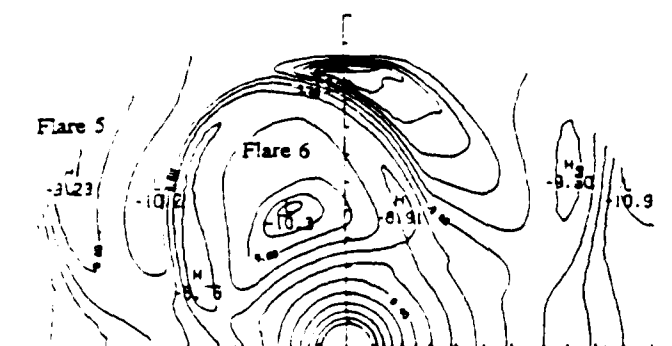
Velocity Increment
(maximum: 369 km/s)



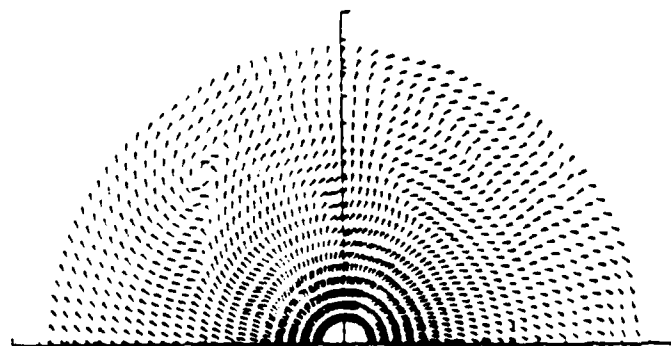
Proton Density



Temperature



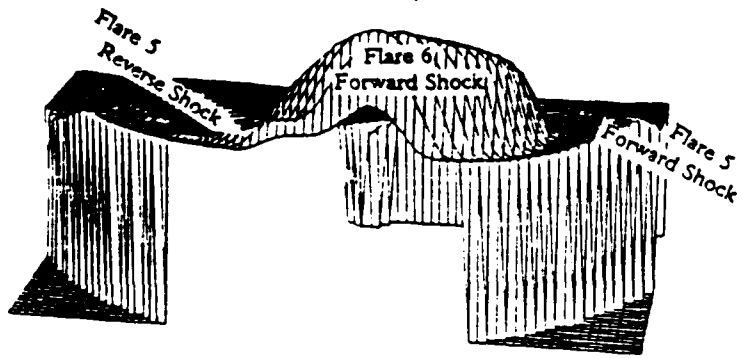
Total Pressure



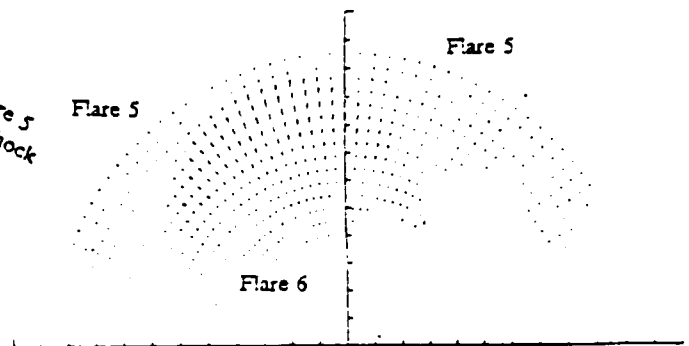
IMF Direction

27. Properties of simulated interplanetary medium at $t = 125.2 \text{ hr}$ (0412 UT, 8 February, 1986).

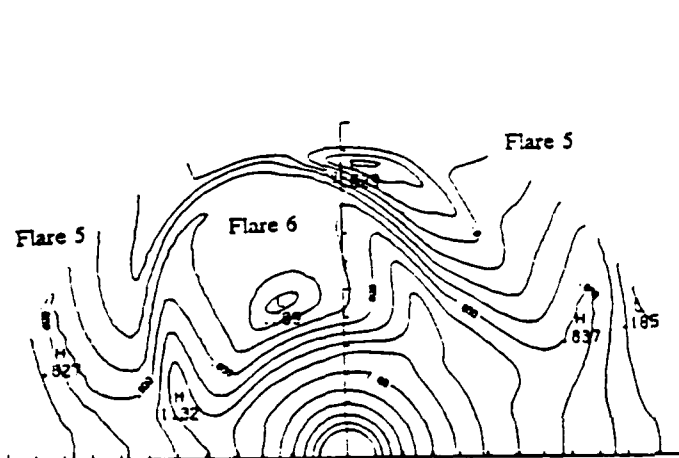
$t = 130.0 \text{ hr}$



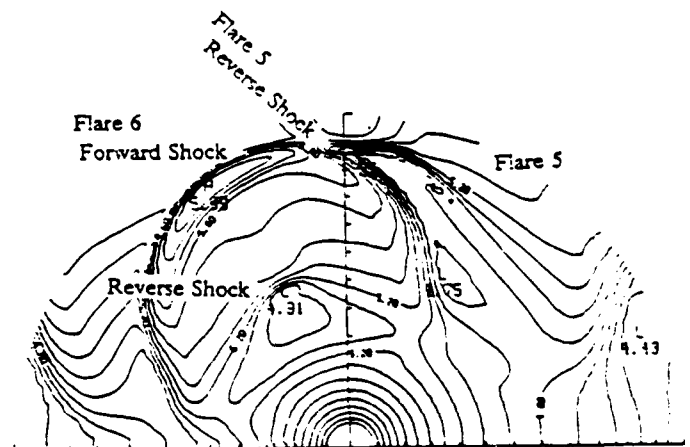
Solar Wind Speed



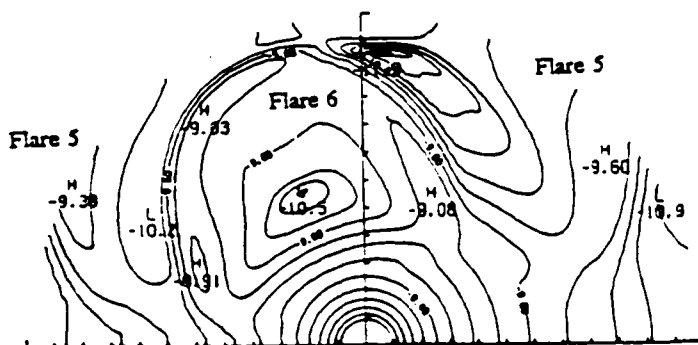
Velocity Increment
(maximum: 368 km/s)



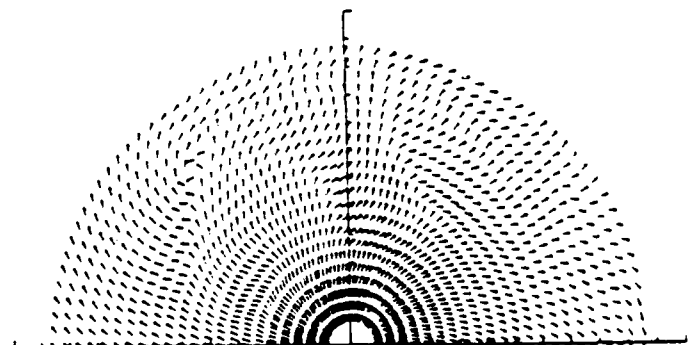
Proton Density



Temperature



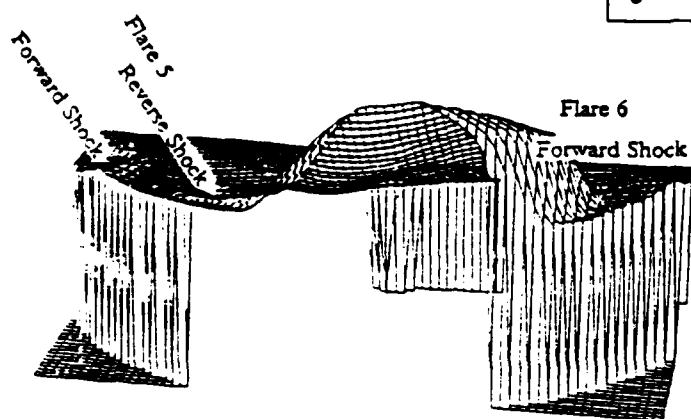
Total Pressure



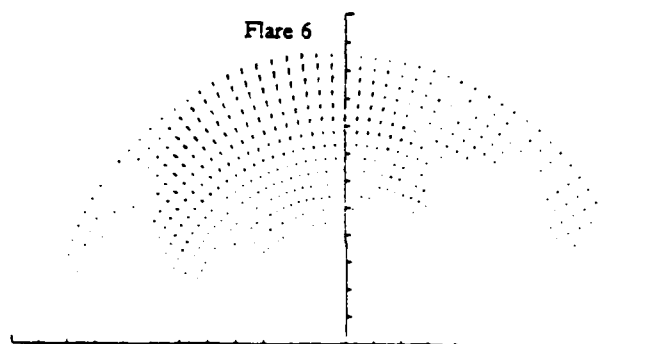
IMF Direction

28. Properties of simulated interplanetary medium at $t = 130.0 \text{ hr}$ (0900 UT, 8 February, 1986).

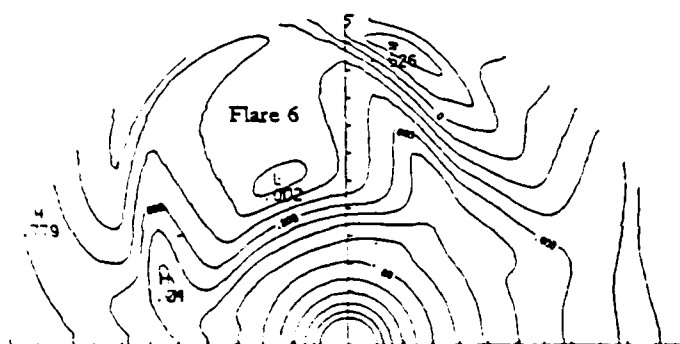
$t = 135.3 \text{ hr}$



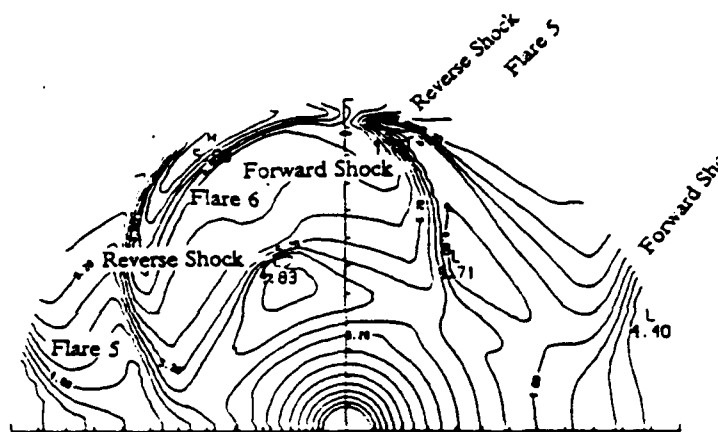
Solar Wind Speed



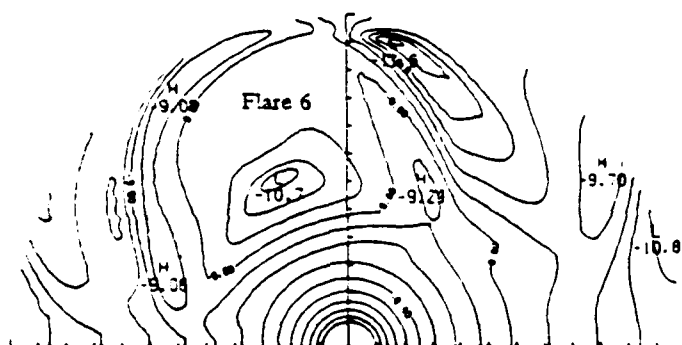
Velocity Increment
(maximum: 366 km/s)



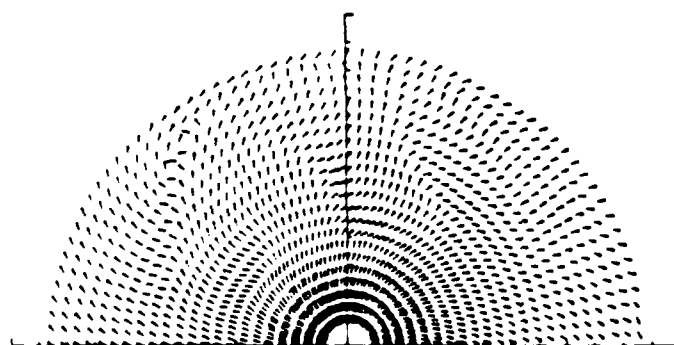
Proton Density



Temperature



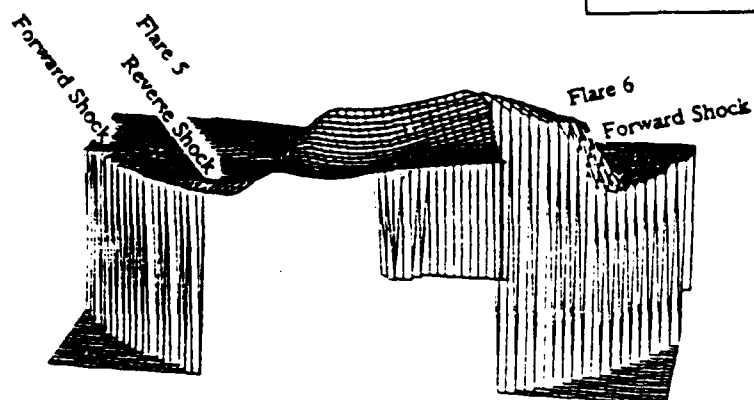
Total Pressure



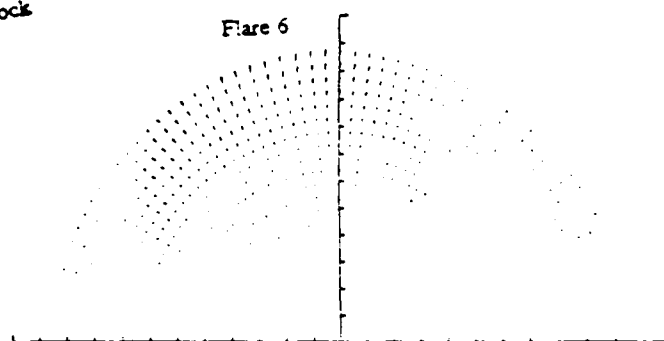
IMF Direction

29. Properties of simulated interplanetary medium at $t = 135.3 \text{ hr}$ (1418 UT, 8 February, 1986).

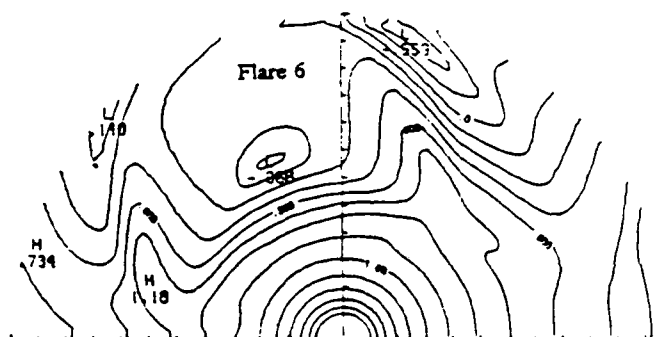
$t = 140.1$ hr



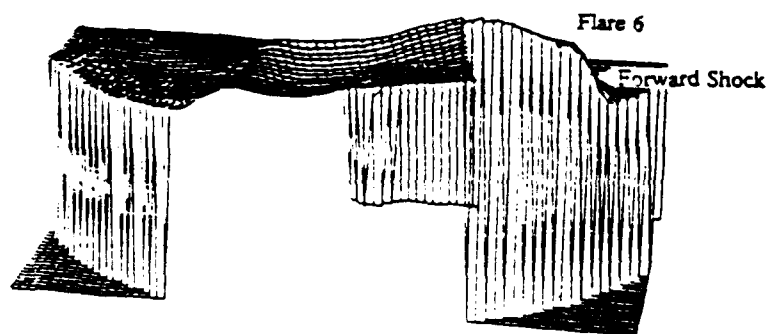
Solar Wind Speed



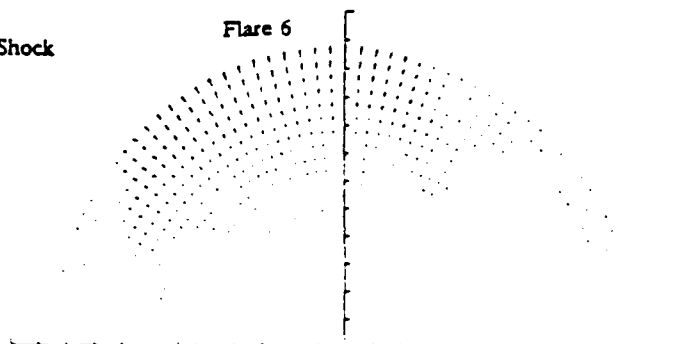
Velocity Increment
(maximum: 338 km/s)



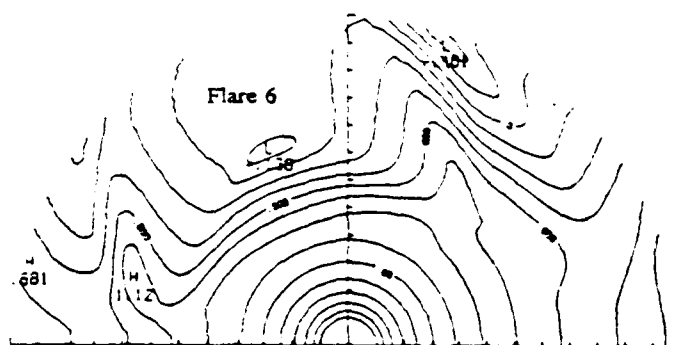
$t = 145.3 \text{ hr}$



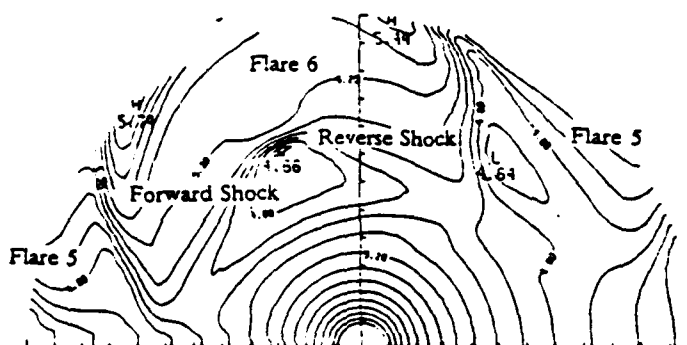
Solar Wind Speed



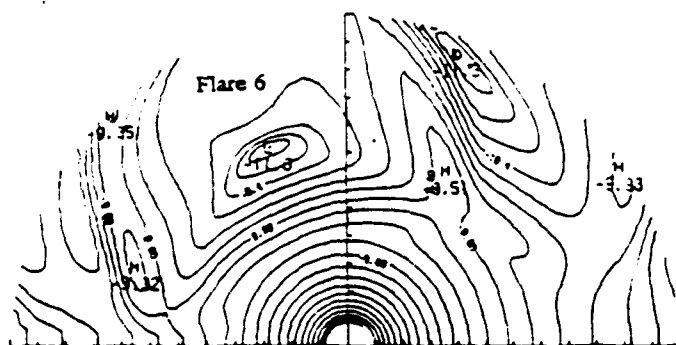
Velocity Increment
(maximum: 275 km/s)



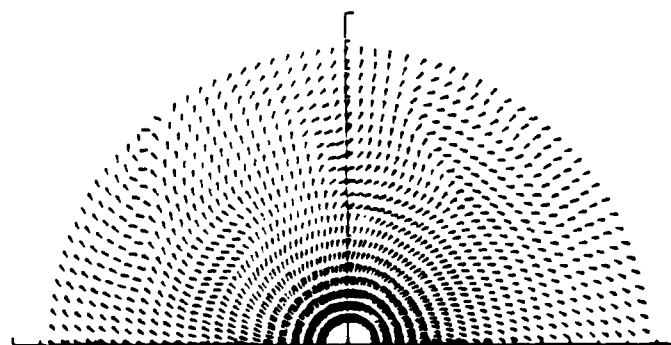
Proton Density



Temperature

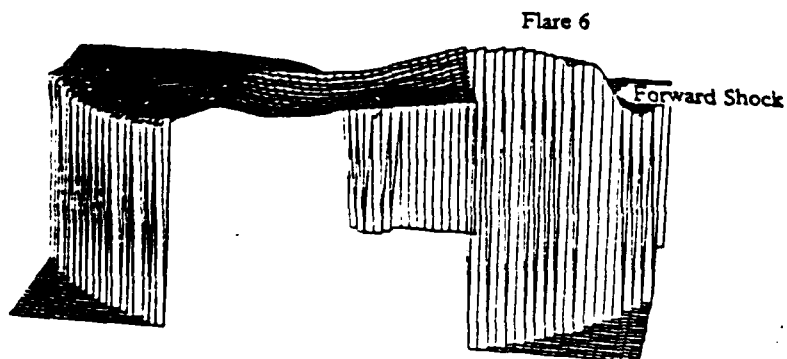


Total Pressure

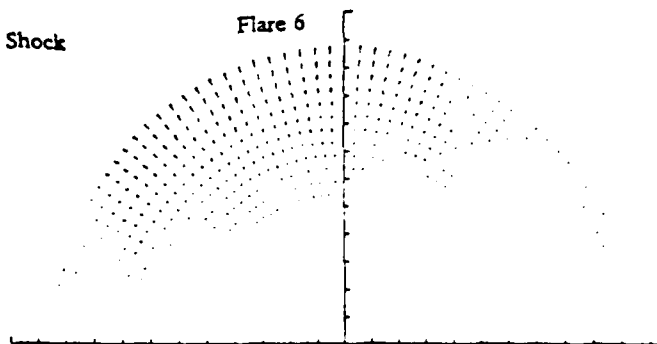


IMF Direction

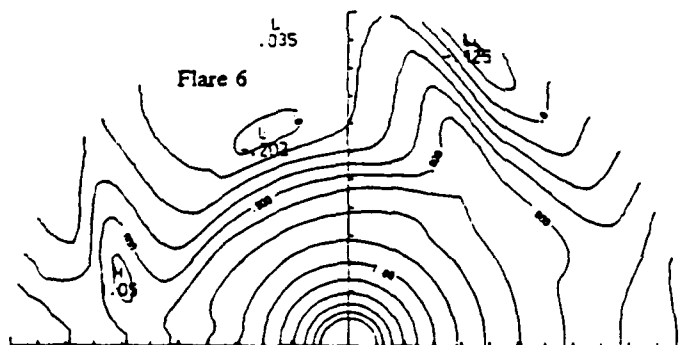
31. Properties of simulated interplanetary medium at $t = 145.3 \text{ hr}$ (0018 UT, 9 February, 1986).

$$t = 150.3 \text{ hr}$$


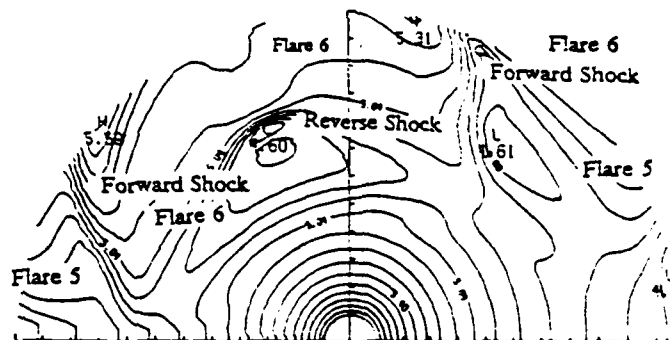
Solar Wind Speed



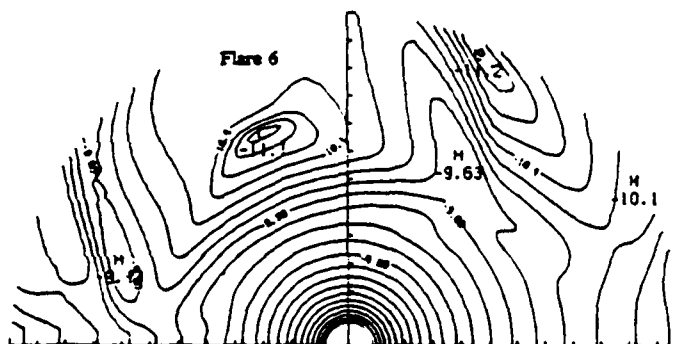
Velocity Increment
(maximum: 231 km/s)



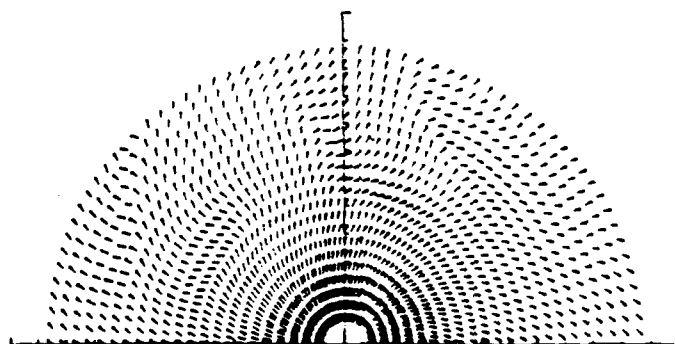
Proton Density



Temperature



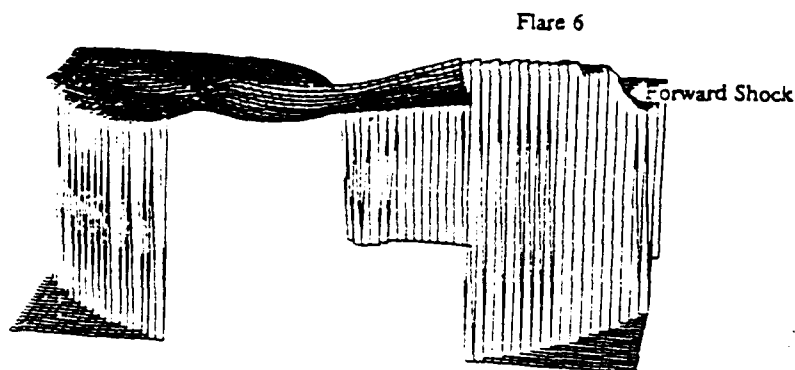
Total Pressure



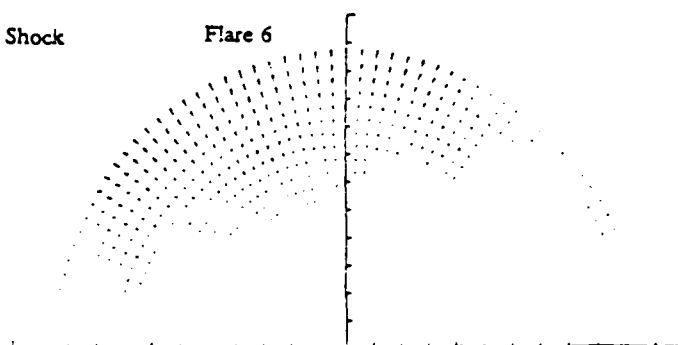
IMF Direction

32. Properties of simulated interplanetary medium at $t = 150.3$ hr (0518 UT, 9 February, 1986).

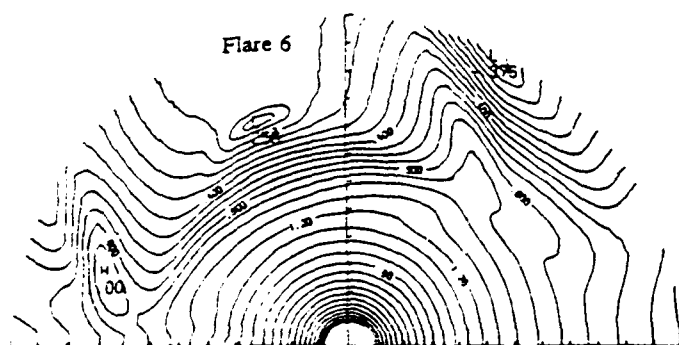
$t = 155.2 \text{ hr}$



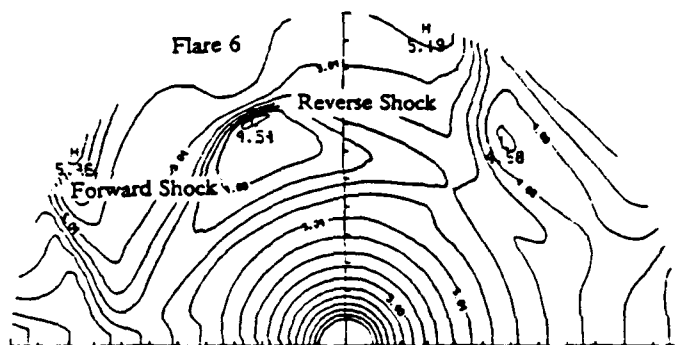
Solar Wind Speed



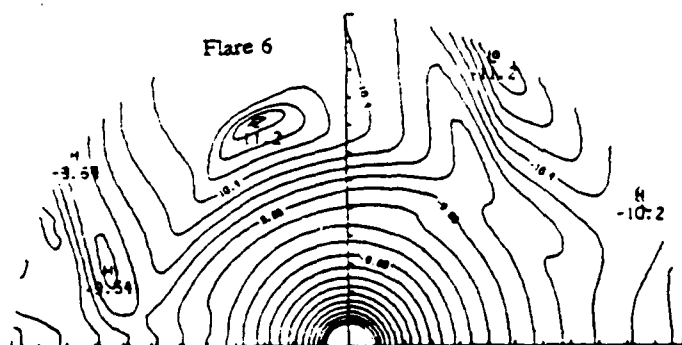
Velocity Increment
(maximum: 193 km/s)



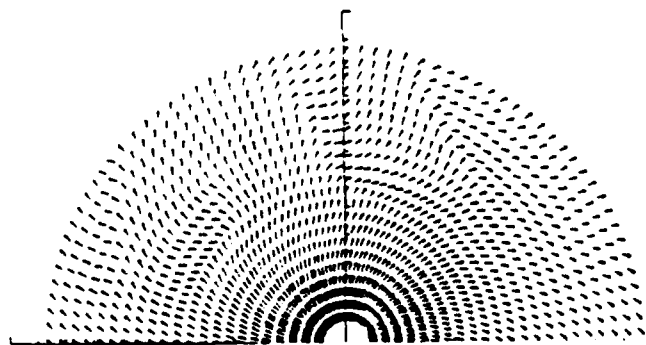
Proton Density



Temperature



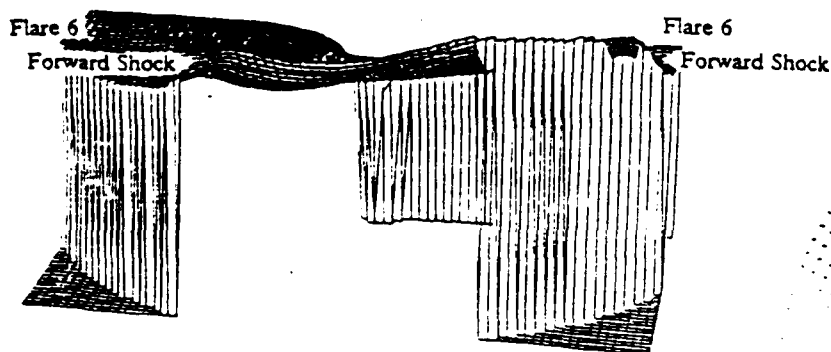
Total Pressure



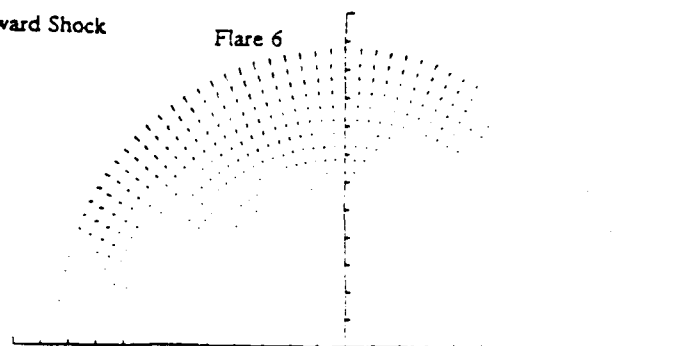
IMF Direction

33. Properties of simulated interplanetary medium at $t = 155.2 \text{ hr}$ (1012 UT, 9 February, 1986).

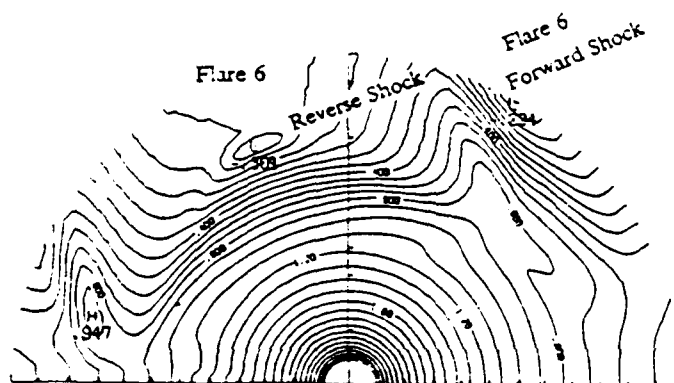
$t = 160.1$ hr



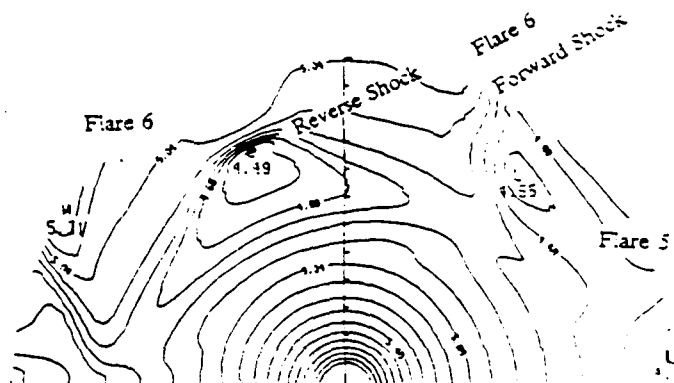
Solar Wind Speed



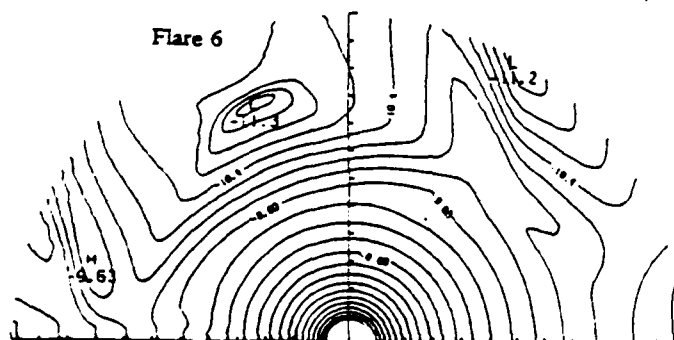
Velocity Increment
(maximum: 160 km/s)



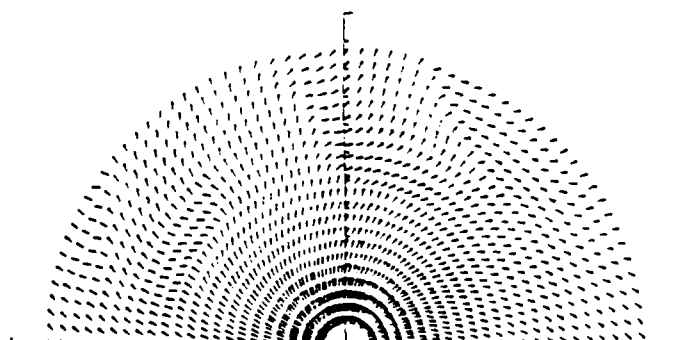
Proton Density



Temperature



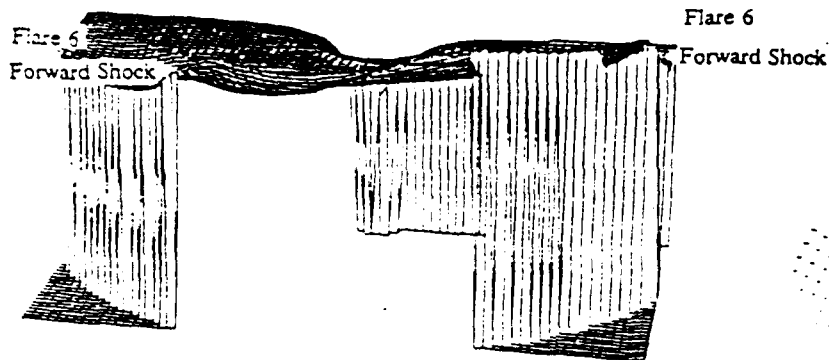
Total Pressure



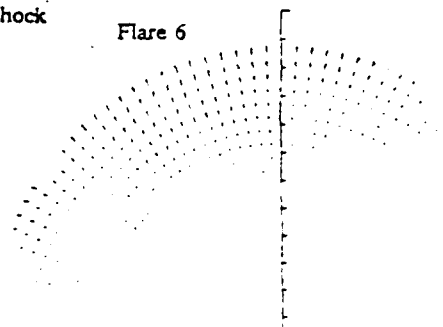
IMF Direction

34. Properties of simulated interplanetary medium at $t = 160.1$ hr (1506 UT, 9 February, 1986).

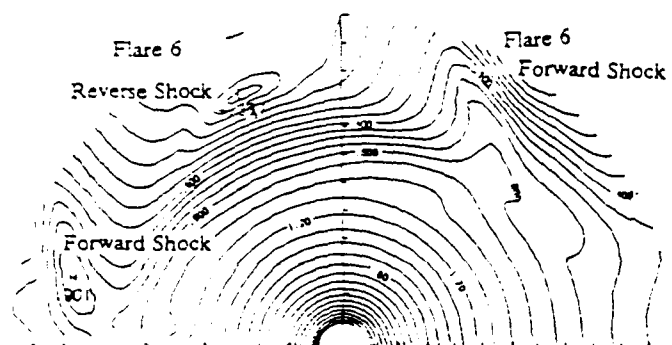
$t = 165.3 \text{ hr}$



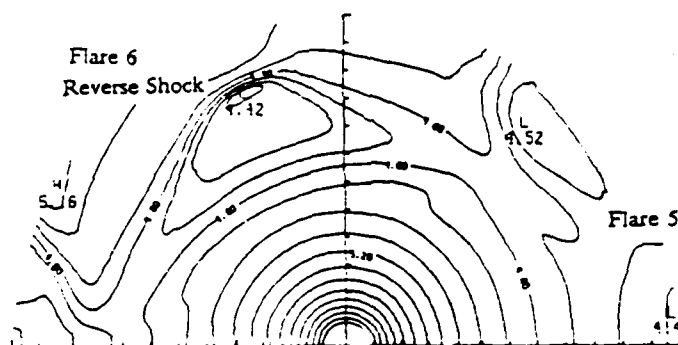
Solar Wind Speed



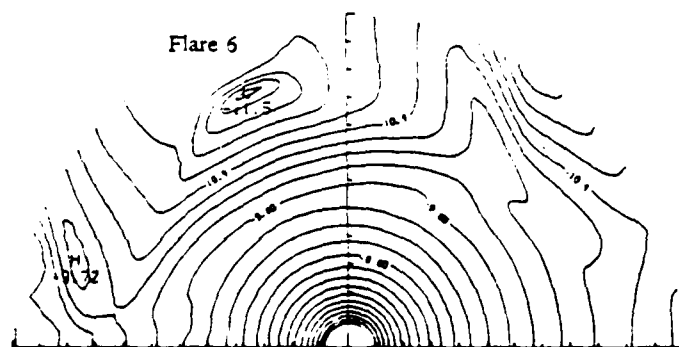
Velocity Increment
(maximum: 130 km/s)



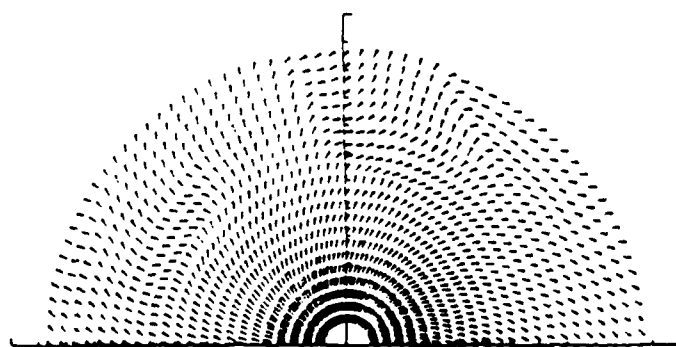
Proton Density



Temperature



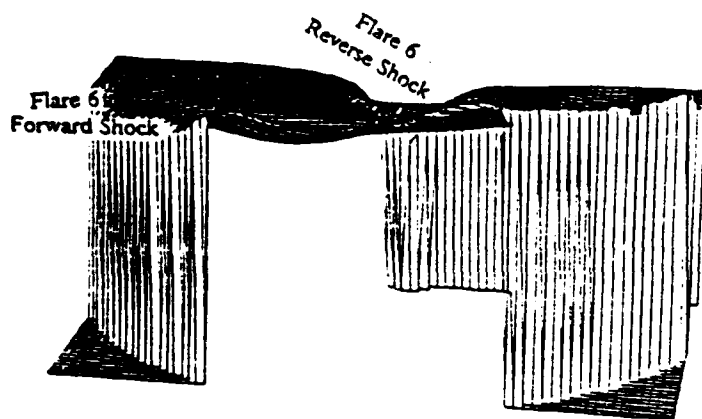
Total Pressure



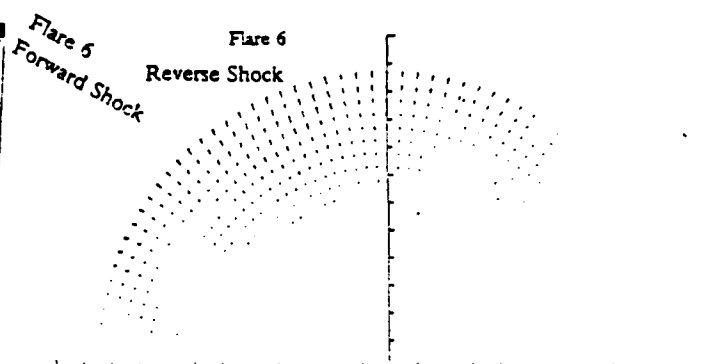
IMF Direction

35. Properties of simulated interplanetary medium at $t = 165.3 \text{ hr}$ (2018 UT, 9 February, 1986).

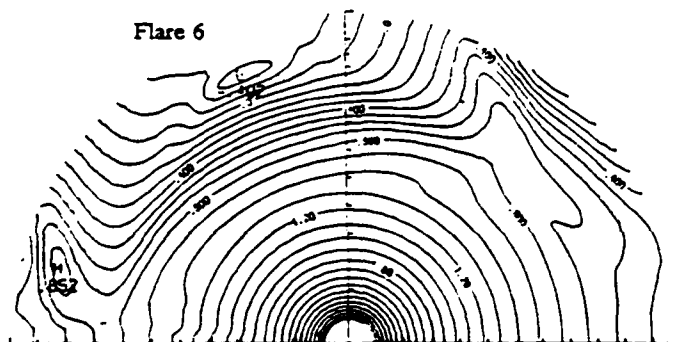
$t = 170.3 \text{ hr}$



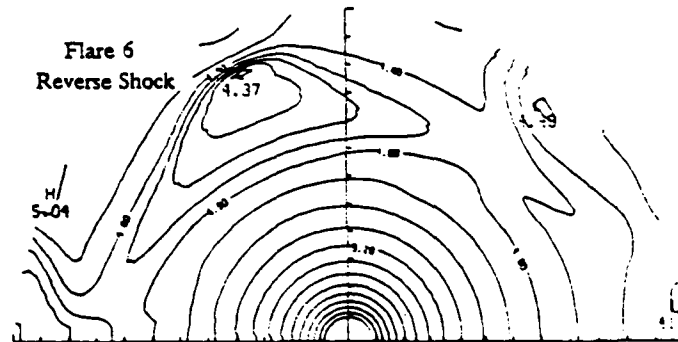
Solar Wind Speed



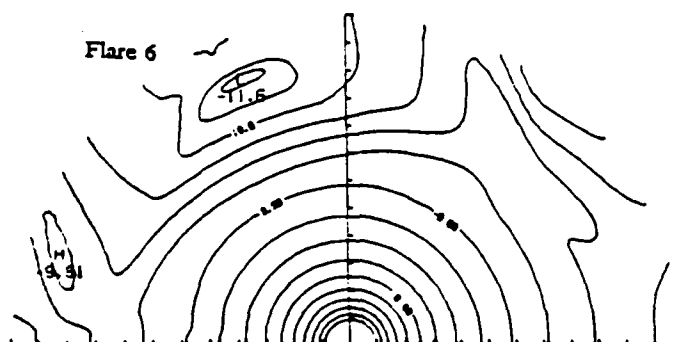
Velocity Increment
(maximum: 106 km/s)



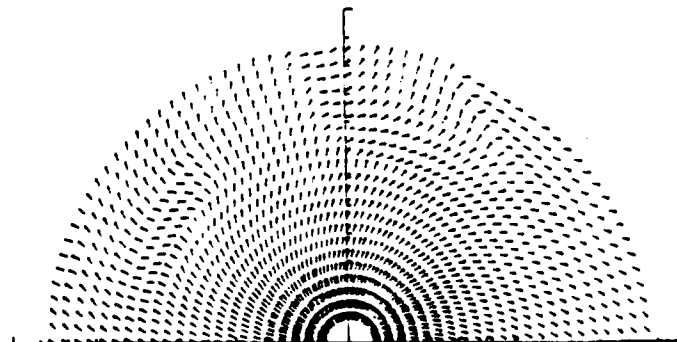
Proton Density



Temperature



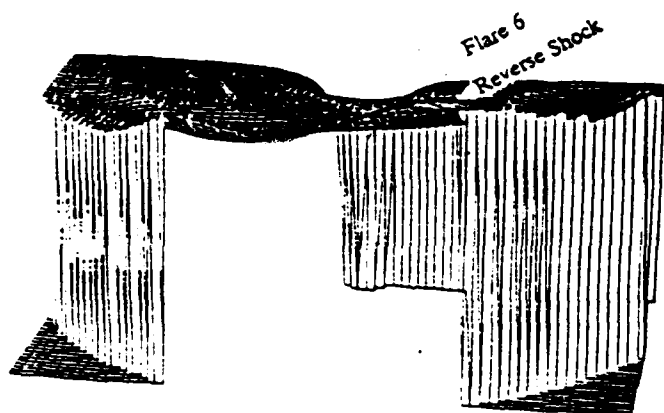
Total Pressure



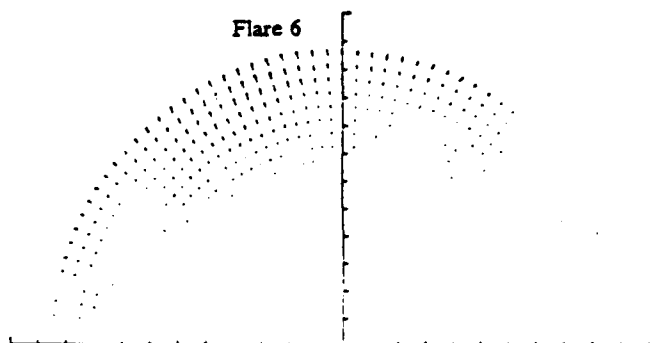
IMF Direction

36. Properties of simulated interplanetary medium at $t = 170.3 \text{ hr}$ (0118 UT, 10 February, 1986).

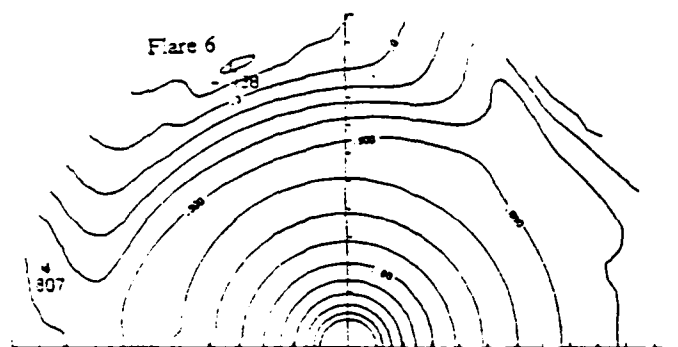
$t = 175.1 \text{ hr}$



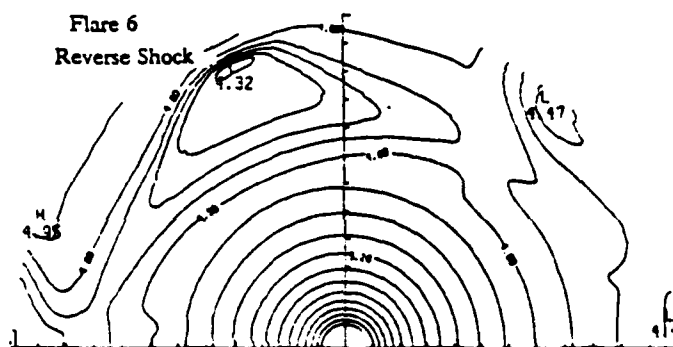
Solar Wind Speed



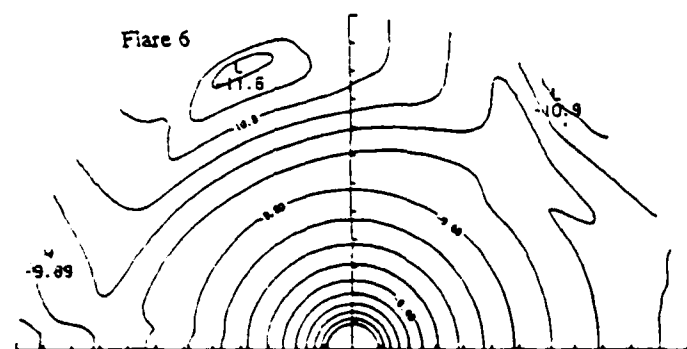
Velocity Increment
(maximum: 92.6 km/s)



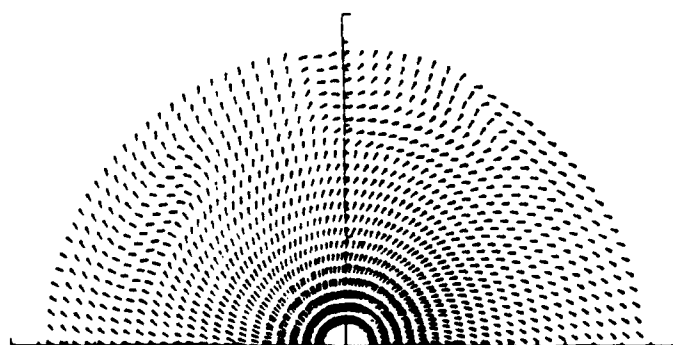
Proton Density



Temperature



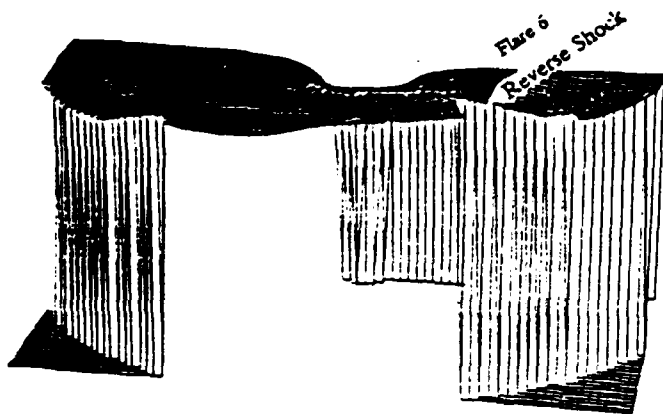
Total Pressure



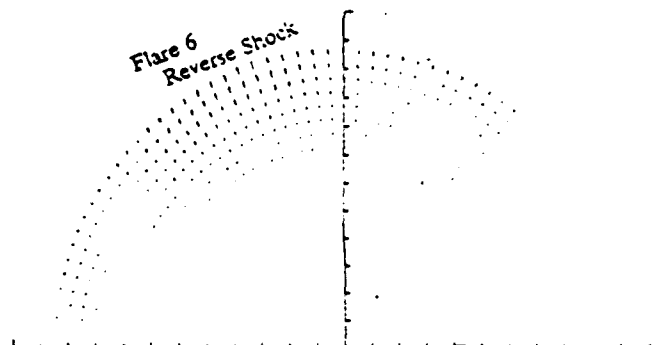
IMF Direction

37. Properties of simulated interplanetary medium at $t = 175.1 \text{ hr}$ (0606 UT, 10 February, 1986).

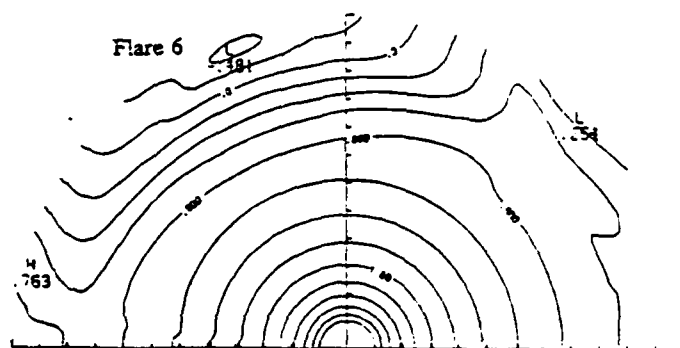
$t = 180.1 \text{ hr}$



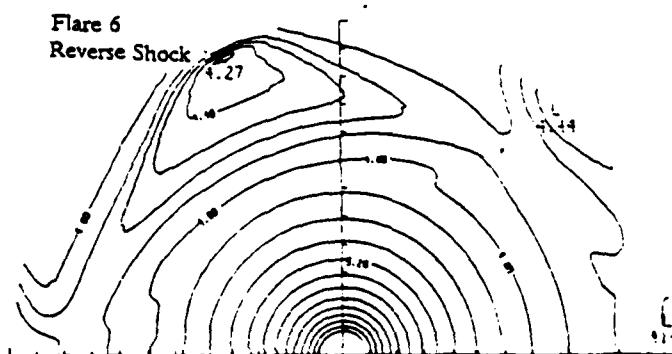
Solar Wind Speed



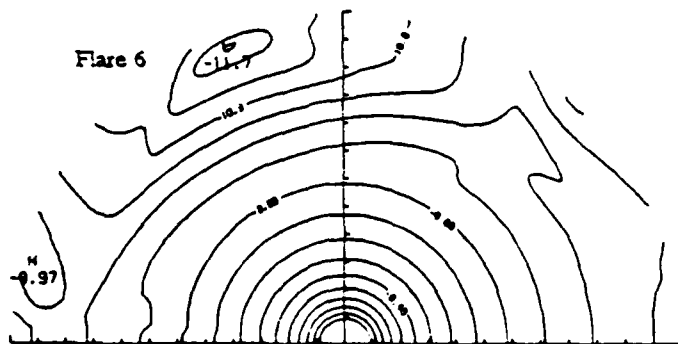
Velocity Increment
(maximum: 91.2 km/s)



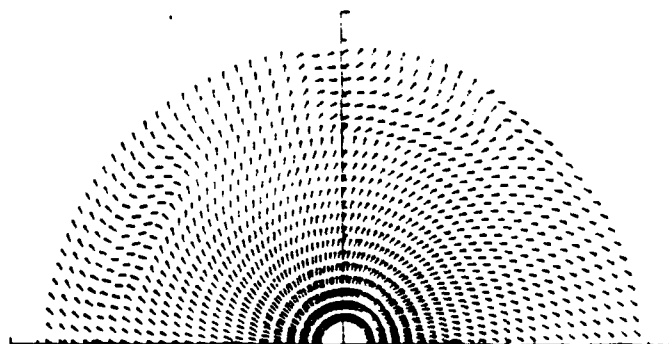
Proton Density



Temperature

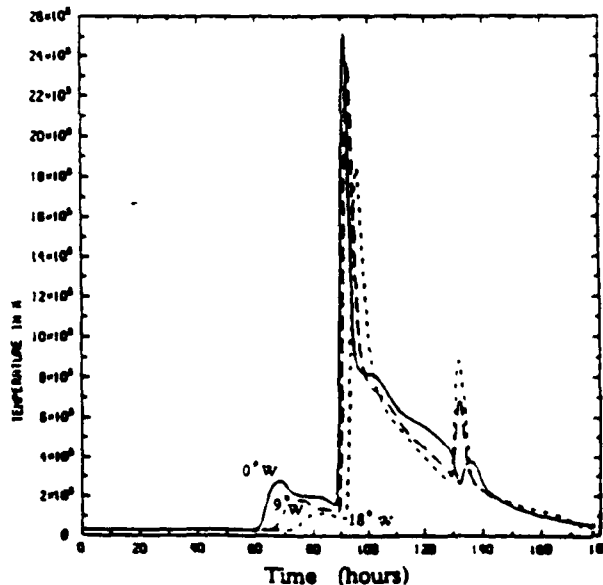
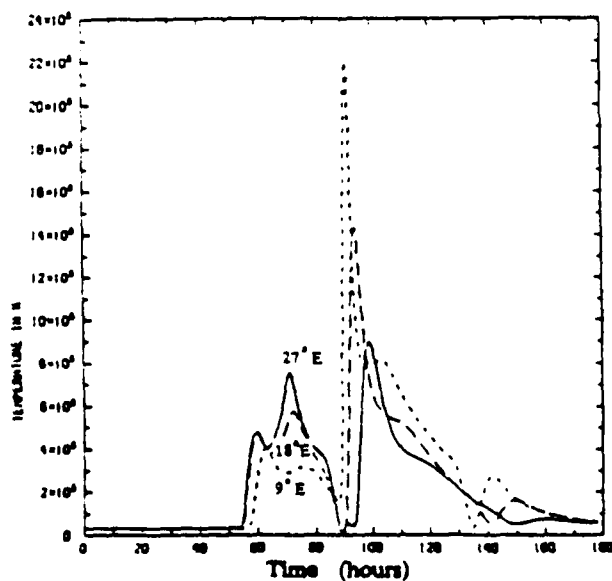
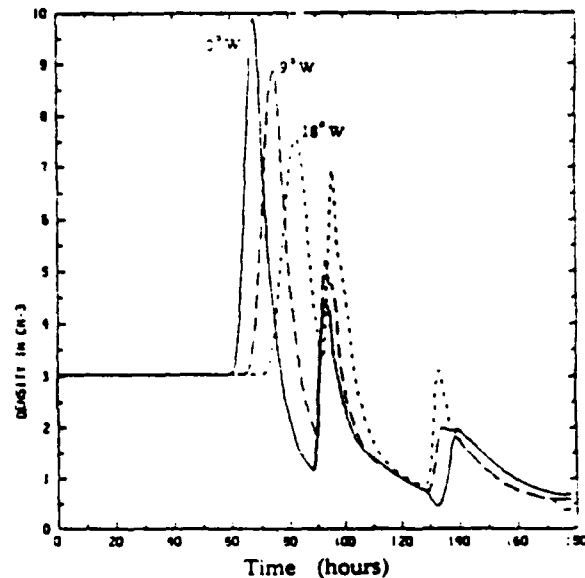
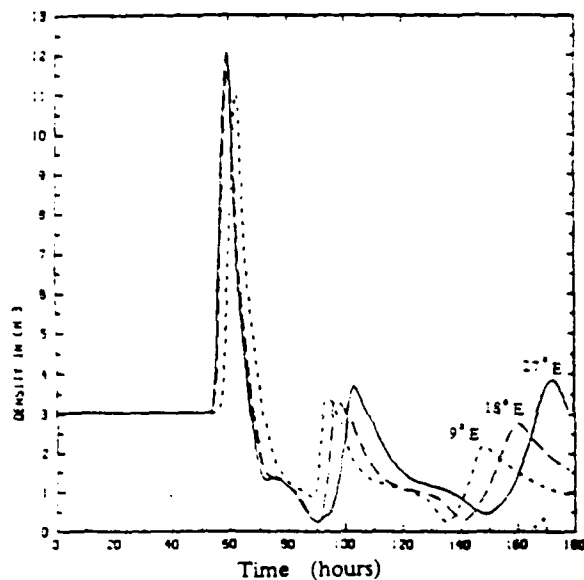
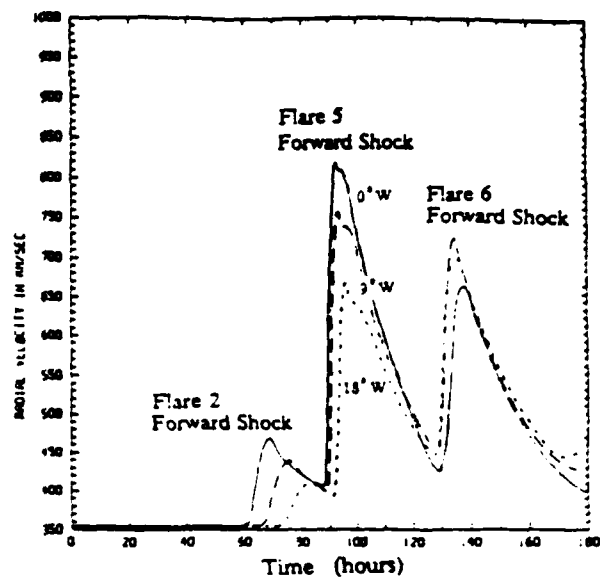
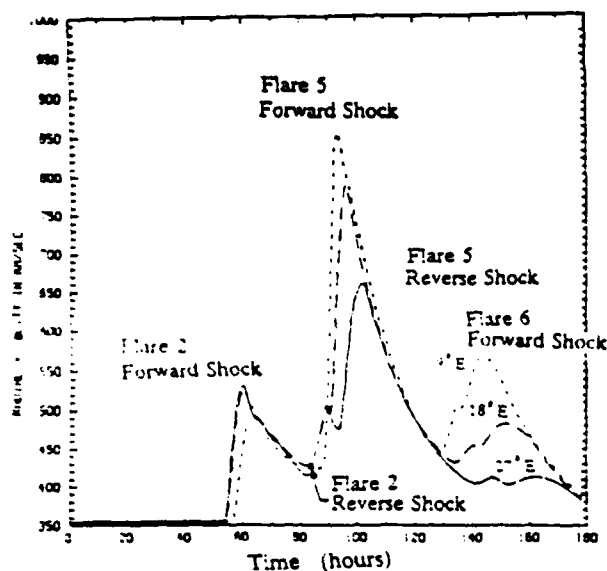


Total Pressure

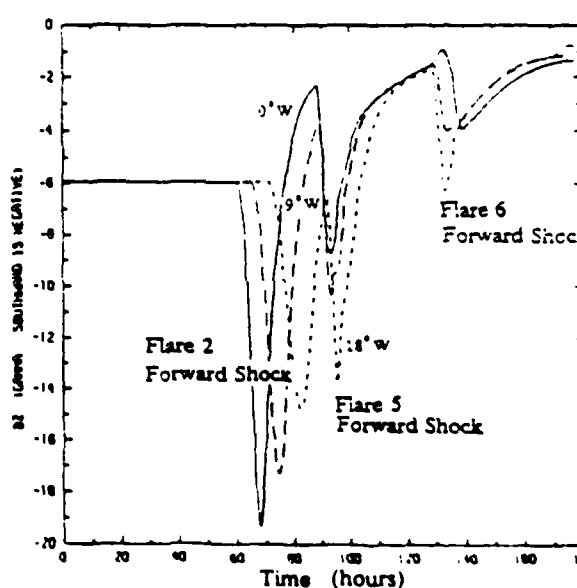
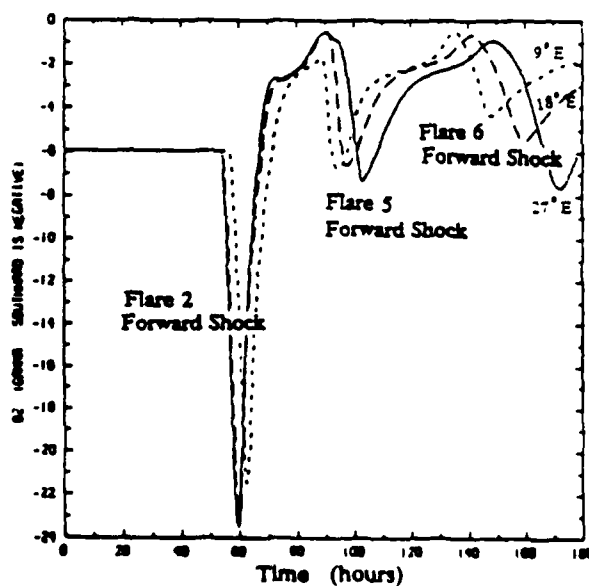
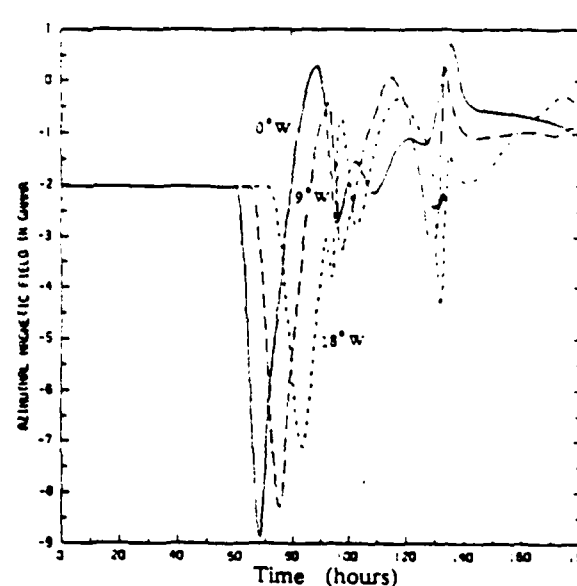
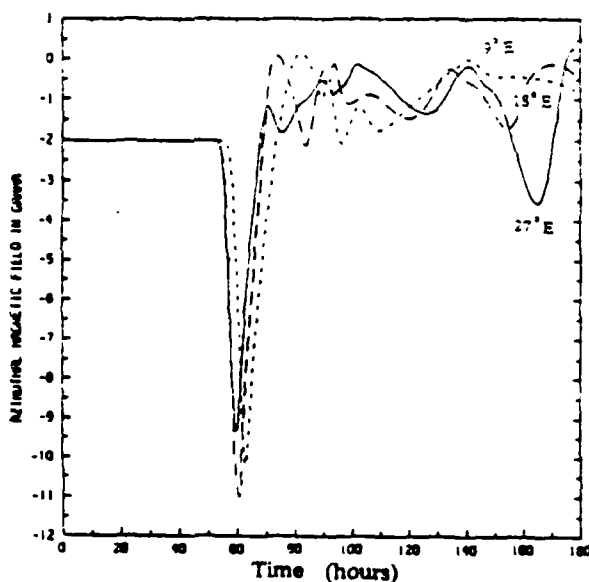
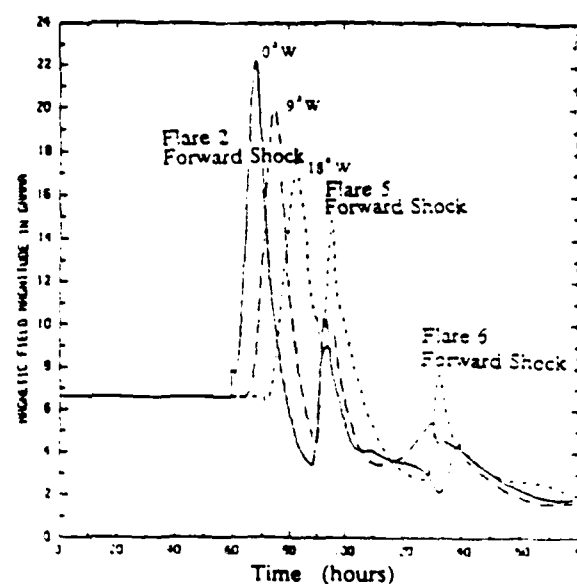
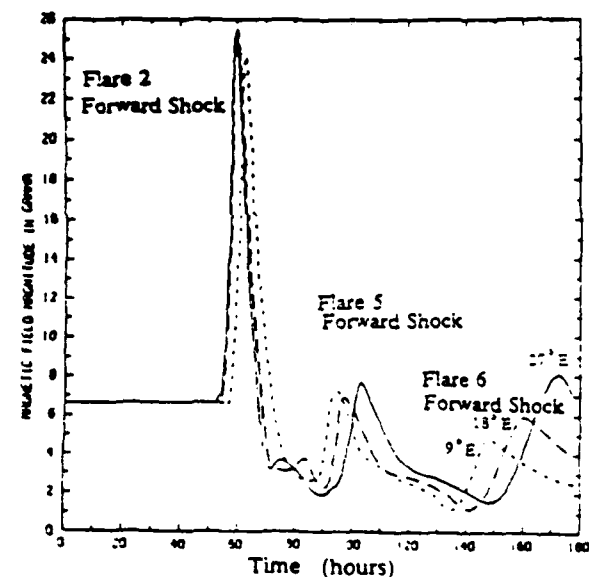


IMF Direction

38. Properties of simulated interplanetary medium at $t = 180.1 \text{ hr}$ (1106 UT, 10 February, 1986).

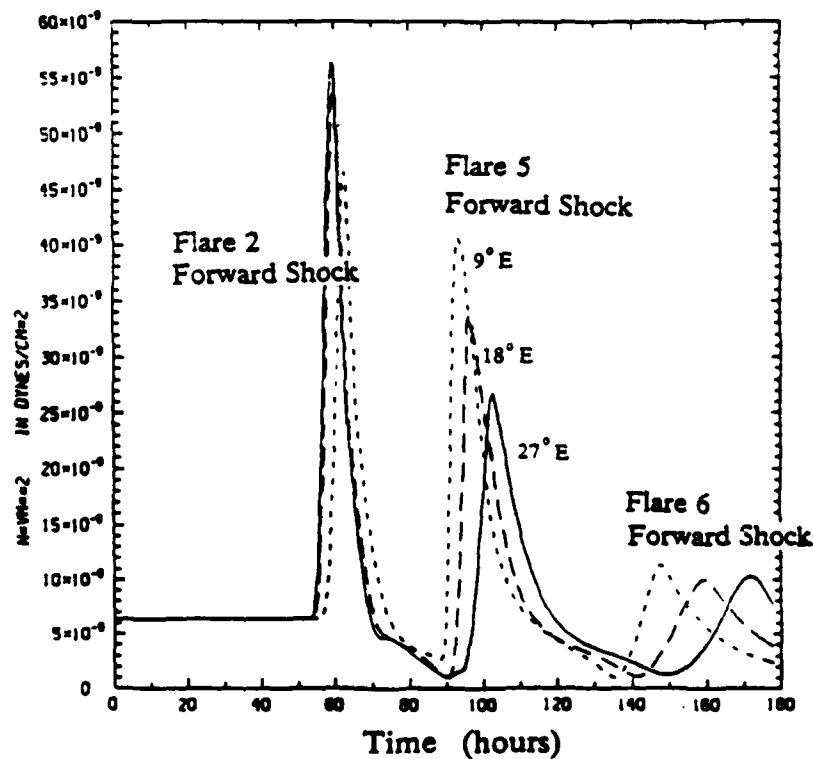
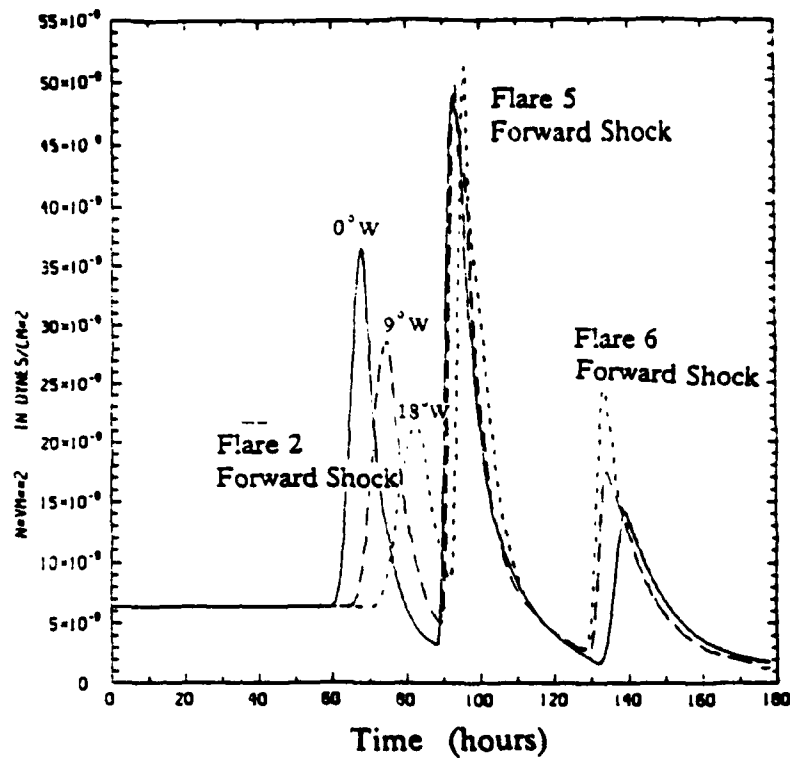


39. Time series of simulated radial velocity V_r , density, n , and temperature, T , at six sampling points at 1 AU. Left column presents the simulations at 27°E (solid curve), 18°E (dashed curve), and 9°E (dotted curve) of Earth's central meridian. Right column presents the simulations at 0°W (Earth's position, solid curve), 9°W (dashed curve), and 18°W (dotted curve) of Earth's meridian.



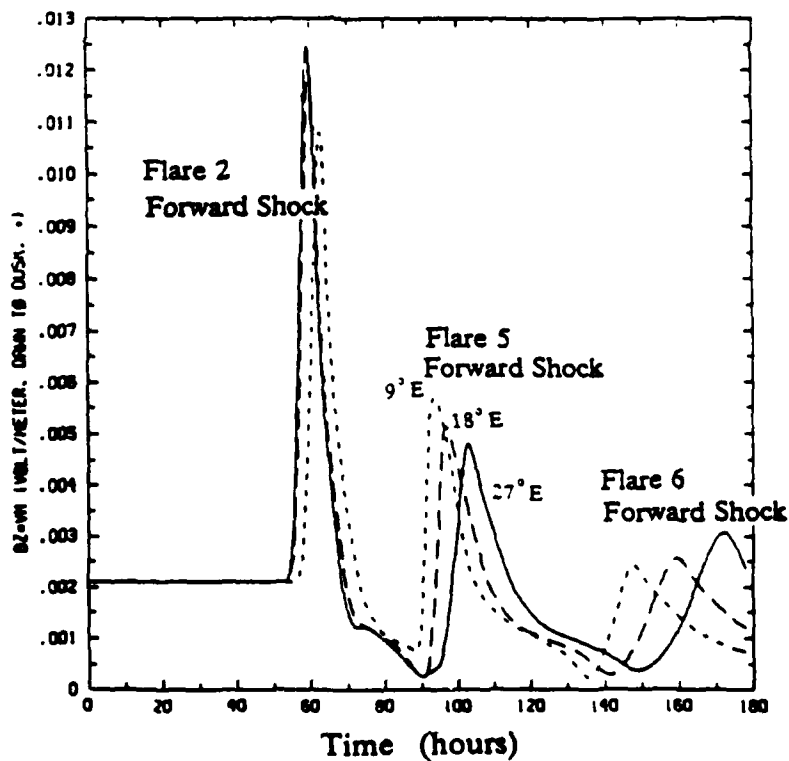
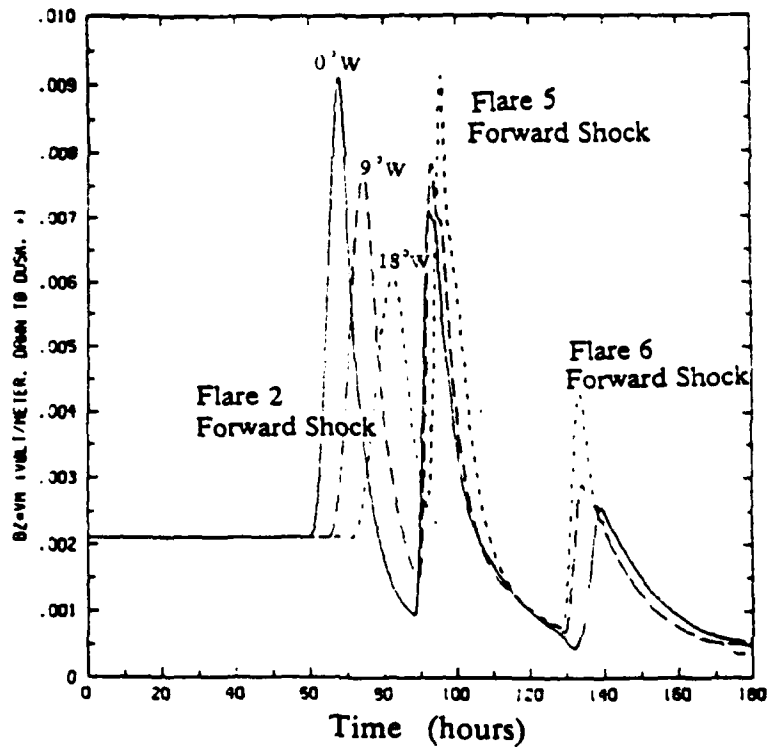
40. Time series of simulated interplanetary magnetic field magnitude $|B|$, azimuthal magnetic field component B_θ , and the negative value of the meridional magnetic field component B_ϕ plotted here as B_z , at six hypothetical sampling points at 1 AU. As in Figure 39, the panels on the left side refer to the three points east of Earth and, on the right side, to Earth's position and two additional points to the west of Earth.

at 1.0 AU



41. Time series of simulated momentum flux (nmV^2) at six hypothetical sampling points at 1 AU. Upper panel refers to Earth's position (0°W of central meridian, solid curve), 9°W (dashed curve), and 18°W (dotted curve) of central meridian. Lower panel refers to 27°E (solid curve), 18°E (dashed curve), and 9°E (dotted curve) of Earth's meridian.

at 1.0 AU



42. Time series of simulated cross-magnetospheric tail electric field (VB_z) variations at six hypothetical sampling points at 1 AU. Upper panel refers to Earth's position ($0^\circ W$ of central meridian, solid curve), $9^\circ W$ (dashed curve), and $18^\circ W$ (dotted curve) of Earth's meridian. Lower panel refers to $27^\circ E$ (solid curve), $18^\circ E$ (dashed curve), and $9^\circ E$ (dotted curve) of Earth's meridian.

END

12-86

DTIC